

ulm university universität ulm

Investigations of the kinetics and mechanism of the selective methanation of CO in CO_2 and H_2-rich reformates over Ru supported catalysts

Universität Ulm
Institut für Oberflächenchemie und Katalyse

Dissertation zur Erlangung des Doktorgrades
Dr. rer. nat. der Fakultät für Naturwissenschaften der Universität Ulm

Stephan Eckle
(München)
2012

Amtierender Dekan:	Prof. Axel Groß
1. Gutachter:	Prof. R.J. Behm
2. Gutachter:	Prof. N. Hüsing
3. Gutachter:	Prof. M. Muhler

Tag der Promotion: 07.02. 2012

Für Iris und Jonah

Preface

The Ru/zeolite catalysts investigated in this work were supplied by Sued Chemie AG. Due to a non disclosure agreement it is not possible to provide any details on the synthesis or type of the zeolite. General information such as metal loading, BET area, metal particle sizes, however, will be given in section 3.1.

Table of contents

1 Introduction 7
2 Experimental 15
2.1 Kinetic and conversion experiments 15
2.1.1 The ‚plug flow' model 16
2.1.2 Theory of the ‚plug-flow' reactor 17
2.1.3 Gas mixing unit 20
2.1.4 Gas Chromatograph (GC) 22
2.1.5 IMR / MS 22
2.2 Transmission Electron Micropsocope (TEM) 23
2.3 X-ray Photoelectron Spectroscopy (XPS) 24
2.4 X-ray Diffraction (XRD) 25
2.5 Hydrogen chemisorption 26
2.6 Dispersion and TOF calculation 27
2.7 Diffuse Reflectance Infrared Fourier Transform Spectroscopy (DRIFTS) 28
2.8 X-ray Absorption Spectroscopy (XAS) 31
2.8.1 Technical preconditions 31
2.8.2 Physical principles of the electron transition 33
2.8.3 XAS spectrum (XANES and EXAFS) 35
2.8.4 EXAFS: mathematical description 37
2.8.5 Sample preparation and experiment 39
2.8.6 EXAFS evaluation 42
3 Results and Discussion 49
3.1 Catalyst characterization 49
3.2 Activity, selectivity, and adsorbed reaction intermediates/reaction side products in the selective methanation of CO in reformate gases on supported Ru catalysts 57
3.2.1 Temperature screening experiments 58
3.2.2 Kinetic measurements 63
3.2.3 DRIFTS measurements 70
3.2.4 Transient experiments 79
3.2.5 Summary 83

3.3 Reaction intermediates and side products in the methanation of CO and CO_2 over supported Ru catalysts in H_2-rich reformate gases 87
3.3.1 CO methanation 87
3.3.2 Carbon dioxide methanation 94
3.3.3 Conclusion 98
3.4 What drives the selectivity for CO methanation in the methanation of CO_2-rich refomate gases on supported Ru catalysts. 100
3.4.1 *In situ* DRIFTS measurements 100
3.4.2 Kinetic measurements 109
3.4.3 Conclusions 114
3.5 Influence of the catalyst loading on the activity and the CO Selectivity of supported Ru catalysts in the selective methanation of CO in CO_2 containing feed gases 116
3.5.1 *In situ* DRIFTS measurements 117
3.5.2 SR-ref 6000 reformate 118
3.5.3 Reformate gases with low CO concentrations 120
3.5.4 Kinetic measurements 126
3.5.5 Conclusion 133
4 Summary 136
5 References 141
6 Appendix 150
6.1 German Summary 157
6.1.1 List of publications 163
6.1.2 Curriculum Vitae 165
7 Acknowledgement 166
8 Declaration 167

1 Introduction

Economically and ecologically efficient techniques for the production of sufficiently pure H_2 are a prerequisite for the introduction of H_2 based energy technologies [1]. Today, H_2 is mainly produced by partial oxidation (eq. 1.0) or catalytic steam reforming (eq. 1.1) of fossil fuels [2-8]. During partial oxidation (eq. 1.0) substoichiometric amounts of oxygen are added to the reformate, generating CO and hydrogen in an exothermic reaction. Steam reforming of fossil feed stocks necessitates the presence of water, a catalyst (usually Nickel based) [2] and high temperatures (~ 700°C) to produce H_2. Due to the reaction conditions in the reformer the latter reaction is usually accompanied by the water gas shift (eq. 1.2) and the methanation reaction (eq.1.3) both producing substantial amounts of CO_2 (up to 20%), CH_4 (5%) and CO (1-8%) in the resulting H_2-rich feed gas ('reformate') [5-8].

$C_nH_m + \frac{n}{2} O_2 \leftrightarrow n\,CO + \frac{m}{2} H_2 \quad \Delta H^0_R < 0$ [9] *eq. 1.0*

$C_nH_m + H_2O \leftrightarrow n\,CO + (n + \frac{m}{2})\,H_2 \quad \Delta H^0_R > 0$ [2] *eq. 1.1*

$CO + H_2O \leftrightarrow CO_2 + H_2 \quad \Delta H^0_R = -41{,}2\ kJ \cdot mol^{-1}$ [2] *eq. 1.2*

$CO + 3H_2 \rightarrow CH_4 + H_2O \quad \Delta H^0_R = -206{,}2\ kJ \cdot mol^{-1}$ [2] *eq. 1.3*

For the operation of low-temperature polymer electrolyte fuel cells (PEFCs), the resulting H_2-rich gas should be free of catalyst poisons, in particular the CO content has to be reduced to ≤10 ppm [10;11], which is most commonly achieved catalytically [2-4;7;12;13], besides other techniques such as pressure swing adsorption [14]. In a first step the combination of the high (HTS) and low (LTS) temperature water gas shift reaction (eq. 1.2 and 1.4) reduces the CO content of the feed gas. The high temperature water gas shift reaction (T= 310-450°C) features a large reaction rate for CO conversion, reducing the CO content to 3% over Fe_xO_y/Cr_2O_3 catalysts. Lower amounts are not possible due to the exothermic reaction. Therefore the subsequent low temperature water gas shift reaction (T= 200-260°C) lowers the remaining amount of CO to about 0.5-1%, employing Cu/ZnO catalysts. In a second step the remaining CO is usually lowered to below 10 ppm by the preferential oxidation of CO over Pt or Fe catalysts (PROX, eq. 1.4).

$CO + ½\ O_2 \rightarrow CO_2 \quad \Delta H^0_R = -283{,}2\ kJ \cdot mol^{-1}$ [15] *eq. 1.4*

$H_2 + ½\ O_2 \rightarrow H_2O \quad \Delta H^0_R = -241{,}8\ kJ \cdot mol^{-1}$ [15] *eq. 1.5*

However, the process management requires additional monitoring and units for O_2 dosing, as well as additional maintenance, which is only profitable for large scale applications. In addition the reaction of H_2 and excess oxygen to water (eq. 1.5) may lower the overall efficiency. Therefore, in cost sensitive, small scale applications (such as block heating stations), the methanation of the CO (eq. 1.3) may be a more attractive alternative for CO removal compared to the PROX reaction. The methanation reaction uses the H_2 present in the feed gas and avoids the need for an additional unit for O_2 dosing [5;16]. The loss of H_2 is tolerable, as long as the initial CO content, after the WGS reaction, is low (0.5 %). Precondition for this concept, however, is that the reaction is highly selective for the methanation of CO and that CO_2 methanation (eq. 1.7) is essentially inhibited, otherwise the losses of hydrogen would become intolerable [5;17].

$$CO_2 + 4H_2 \rightarrow CH_4 + 2H_2O \qquad \Delta H^0_R = -164{,}9\ kJ \cdot mol^{-1} \qquad [18] \quad \textit{eq.1.7}$$

The CO methanation reaction is closely related to the Fischer-Tropsch reaction, where higher hydrocarbons are generated by the reaction of CO and H_2. Depending on the desired product (long or short alkanes, olefins etc.), the reaction conditions vary over a wide range (T= 150-600°C, p= 1 bar to 100 bars, CO:H_2 ratio between 1.6-3) [19-21]. The most active catalysts in the Fischer-Tropsch reaction were oxide supported Fe, Co, Ni and Ru catalysts (see [19]) and references therein, [22]). Ru was identified as the most active and the most expensive catalyst, leading to a commercial use of the cheaper and less active iron, copper or nickel catalysts. Not surprisingly, the catalysts active for the Fischer-Tropsch Synthesis were identified also as the most active catalysts for the CO methanation reaction [20;22-34]. In the latter case the reaction conditions were usually altered to atmospheric pressure, moderate temperature (~200°C) and a CO:H_2 ratio of 3 in order to obtain mostly CH_4. Again, Ru was identified as the most active catalyst [23;24]. Even recent DFT studies showed, that the CO methanation reaction mechanism is faster over Ru than over Ni or Fe based catalysts [35-38]. However, due to the high costs of Ru metal the industrially used catalysts for this reaction are usually based on moderately priced Ni or Fe metal supported catalysts. Disadvantage of these catalysts is the fast deactivation with time due to a higher CO disproportionation probability (even in the absence of H_2) [29], as a result of strongly bound carbides and graphite. In contrast, Ru supported catalysts do not feature this problem to such an extent, resulting in

more stable catalysts. In addition, these catalysts showed a high selectivity / activity towards CO methanation in CO_2 containing gas mixtures [31;39-42]. For supported Ru catalysts, it was established in a number of studies that, in addition to the nature of the support material (see below), such as Al_2O_3, TiO_2 or zeolites, that the Ru particle size has a pronounced effect on their activity for CO methanation [26;43-45]. The Ru mass normalized reaction rate was found to increase with increasing Ru particle size. This was associated with the higher fraction of Ru terrace sites on larger Ru nanoparticles, which were considered to be more active for this reaction [25;26;43-45]. For very small Ru nanoparticles with diameter ~ 1 nm, the activity decreased steeply. In the latter publications the metal particle size was determined by TEM or H_2 chemisorption. While the above studies were conducted under Fischer-Tropsch reaction conditions in a typical syngas mixture (H_2:CO = 3), this trend was confirmed also in more recent studies performed under conditions more relevant for feed gas processing (H_2:CO = 14 or 100) [41;42;46-48].

Besides a high activity, the selectivity for CO methanation in the selective methanation in CO_2-rich gas atmospheres is an important property of methanation catalysts. In realistic reformates the CO selectivity is generally attributed to a surface blocking by adsorbed CO. This is driven by the higher adsorption energy of CO compared to CO_2. CO_{ad} blocks the surface for (dissociative) adsorption of CO_2 and subsequent methanation reaction [49;50]. In that case, CO_2 methanation will be inhibited, as long as the CO partial pressure and hence the CO_{ad} coverage on the catalyst is sufficiently high. Increasing the selectivity of Ru supported catalysts was already tried in many different ways, including the use of different support materials such as TiO_2, Al_2O_3, SiO_2 or CeO_2 [42;51-55] or of dopants [56;57], or varying the Ru particle size [40]. Also the use of zeolite supports was proposed as an alternative to standard supports such as TiO_2 or Al_2O_3. The zeolite supported Ru catalysts which did not affect the turn over frequency markedly for the methanation of CO compared to Ru/Al_2O_3 or Ru/SiO_2 catalysts, however enabled to maintain a high metal dispersion [58]. The CO_2 methanation under low CO partial pressures was not investigated by the various scientific groups. Despite of partially promising results of increasing the catalysts CO selectivity by doping [56;57] or the use of different supports [42;51-55], the physical origin of the increased selectivity remained unclear. This is partly due to the fact that in most cases the CO selectivity in the selective methanation reaction was evaluated only from “temperature screening”

measurements, which provide little mechanistic insight [17;47;48;53;54;56;57;59;60]. Furthermore, most of the previous studies on CO_x methanation over Ru catalysts dealt with the methanation of either CO or CO_2 rather than with the selective methanation of CO in CO_2-rich gas mixtures [26;30;32;41;42;51;61;62]. Finally, despite of a number of theoretical studies on CO methanation or on the Fischer-Tropsch reaction on Ru surfaces [37;38;63;64], the question of the selectivity has also not been investigated theoretically so far.

The mechanism of the reaction of CO or CO_2 to CH_4 as well as the active surface species of the selective methanation of CO are still under debate. The surface species formed during reaction were characterized mostly by *in situ* infrared spectroscopy studies on different Ru catalysts. Different types of CO_{ad} adsorbed on the Ru particles, e.g., CO_{ad} on oxidized Ru, linear and bridged CO_{ad} on Ru^0, surface formates and / or surface carbonates, as well as adsorbed $CH_{x,ad}$ species were observed during CO methanation on the catalyst [26-29;31;32;65]. From these studies it was not clear, however, whether there is a preference for a specific type of CO_{ad} as active species, and if so, for which of them. Surface formates and carbonates were commonly interpreted as side products [26;27]. In earlier studies, it was proposed that CO dissociates in the first step, leading to active and inactive carbon species, where the former are stepwise methanated to CH, CH_2, CH_3 and finally CH_4 [22;31;66-70]. Yamasaki et al. [28] showed in a very detailed *in situ* IR study that upon changing from a $^{12}CO/H_2$ reaction atmosphere to a $^{13}CO/H_2$ gas mixture the signals related to $^{12}CH_{x,ad}$ species disappeared, while signals related to the corresponding $^{13}CH_{x,ad}$ species were growing in [28]. They also estimated concentrations of CH_2 and CH_3 groups present on the surface under steady-state conditions. Assuming that these groups belonged to adsorbed C_xH_y hydrocarbon chains, they calculated the average length of the C_xH_y hydrocarbon chains. Based on these data they proposed a complex mechanism for the CO methanation reaction, where $CH_{x,ad}$ species act as reaction intermediates and CH_4 formation proceeds via formation and decomposition of adsorbed hydrocarbon chains [28]. However, since in the SSITKA-type (Steady State Isotope Transient Kinetic Analysis) experiments the $CH_{x,ad}$ removal rate in H_2 was not quantified and compared to the CH_4 formation rate, it is not clear, whether the reactive removal of the $CH_{x,ad}$ species observed in IR is really the rate-limiting step in the dominant reaction pathway, which would mean that these species represent reaction intermediates in that pathway, or whether they

should better be considered as spectator species or as reaction intermediates in a minority pathway (side reaction). Other studies, however, involving transient experiments, where H_2 was exchanged by D_2 after achieving steady-state conditions, provided convincing evidence that the adsorbed CH_x species, at least those detected by IR spectroscopy, represent side products rather than reaction intermediates [26;27]. In the latter studies it was observed that the CH_x species related IR signal did not decline even after 3 h. In a different concept, CO disproportionation was proposed as initial step, followed by carbon hydrogenation to CH_4 and CO_2 reduction to CO via the Reverse Water Gas Shift (RWGS) reaction [22;66]. More recent studies indicated that a formyl type (HCO) ad-species plays an important role in the CO methanation reaction, followed by C-O bond breaking and further hydrogenation [36;71]. This species was also identified as intermediate in the dominant reaction pathway during Fischer-Tropsch reactions in density functional theory (DFT) studies by Inderwildi et al. [37;64;72]. Still, the main question is whether the reaction starts with C-O bond breaking or with association of hydrogen and subsequent C-O band breaking.

The mechanism of the CO_2 methanation reaction is similarly controversial [22;73-78]. Following earlier proposals of direct CO_2 methanation [22], it is nowadays generally accepted that CO_{ad} is the main intermediate of the CO_2 methanation [71;73;74;76-79]. This CO_{ad} species is subsequently hydrogenated via the mechanism for CO methanation as discussed above. Several groups proposed for Ru supported catalysts that CO_2 first reacts to CO_{ad} via the Reverse Water Gas Shift (RWGS) reaction, which then continues to react to CH_4. It was suggested that the RWGS reaction proceeds via a formate intermediate [73;76-78]. However, the reaction mechanism of the RWGS may change for different catalytic systems, i.e. for CO_2 conversion on oxide supported Au catalysts a redox-type mechanism was proposed for the RWGS reaction [80]. Finally, dissociative CO_2 adsorption to CO_{ad} and O_{ad} and subsequent reaction of CO_{ad} to CH_4 was considered as a third alternative for the methanation of CO_2 [74].

It is important to realize also that almost all of the studies listed above focus on the hydrogenation of CO or CO_2 under conditions relevant for methane formation from synthesis gas, at nearly stoichiometric conditions ($CO:H_2$ = 1:3-1:4). Only few studies deal with reaction atmospheres with a high excess of hydrogen ($CO:H_2$ = 1:20-1:100), as it is typical for the selective methanation reaction

[17;27;36;40;42;47;48;51;53;54;56;57;60;68] with the above mentioned limitations. The different reactant ratios may have considerable effects on the reaction behavior and the dominance of a specific reaction pathway. In that sense, studies performed at close stoichiometric CO: H2 ratios may lead to mechanistic conclusions which are not necessarily relevant for the reaction under conditions typical for the selective methanation in H_2-rich reformate gases. In addition the few studies investigating the selective CO methanation deal mostly with integral reaction conditions or concentrate on either CO or CO_2 methanation. There are no publications investigating both reactions at the same time under differential reaction conditions, which are certainly needed to draw conclusions on the molecular based mechanism and the driving force behind the CO selectivity.

The motivation of this PhD thesis is to shine more light on the molecular mechanism of the CO and CO_2 methanation over supported Ru catalysts and to elucidate the physical origin of the driving force behind the selectivity for CO methanation specifically. This included two parts. First, the performance of commercial, supported Ru catalysts in the selective methanation of CO, various zeolite supported catalysts developed for these purposes and, for comparison, a standard Ru/Al_2O_3 catalyst was investigated. Second, the mechanistic details of the reaction were studied by various spectroscopic techniques, aiming at a physical understanding of the reaction mechanism and the resulting CO selectivities under conditions typical for selective methanation in H_2-rich reformate gases

The layout of the thesis is as follows:
First (section 3.1) the main techniques used for catalyst characterization will be described. Moreover *in situ* EXAFS results are described for all catalysts, which were finally used to determine the coordination number and thus the Ru particle size.
Second (section 3.2) the results of the CO methanation reaction in a number of different reaction atmospheres, going from pure H_2/CO and H_2/CO_2 mixtures to more realistic reaction mixtures, over a 2.2 wt.% Ru/zeolite and a 5 wt.% Ru/Al_2O_3 catalyst will be presented. The activity, selectivity and stability of the two catalysts were characterized in conversion experiments. Kinetic measurements, performed under differential reaction conditions, gave insight into reaction rates, activation energies and reaction orders. In the second part, the formation and their accumulation with time of different surface species under reaction conditions as well as their

decomposition in CO-free atmosphere (H_2/N_2 mixtures) was followed in transient *in situ* diffuse reflection IR Fourier transform spectroscopy (DRIFTS) measurements, performed under comparable reaction conditions (differential conversion, identical gas mixtures and reaction temperatures) as used in the kinetic measurements and compared to reaction and mass spectrometric transient data. The correlation between activity and build-up of surface species during the reaction under different reaction conditions and between the removal of adsorbates and CH_4 formation in transients in CO-free atmosphere on both Ru catalysts as well as consequences for the reaction pathway are discussed.

The next section (3.3) describes the identification and characterization of the active reaction intermediates of the CO and CO_2 methanation reaction on the standard Ru/Al_2O_3 catalyst and the Ru/zeolite catalyst under these reaction conditions. This was studied in transient SSITKA (Steady State Isotope Transient Kinetic Analysis) type IR experiments, where after 1000 min of reaction in idealized CO or CO_2 reformate one educt was replaced by its isotope labeled (^{13}CO, $^{13}CO_2$) isotopomer. Correlation of the build-up / decay of various surface species such as HCO_{ad}, $CH_{4,ad}$ and CO_{ad} upon the exchange step under otherwise constant reaction conditions with the steady-state activity of the catalysts allowed me to distinguish between reaction intermediates in the dominant reaction pathway and stable or less active reaction side products (‘spectator species’).

This is followed by an investigation of the reasons underlying the high CO selectivity of the Ru/zeolite catalyst in section 3.4, where results of a combined kinetic and *in situ* IR spectroscopic study on the effect of the CO content on the adsorption and reaction behavior on a Ru/zeolite and a Ru/Al_2O_3 catalyst are reported, focuses on correlations between CO_{ad} coverage and selectivity. The measurements were performed in a number of different idealized (H_2/CO) and semi-realistic ($H_2/CO/CO_2$) reaction atmospheres, decreasing the CO content to as low as 100 ppm. The temporal evolution of the adsorbed surface species during the methanation reaction in different reaction atmospheres, characterized by time-resolved *in situ* IR measurements is discussed in this section. In combination, these measurements allow me to not only to determine the steady-state CO_{ad} coverages in different reaction atmospheres, but also to quantitatively assess the contribution from CO_2 decomposition to the CO_{ad} signal in the experiments performed under semi-realistic conditions. The influence of the CO content on the CO methanation activity and on

the selectivity for CO methanation was also investigated. The resulting correlations between CO_{ad} coverage and the selectivity for CO methanation as well as consequences on the molecular scale mechanism responsible for the selectivity are discussed.

In the last section (3.5), the influence of the particle size of differently loaded Ru/zeolite catalysts on the CO selectivity is elucidated, where contributions of possibly different metal support interactions due to the different supports can be ruled out. Here results of a systematic, combined kinetic and *in situ* spectroscopy study on the effect of Ru metal loading and Ru particle size on the activity and in particular on the selectivity of Ru/zeolite catalysts in the selective methanation of CO are reported. The measurements were performed in a number of different idealized (H_2/CO, H_2/CO_2) and semi-realistic (H_2/CO/CO_2) reaction atmospheres, decreasing the CO content to as low as 100 ppm. *In situ* extended X ray absorption fine structure spectroscopy (EXAFS) and *in situ* diffuse reflectance IR spectroscopy (DRIFTS) measurements were employed, in addition to kinetic measurements, in order to gain information on the Ru particle sizes of the different catalysts during reaction under steady-state conditions (EXAFS) and on the temporal evolution of the adsorbate layer during the reaction (time-resolved DRIFTS). Finally, a brief comment on consequences of these findings for technical applications is provided.

2 Experimental

2.1 Kinetic and conversion experiments

The kinetic experiments performed in this work were carried out using a ‘plug flow’ reactor at atmospheric pressure. The first set up, employing ‘Gas Chromatography’ (GC) for the detection of the different feed gas and product components, was used for kinetic experiments under differential conditions (conversion of one educt < 15%), such as deactivation, activation energy, reaction orders. In order to achieve differential conditions, the catalyst was diluted with different amounts of SiO_2, which is inactive for the methanation reaction (refer to Table 8, appendix). In addition, conversion experiments under integral reaction conditions (conversion of one educt up to 100%) were performed, where pure undiluted catalysts were employed.

The second set-up, employing an ‘Ion Molecule Reaction Mass Spectrometer (IMR / MS) as detection unit, was used for instationary experiments, where one educt (CO) was shut off after reaching steady-state conditions. Details on the apparatus will be given in the following sections.

The compositions of the reformate gases applied during the experiments are given in Table 1.

Reaction gas	Reaction gas composition		
	not changing	CO	CO_2
ID-ref 100: Low-CO idealized reformate (100 ppm CO)	2.8 % N_2, balance H_2	100 ppm	0 %
ID-ref 1000 : Idealized reformate (1000 ppm CO):	2.8 % N_2, balance H_2	1000 ppm	0 %
ID-ref 6000 : Idealized reformate (6000 ppm CO)	2.8 % N_2, balance H_2	6000 ppm	0 %
CH_4 rich ID-ref 6000 : Idealized reformate (6000 ppm CO)	2.8 % N_2, balance H_2, 4.5% CH_4	6000 ppm	0 %
CO_2 rich ID-ref 6000 : Idealized reformate (6000 ppm)	2.8 % N_2, balance H_2	6000 ppm	1.2 %
SR-ref 100: Low-CO semi-realistic reformate (100 ppm CO):	2.8 % N_2, balance H_2	100 ppm	15.5 %
SR-ref 1000: Semi-realistic reformate (1000 ppm CO):	2.8 % N_2, balance H_2	1000 ppm	15.5 %
SR-ref 3000: Semi-realistic reformate (3000 ppm CO)	2.8 % N_2, balance H_2	3000 ppm	15.5 %
SR-ref 6000: Semi-realistic reformate (6000 ppm CO):	2.8 % N_2, balance H_2	6000 ppm	15.5 %
H_2O rich SR-ref 6000: Semi-realistic reformate (6000 ppm CO):	2.8 % N_2, 5 % H_2O balance H_2	6000 ppm	15.5 %
CO_2-ref: CO_2 reformate (CO-free)	2.8 % N_2, balance H_2	0 ppm	15.5 %
Low CO_2-ref: CO_2 reformate (CO-free)	2.8 % N_2, balance H_2	0 ppm	1.2 %

Table 1: Composition of the different reaction gases

2.1.1 The ‚plug flow' model

The model of the plug flow reactor is described as a volume dV (here: reaction gas mixture), which passes homogeneously through the catalyst bed [81]. It is assumed that the gas molecules only move along the flow direction, describing a 'plugged gas flow'. Furthermore, a homogeneous gas composition is required for the reaction to take place evenly.

A typical reactor consists of a quartz tube, 23.5 cm long, with a 6 and 4 mm outer and inner diameter and a wall thickness of 1 mm. The powder catalyst is placed in the middle of the reactor and fixed by glass wool at both ends. A Ni/CrNi thermocouple, which is placed in a small cavity in the middle of the reactor and attached by a ceramic glue on the basis of SiO_2 (Plytec, Type 905), measures the temperature. Normally, about 200 mg of diluted catalyst powder was used, which results in a catalyst bed of ca. 1 cm. The reactor is embedded into an oven, which is heated up to 600°C by a heating wire (Horst company). The heating power is adjusted by a control unit (Watlow, Model 982). Quartz wool serves as insulation of the oven and provides a basis for a constant temperature.

2.1.2 Theory of the ‚plug-flow' reactor

A detailed description of the plug flow model is given elsewhere [82;83]. This section provides only the basic theory of the ‚plug-flow' reactor and shortly explains the mathematic equations.

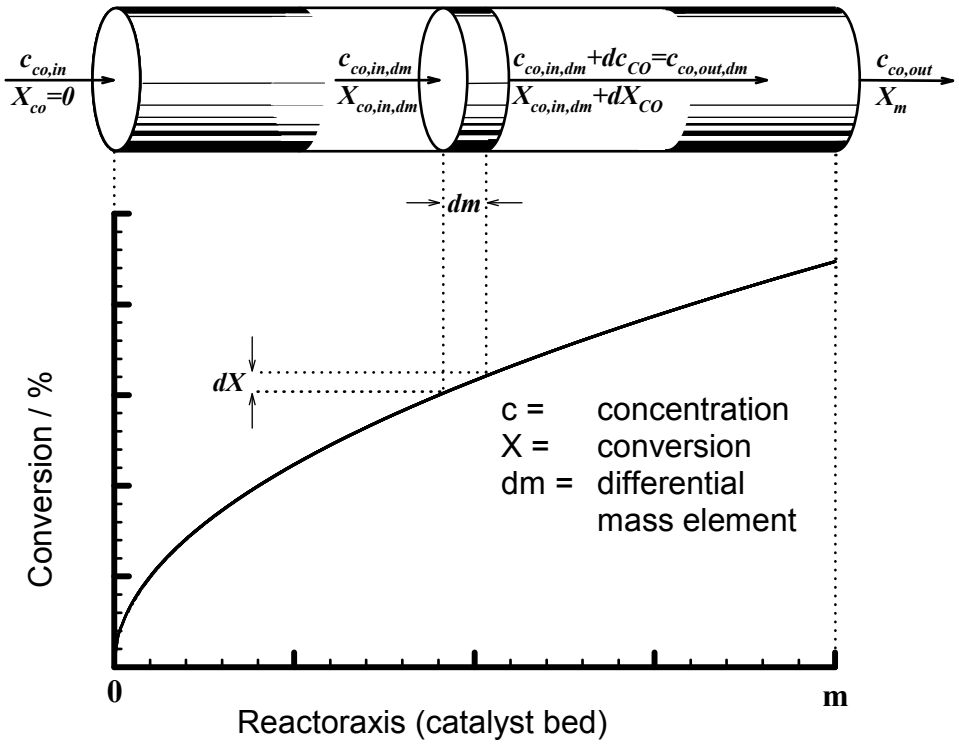

Figure 1: Schematic presentation of a plug flow reactor [82]

In order to compare experimental results of different measurements, a conversion independent parameter is needed, which is defined by the reaction rate. Determining the reaction rate requires the mass balance of the educts and products:

$$\text{substance}_{in} = \text{substance}_{out} + \text{substance}_{reaction} \qquad \textit{eq. 2.1}$$

The introduction of the volumetric flows ($\dot{V}_i = \dot{V}_{tot} \cdot c_i$) yields:

$$\dot{V}_{tot} \cdot c_i = \dot{V}_{tot} \cdot (c_i + dc_i) + (-r_i) \cdot dm \qquad \textit{eq. 2.2}$$

where

r_i: reaction rate of the component i for differential mass element dm $\left[\frac{mol \cdot i}{s \cdot g_{Kat}}\right]$

$\dot{V}_i$: volumetric flows of component i

c_i: concentration of component i

Rearrangement of eq. 2.2 yields:

$$\dot{V}_{tot} \cdot dc_i = r_i \cdot dm \qquad \textit{eq. 2.3}$$

The conversion of the component i can be described by the differential change in the concentration of the component:

$$X_i = \frac{c_i - c_{i_{out}}}{c_{i_{in}}} = 1 - \frac{c_{i_{out}}}{c_{i_{in}}} \qquad \textit{eq. 2.4}$$

where

X_i: conversion of component i for the differential mass element dm

For differential conversions the following simplification applies:

$$\frac{dX_i}{dc_i} = -\frac{1}{c_{i_{in}}} \text{ or: } dc_i = -dX_i \cdot c_{i_{in}} \qquad \textit{eq. 2.4}$$

with eq. 2.3 this results in:

$$\dot{V}_{tot} \cdot dX_i \cdot c_{i_{in}} = r_i \cdot dm \qquad \textit{eq. 2.5}$$

Applying $\dot{V}_i = \dot{V}_{tot} \cdot c_i$ on eq. 2.5 yields:

$$\dot{V}_{i_{in}} \cdot dX_i = -r_i \cdot dm \text{ or } dX_i = -r_i \cdot \frac{dm}{\dot{V}_{i_{in}}} \qquad \textit{eq. 2.6}$$

Integration of the equation establishes the relationship between the differential mass element dm and the whole catalyst bed:

$$\int_0^m \frac{dm}{\dot{V}_{i_{in}}} = \int_0^{X_m} \frac{dX_i}{-r_i} \qquad \textit{eq. 2.7}$$

In order to easily determine the reaction rate, the experiments have to be conducted under differential reaction conditions and conversions. These are met, if the conversion of the reacting educts is equal or smaller than 15 %. The low conversion also helps to maintain a constant temperature, even under strong exo – or endothermic reactions. When ensuring small conversions of the reaction educts, the reaction rates, concentrations of the educts and volumetric flow rates along the catalyst bed can be assumed as constant, which leads to:

$$\frac{1}{\dot{V}_{i_{in}}} \cdot \int_0^m dm = \frac{1}{-r_i} \cdot \int_0^{X_m} dX_i \qquad \textit{eq. 2.8}$$

Integration of eq. 2.8 yields:

$$r_i = -X_m \frac{V_{i_{in}}}{m} \qquad \textit{eq. 2.9}$$

For CO the equation above would result in:

$$r_{CO} = -X_m \frac{V_{CO_{in}}}{m} \qquad \textit{eq. 2.10}$$

The conversion of other components taking part in the reaction is calculated in the same way as written above.

For CO_2 this results in:

$$X_{CO_2} = \frac{c_{CO_{2in}} - c_{CO_{2out}}}{c_{CO_{2in}}} = 1 - \frac{c_{CO_{2out}}}{c_{CO_{2in}}} \qquad \textit{eq. 2.11}$$

for CH_4 :

$$X_{CH_4} = \frac{c_{CH_{4in}} - c_{CH_{4out}}}{c_{CO_{in}} + c_{CO_{2in}}} = X_{CO} + X_{CO_2} \qquad \textit{eq. 2.12}$$

The CO selectivity is calculated by the following equation:

$$S_{CO} = \frac{c_{CO_{in}} - c_{CO_{out}}}{c_{CH_{4in}} - c_{CH_{4out}}} \cdot 100\% = \frac{X_{CO}}{X_{CH_4}} \cdot 100\% \qquad \textit{eq. 2.13}$$

2.1.3 Gas mixing unit

All instruments used for the *in situ* investigation of the selective methanation of CO (plug flow reactors connected to the GC or MS, the DRIFTS or the XAS reaction cell) were connected to a gas mixing unit, which allowed experiments with four different gases and flow rates up to 200 Nml·min^{-1}. Four mass flow controllers (MFC), which were connected with the gases (CO, CO_2, H_2, N_2, CH_4), adjusted the gas flow. The gases were intermixed after passing the MFCs prior to entering the reactor. Subsequently they were fed to the detection system. During bypass measurements the intermixed gases did not flow through the reactor prior to entering the detection system. This was adjusted by a four port valve. Details on the gas mixing units can be found in [84].

For the *in situ* XAS measurements, a small transportable gas mixing unit (Figure 2 and Figure 3) was built, including six digital mass flow controllers (Bronkhorst), which were controlled via a computer program (FlowView, Bronkhorst). The principal set-up is similar to the gas mixing units used for DRIFTS or kinetic measurements. Figure 2 shows a schematic description of the gas mixing unit. This set-up allowed the use of two XAS *in situ* cells simultaneously, e.g., one for pre-treatment and one for measurements under idealized conditions (maximum of three MFC per cell). For experiments under realistic conditions, one cell could be connected to four MFCs. This was achieved by switching one mass flow controller from one side via three port valves to the three MFCs on the other side.

Table 9 (see appendix) summarizes the different MFCs for the different experimental stations.

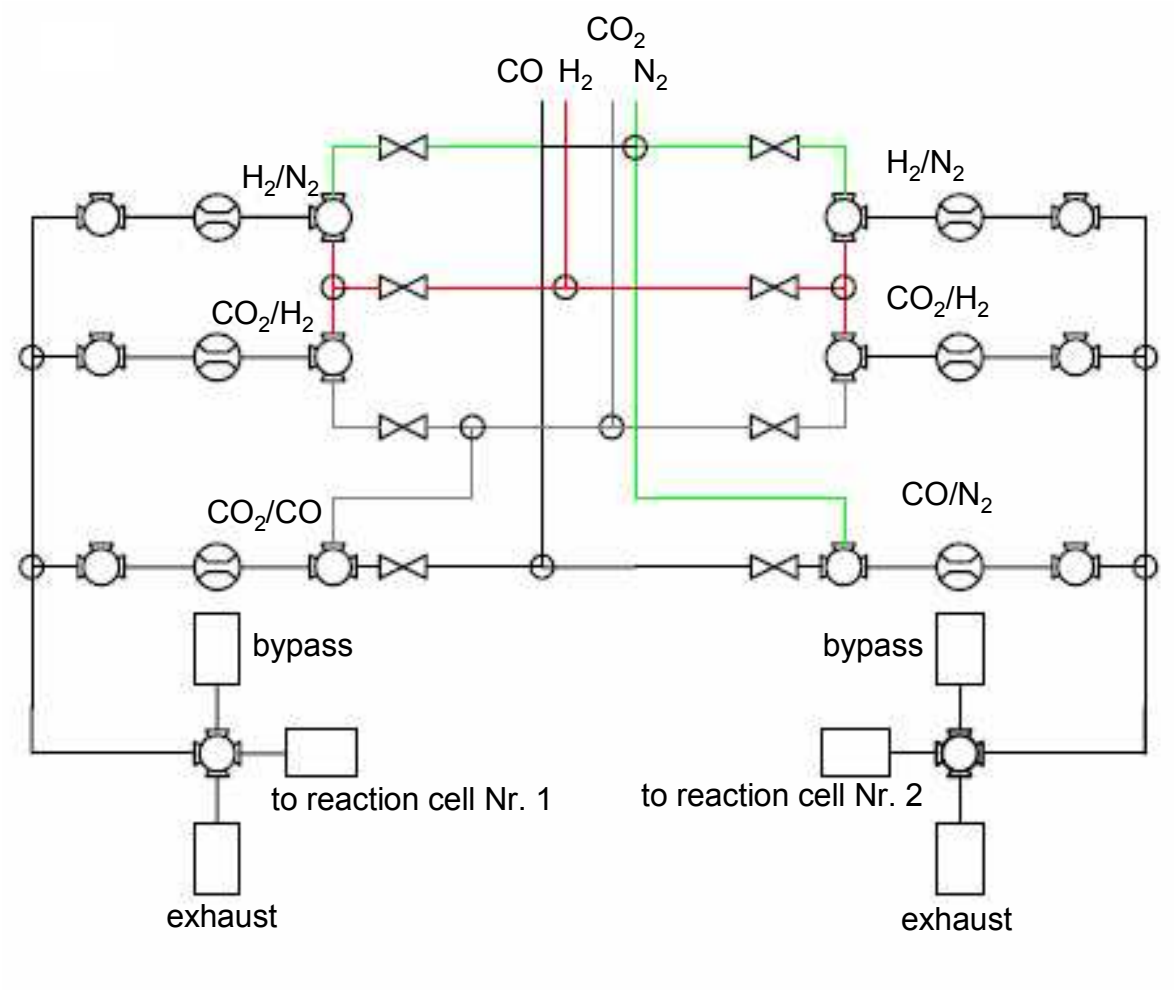

Figure 2: Sketch of the portable gas mixing unit

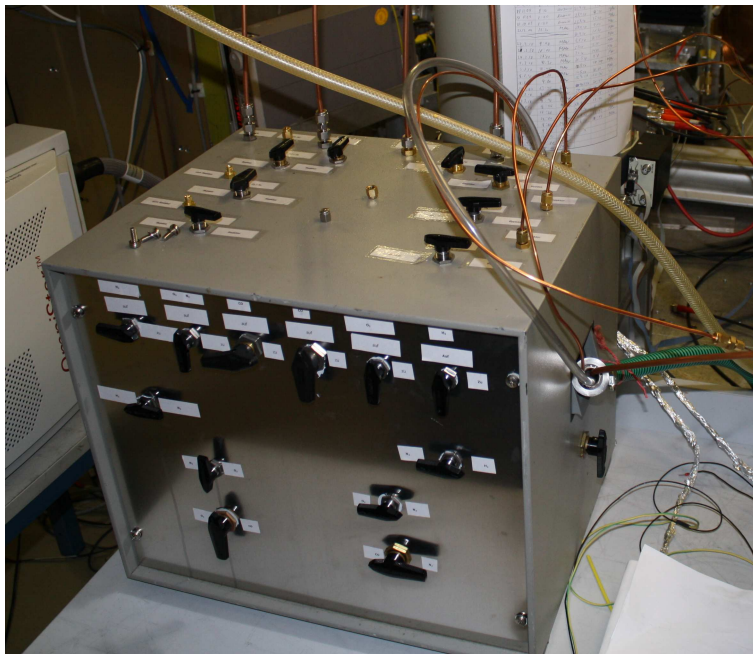

Figure 3: Portable gas mixing unit

2.1.4 Gas Chromatograph (GC)

The effluent gases were analyzed with a GC from DANI (Model 86.10HT). The components were separated in two packed stainless steel columns, where one was packed with a polymer (Hayesep Q) and the other one with a mole sieve (5 Å). First the content of the sample loop (1.5 ml) was eluted onto the polymer column, where CO_2 and water were separated from O_2, N_2, CH_4 and CO. The latter components were subsequently directed onto the polar column, and a four way valve connected both columns to thermal conductivity detectors (model TCD 86/40 from DANI). Hydrogen as a carrier gas, with a flux of 20 $ml \cdot min^{-1}$, enhanced the TCDs' sensitivities compared to N_2, therefore its concentration in the feed gas could not be detected. The oven temperature was set to 60°C and the detector temperature to 140°C, which assured the best efficiency for separation of the components and for the measurement time (15 min per run). For more details see [82]. The calibration of peak areas (GC) or signal intensities was performed using a calibration gas of known composition (1% CO_2 (4.5), 1% CO (3.7), 0.5% CH_4 (3.5), 1% O_2 (5.0), 21.5% N_2 (5.0), balance H_2 (5.0)) from Westphalen.

2.1.5 IMR / MS

In another way of analysing the effluent gases I used an Ion Molecular Reaction Mass Spectrometer (IMR / MS); Atomika IMR-MS SP89. This apparatus was installed by S. Hackenberg [85] and later modified by R. Leppelt [86]. Here, reaction gas ions (Kr^+ and Xe^+) are used for ionization of the effluent gas composition. There are two advantages of such kind of system compared to GC measurements: (i) the high time resolution (10 s) and (ii) the fact that components with ionization energies larger than the electron affinity of Xe^+ and Kr^+ (e.g. H_2 and N_2) are not ionized, which allows quantitative detection of CO in the presence of N_2. Additionally, a low fragmentation probability for, e.g., CO_2 is observed, since moderate ionization energies are applied (Xe^+: 12.13 eV and Kr^+ 14.00 eV). The ionization gases were dosed from a 1:1 mixture of Xe and Kr (Linde) via a leak valve (VTI). This led to a pressure in the analysis chamber of $8 \cdot 10^{-6}$ mbar. Feeding the analyte gas through a polymer capillary (ID 0.2 mm), which was connected via a T connector to an oil pump and the MS system, increased the chamber pressure to $5 \cdot 10^{-6}$ mbar (typical experimental conditions). The calibration of the mass ratios was performed using a calibration gas of known composition (1% CO_2 (4.5), 1% CO (3.7), 0.5% CH_4 (3.5), 1% O_2 (5.0),

21.5% N_2 (5.0), balance H_2 (5.0)) from Westphalen. For a detailed description of the system see [85;86].

2.2 Transmission Electron Microscope (TEM)

All TEM images presented in this work were recorded by Dr. J. Biskupek (Ulm University) on a Philips CM20 200KV equipped with a CCD camera. It is a powerful technique to visualize particle sizes and catalyst morphologies [87;88]. In principle, an electron beam passes through a condenser where parallel rays are produced. An aperture controls the size of the illuminated sample. Those electrons, passing in parallel through the sample, produce an image, after passing several lenses and the "backfocal plane". This small intermediate image passes through several lenses which magnify the image. Subsequently it is displayed on a fluorescent screen [89]. A two dimensional grey scale projection is formed by the transmitted electrons, where the grey scale levels result from the attenuation of the beam, which in turn depends on the weight of the element, thickness of the sample and oxidation state of the elements. This is called a bright field image. The Ru/Zeolite catalyst contains particles below 1 nm in size, which are essentially invisible to TEM at least for this instrument. In addition, the zeolite matrix was found to decompose under the focused electron beam, resulting in images with low resolution. Therefore, an evaluation of the Ru particles was not possible. For the Ru/Al_2O_3 catalyst, TEM characterization was possible, since the Ru particle sizes were sufficiently large and the support was stable under the electron beam. In order to obtain a reasonable statistics, at least 200 particles were evaluated with the 'i-TEM' program. The average particle size is needed for the calculation of their dispersion on the catalysts support (see section 2.6), so that a turn-over frequency (TOF) can be calculated.

2.3 X-ray Photoelectron Spectroscopy (XPS)

XPS is commonly and widely used to obtain information on the elemental composition of surfaces and on the oxidation state of the particular elements in catalysis and surface science [90-92]. The spectra presented in this work were recorded by Dr. S. Kielbassa and Dr. T Diemant with a PHI 5800 ESCA system using monochromatized Al-Kα radiation (1486 eV). In principle, the kinetic energy of the photo electrons is measured after excitation of core level electrons by X-rays. The kinetic energy is converted into a binding energy, which is element specific.

$$E_b = h \cdot \nu - E_{kin} - \phi \qquad \textit{eq. 2.14}$$

E_{kin}: kinetic energy of the photoelectron

E_b: binding energy of the photoelectron

ϕ: work function of the spectrometer

ν: frequency of the exciting irradiation

h: Planck's constant

All spectra were recorded with a power of 250 W, an emission angle of 45° and with an aperture size of 4 mm (acceptance angle ±5°, sampled size 1 mm). The detail spectra of the elements of interest, here Ru, O, Si, Al and C, were recorded with a pass energy of 23.5 eV. The scanning time differed, depending on the catalyst. For the characterization of the Ru/zeolite catalyst, the measurement times were about 60 hours, in order to get an acceptable signal to noise ratio. For the Ru/Al_2O_3 catalyst the respective measurement time was only 6 hours. Neutralization of the powder samples was achieved by an electron gun with an emission current of 20µA. The fitting parameters (FWHM: Full width at half maximum) for the Ru signals were determined by measuring RuO_2 and a metallic Ru single crystal under identical conditions. Shirley background subtraction [91] and peak fitting were performed using a public XPS peak fit program (XPSPEAK4.1). In order to remove shifts due to surface charging effects, the binding energies were calibrated using the C (1s) peak as reference (284.4 eV). Due to the interference of the C (1s) peaks with the Ru (3d) signals, fits of the Ru (3p) peaks were performed based on the following assumptions:

The peak positions for Ru^0 and for Ru^{4+} corresponds to 461.3 and 462.3 eV respectively [93]. The spin orbit splitting between $Ru(3p_{3/2})$ and $Ru(3p_{1/2})$ was 22.2

eV [93-95]. The intensity of the Ru($3p_{1/2}$) is half the intensity of the Ru($3p_{3/2}$) signal. The FWHM is constant for all peaks and the Gauss-Lorentz ratio was not changed.

2.4 X-Ray Diffraction (XRD)

Catalyst properties as well as particle sizes of metallic nanoparticles can be studied by XRD. This technique is based on the interference of X-rays upon passing through a crystalline lattice where the diffracted radiation results in a diffractogram [89]. A Co source is used to produce Co Kα radiation (electron acceleration voltage: 40.00 keV, 35 mA). If the diffracted plane waves are in phase, this results in constructive interference and maxima are detected in the diffractogram. These signals allow the evaluation of particle sizes via the Debye-Scherrer equation.

$$< L >= \frac{K * \lambda}{\beta * \cos\theta} \qquad \textit{eq. 2.15}$$

where:

- <L>: Measure for the dimension of the (single crystalline) particle in the direction perpendicular to the reflecting plane
- λ: X-ray wavelength
- β: Peak width
- θ: Angle between the beam and the normal on the reflecting area
- K: Constant (0.9)

The XRD diffractograms were recorded and evaluated by Lionel Kroner at the Institute of Micro and Nano Materials, Ulm University, using a Philips X'PERT D5000 diffractometer and the X'PERT Highscore Plus program.

2.5 Hydrogen chemisorption

The H_2 chemisorption is a widely used indirect technique to assess the catalytically active surface area of supported catalysts [96;97]. This method provides, besides X-ray spectroscopic, diffractometric or electron microscopy techniques (XAS, XRD or TEM) the possibility to obtain the metal dispersion and subsequently a mean particle size. In principle, the catalyst characterization by H_2 chemisorption is based on the identification of the amount of adsorbed H_{ad} which is necessary to cover the catalyst's active surface by a monomolecular chemisorbed atomic layer (see also DIN 66166). On the basis of this amount and under consideration of a defined stoichiometry of the adsorbates and metal atoms (for H_{ad} on metals at RT: 0.7) it is possible to calculate the specific active surface of the catalyst sample. If the geometric parameters of the active particles are known, it is possible to calculate an average metal (Ru) particle size.

However, in most cases these parameters are estimated, especially when disperse catalysts are used, which may result in an overestimated active particle size and thus in low dispersions. Normally, spherical or hemispherical particles are assumed [97]. The resulting particle sizes and dispersions obtained by this technique represent the active surface area, which is accessible to the adsorbents and is not necessarily identical to the whole particle surface area. Therefore the results (dispersions) may differ when comparing to TEM or XAS derived dispersions, since the last two techniques consider the whole particle as active surface.

Static volumetric H_2 chemisorption isotherms on Ru supported catalysts were measured by Dr. Volker Hagen and Susanne Buse (Univ. Bochum) using an Autosorb 1C (Quantachrome, USA) machine. The catalysts were pre-treated *in situ* under a flowing H_2 stream (20 Nml·min^{-1}, H_2 grade 6.0) at 200°C for 3h. Subsequently the catalyst was evacuated to UHV conditions and the temperature was lowered to 25°C. Afterwards, defined amounts of H_2 were introduced stepwise to the sample cell. These amounts can be converted into a pressure, which would occur, if no sample was present. The difference between the pressure calculated by this way and the pressure measured after admission, leads to the adsorbed amount of H_2 on the catalyst. The measurements were conducted in a range between 80-800 Torr. The obtained isotherm contains contributions of physisorbed and chemisorbed H_{ad} on the active surface. Additional evacuation and remeasuring of the same

catalyst results in the amount of only physisorbed H_{ad}, since the chemisorbed H_{ad} will still be present on the catalyst. Subtraction of the two values gives the amount of chemisorbed hydrogen atoms, which correlates with the active surface area. The latter is calculated from the known catalyst loading and the assumption of 70% H_{ad} coverage and a Ru atom cross-section of 8.17Å^2 [98]. The data evaluation was performed using the Quantachrome software package.

2.6 Dispersion and TOF calculation

For catalyst characterization and comparison it is important to gain information on the dispersion to calculate a mass and molar independent reactivity. A frequently used unit is the turnover frequency, which displays the reactivity of a catalyst to convert an educt per time (TOF). For the calculation of the catalyst's dispersion it is inevitable to know the particle size of the catalytically active species (here: Ru particles), which can be measured by the techniques discussed above. Bergeret et al. [97] suggested that the dispersion of small particles (< 2 nm) depends to a great extent on the particle shape. In case of Ru model catalysts, the particle shape can be investigated easily and therefore taken into account for the dispersion calculation. It is however almost impossible to investigate the particle shape of the active metal on dispersed catalysts, especially when the particles are very small (≤ 1 nm). Due to these reasons a hemispherical particle shape is assumed for the dispersed catalysts investigated (as it is done by numerous research groups), even for the ones with very small nanoparticles (2.2 wt.% Ru/zeolite, 0.9 nm particle diameter), in order to be comparable to former publications [98]. The dispersion can be calculated as follows [88].

$$S_{particle} = \frac{4 \cdot \pi \cdot r^2}{2} \qquad \textit{eq. 2.16}$$

$$V_{particle} = \frac{4 \cdot \pi \cdot r^3}{6} \qquad \textit{eq. 2.17}$$

$$N_{'surface-atoms'} = \frac{S_{particle}}{C_{atom}} \qquad \textit{eq. 2.18}$$

$$N_{'volume-atoms'} = \frac{V_{particle}}{V_{atom}} \qquad \textit{eq. 2.19}$$

$$D = \frac{N_{'surface-atom'}}{N_{'volume-atom'}} \qquad \textit{eq. 2.20}$$

where:

$S_{particle}$: mean particle surface

$V_{particle}$: mean particle volume

r: mean particle radius

$N_{'surface\text{-}atoms'}$ number of surface atoms

$N_{'volume\text{-}atoms:'}$ number of volume atoms

C_{atom}: Ru atom cross-section

V_{atom}: volume of a Ru atom

D: dispersion

For the Ru atom cross-section the same value as in the H_2 chemisorption measurements is taken ($8.17A^2$) [98].

A dispersion close to 1 represents a small cluster, where all atoms are surface atoms, whereas a lower dispersion denotes the fraction of surface atoms relative to all volume atoms.

The turnover frequency, as a molar and mass independent unit, is calculated as follows:

$$TOF = \frac{r \cdot M_{Ru}}{D} \qquad \textit{eq. 2.21}$$

whereas:

TOF: turnover frequency [s^{-1}]

r: reaction rate $\left[\frac{mol}{g_{Ru} \cdot s}\right]$

M_{Ru}: molar mass Ruthenium $\left[\frac{g}{mol}\right]$

D: dispersion

2.7 Diffuse Reflectance Infrared Fourier Transform Spectroscopy (DRIFTS)

In situ IR measurements were performed in a DRIFTS configuration with a Magna 6700 spectrometer (Thermo Fisher), equipped with a MCT narrow band detector and a commercial *in situ* reaction cell unit from Harricks (HV-DR2) at atmospheric pressure. This common set-up allows measurements under flowing reaction atmospheres, comparable to the conditions in a plug-flow micro reactor, and at elevated temperatures (maximum 400°C). About 25 mg of catalyst mass diluted 1:5

with α-Al_2O_3 (Aldrich Al_2O_3 fused 325 mesh, 99+%) were used in each experiment. This resulted in an optimum reflectivity value to assure a maximum signal-to-noise ratio. Typically, 20 scans (acquisition time 9 s plus 3 s for data saving) at a nominal resolution of 4 cm^{-1} were added for one spectrum under conditions where fast changes (reaction transients) were expected (first 10 min of reaction). Subsequently 400 scans (acquisition time 4 min 8 s plus 3 s for data saving) at a nominal resolution of 4 cm^{-1} were added for one spectrum, under conditions, where changes in the build up of surface products are expected to be small (~steady-state conditions). Prior to the experiments, background spectra were recorded on the freshly heated catalyst at 150°C under pure N_2 flow (41.6 Nml·min^{-1}). Subsequently, the gases were switched to reaction atmosphere and heated to the reaction temperature (190°C). Afterwards, the reaction spectrum is divided by the background spectrum to obtain a DRIFTS spectrum. The changes in reflectivity due to the small temperature difference were negligible as they only had a marginal influence on the evolving signals. The intensities were evaluated in Kubelka Munk units, which are linearly related to the adsorbate concentration [99-102]. For further details on the apparatus and the theory I refer to the PhD thesis of M. Schubert [84].

The Kubelka Munk function is defined as:

$$f(R_\infty) = \frac{(1-R_\infty)^2}{2 \cdot R_\infty} = \frac{K}{s} \qquad \textit{eq. 2.22}$$

where :

$f(R_\infty)$: Kubelka Munk function

R_∞: diffuse reflection of an infinite thick sample

K: absorption coefficient

S: scattering coefficient (constant in most cases)

R_∞ is defined as

$$R_\infty = \frac{I_\infty(sample)}{I_\infty(background)} \qquad \textit{eq. 2.23}$$

The linear relationship between the Kubelka Munk function (signal intensity) and the concentration of the adsorbate is given by the absorption coefficient (K), which can also be written as

$$K = const. \cdot \varepsilon \cdot c \qquad \textit{eq. 2.24}$$

where

ε: absorption coefficient of the analyte

c: concentration of the analyte

For weakly adsorbed species (relative reflectivity larger 0.6) Sirita et al. [101] suggested a different evaluation. In their work, the reflectivity is defined as follows:

$$R' = \frac{R}{R_\infty} \qquad \textit{eq. 2.25}$$

$$R = \frac{I_{cat+ad}}{I_0} \qquad \textit{eq. 2.26}$$

$$R_\infty = \frac{I_{cat}}{I_0} \qquad \textit{eq. 2.27}$$

where

R': relative reflectivity

I_{cat+ad}: intensity during reaction

I_0: intensity of a nonabsorbing sample (mirror)

I_{cat}: intensity of the background

The resulting spectra are presented in log(1/R') vs. wave number. Since the adsorbed species reported and discussed in this work do not comply (relative reflectivity is lower than 0.6) with the preconditions of Sirita et al. all spectra presented here are evaluated with the Kubelka Munk function.

2.8 X-ray Absorption Spectroscopy (XAS)

X-ray Absorption Spectroscopy (XAS) is a powerful technique which allows elucidating catalyst changes during reaction (*in situ)*. The most valuable information obtained from these experiments is the chemical composition and the electronic structure of the catalyst. In principle, XAS probes the local structure around all atoms of a particular element at any temperature and pressure. Information on the number of neighbors, atom-atom distances and disorder can be derived which allows to reconstruct the structure. Additionally, XAS spectra give information on the local density of states as the total number of unfilled states in the valence band is proportional to the integrated area of the absorption edge [103]. However, since in XAS experiments all atoms of one species contribute to the resulting spectrum, the information gained is only an average over all contributions. In the following, a short introduction on how synchrotron radiation is produced will be given. Next, the theory of the electron transition and EXAFS (Extended X-ray Absorption Fine Structure) is explained and in the last part of this section the evaluation of the raw data will be described.

2.8.1 Technical preconditions

A precondition to perform XAS experiments is the availability of tuneable, high brilliance X-rays. These conditions are met at electron storage rings, where radiation is generated by acceleration of electrons or positrons, which move at a circular track forced by deviation magnets. Once these particles have been accelerated to near the speed of light in accelerator rings, they are transferred to a storage ring, where the high energy of the particle is kept constant. This corresponds to a steady acceleration of the particles to the center of the circuit; the necessitated additional kinetic energy for the acceleration is emitted by the particles tangent in form of broad energetic radiation (Figure 4) [104].

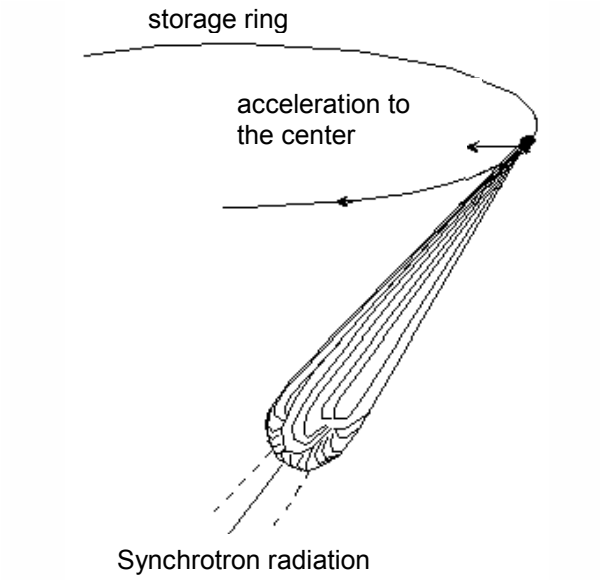

Figure 4: Sketch of the tangent emitted synchrotron radiation

Due to the acceleration with high frequencies, the charged particles are concentrated into small bunches. Radiation is only emitted when a respective bunch passed the respective section of the storage ring. With the use of special insertion devices (Undulators) [104], the synchrotron radiation can be enhanced, by forcing the electron bunches on a sinusoidal track. This additional acceleration results in an enhanced radiation. Undulators consist of dipole magnets, which are periodically arranged with alternating polarity. The principle of an undulator is shown in Figure 5.

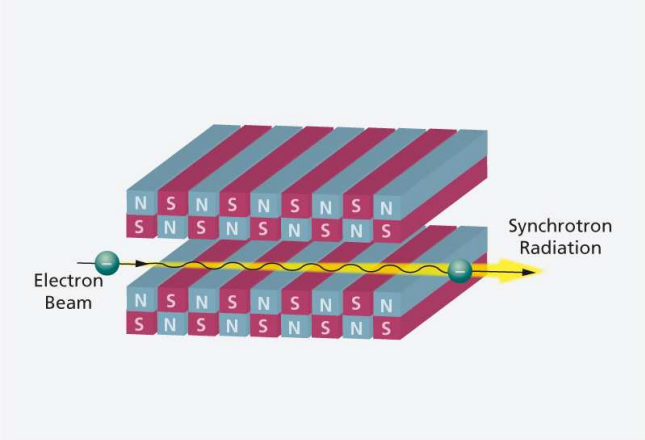

Figure 5: Sketch of an insertion device and the generation of synchrotron radiation taken from [105]

An undulator, due to its relatively weak deviation, generates coherent small band radiation. The radiation (photons) is emitted into a small opening angle, thus causing constructive interference of the radiation cones, which leads to a high intensity and brilliance. Subsequently, a monochromator narrows the broad energy distribution to

the required energy range, and the beam is focused onto the sample. For more details see [104].

2.8.2 Physical principles of the electron transition

The basic principle of X-ray Absorption Spectroscopy is the interaction of photons with matter. When an X-ray photon penetrates matter, elastic and inelastic interaction between radiation and electrons of the atoms occur in addition to photoabsorption. Therefore, the intensity of the incoming beam is reduced after passing through matter. X-ray radiation is usually continuously absorbed along the energy spectrum, and at specific energetic values a discontinuity (absorption edge) can be observed where the absorption signal increases steeply (Figure 6).

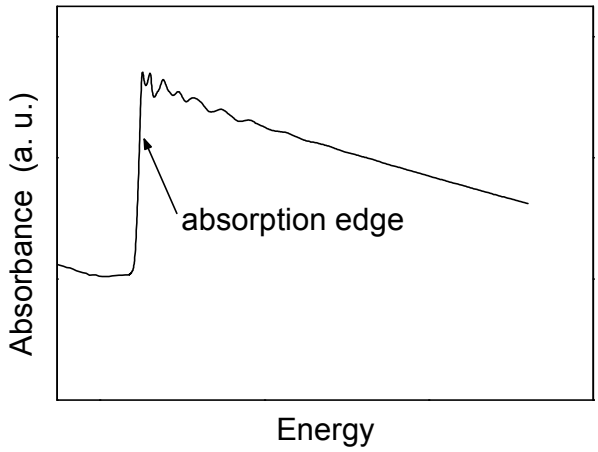

Figure 6: Sketch of K-edge absorption of Ru

Mathematically, the probability $\Gamma_{i\to f}$ of exciting an electron from an occupied initial state (i), given by the wave function Ψ_i, to an unoccupied final state (f) (with wave function Ψ_f) is given by Fermi's Golden rule; it is proportional to the X-ray absorption coefficient (μ(E)):

$$\Gamma_{i\to f} = \frac{2\pi}{\hbar} \times \left| \left\langle \Psi_f \left| \hat{\mathrm{H}}_{\mathrm{int}} \right| \Psi_i \right\rangle \right|^2 \times \rho(E_f) \times \delta(E_f - E_i - \hbar\omega) \qquad \textit{eq. 2.28}$$

The δ function describes the energy conversation for the absorption process (i.e. $E_f - E_i = \hbar\omega$), $\rho(E_f)$ the density of states directly above the Fermi level. The excitation probability is proportional to the transition matrix element $\left| \left\langle \Psi_f \left| \hat{\mathrm{H}}_{\mathrm{int}} \right| \Psi_i \right\rangle \right|^2$, where $\hat{H}_{\mathrm{int}}$ describes the perturbation caused by the incident X-rays.

The interaction operator is approximated by the coulomb gauge:

$$\hat{H}_{\text{int}} \approx -\frac{e}{m_e} A \cdot p \qquad \textit{eq. 2.29}$$

$$p = -i\hbar\vec{\nabla} .$$

where p represents the electron momentum operator and A describes the vector potential of the electromagnetic field. The vector potential is described by:

$$A(r,t) = eA_0\left[\exp\{i(k\cdot r - \omega t)\} + \exp\{-i(k\cdot r - \omega t)\}\right] \qquad \textit{eq. 2.30}$$

Here, '$\vec{e}$' represents the polarization vector of the field. From those terms, only the left one ($e^{-i\omega t}$) is important, as it describes the absorption process. Developing this term in a Taylor series results in:

$$A(r,t) = e\cdot A_0\left[\exp\left\{-i\omega t\left(1 - ik\cdot r + \frac{1}{2}(ik\cdot r)^2 + \ldots\right)\right\}\right] \qquad \textit{eq. 2.31}$$

The resulting equation describes the electrical dipole, electrical quadrupole and magnetic dipole transitions. In the dipole approximation only the first term is considered. Therefore inserting equation 2.31 and 2.29 in equation 2.28 results in:

$$\Gamma_{i\to f} = \frac{2\pi}{\hbar}\left(\frac{-e}{m_e}\right)^2 |A_0|^2 \times \left|\langle \Psi f | e\cdot p | \Psi i\rangle\right|^2 \times \rho(E_f) \times \delta(E_f - E_i - \hbar\omega) \qquad \textit{eq. 2.32}$$

which shows the details of the interaction operator. It consists of the final state, the electron momentum operator and the vector potential, which define if a transition is allowed or not [106], [104]. As the final state is defined as

$$\Psi_f = \Psi_{outgoing} + \Psi_{backscattered} \qquad \textit{eq. 2.33}$$

and both contributions to the final state are a function of energy of the incident beam, the transition probability Γ is not a smooth function above the absorption edge, but results in maxima and minima that constitute the EXAFS signal.

2.8.3 XAS spectrum (XANES and EXAFS)

The spectrum can be separated into different regions. The region from 200 eV before the edge to the edge is called the pre-edge region, the region from the edge to 150 eV above the edge is defined as the Near Edge region and the region of the Extended X-ray Absorption Fine Structure (EXAFS) region ranges from 150 eV after the edge upwards. XANES spectra gain more qualitative information on the electronic properties, e.g. on the oxidation state, the density of states in the d orbital etc., whereas EXAFS spectra give quantitative information on the structural parameters of the investigated particles (no. of nearest neighbors, bond lengths).

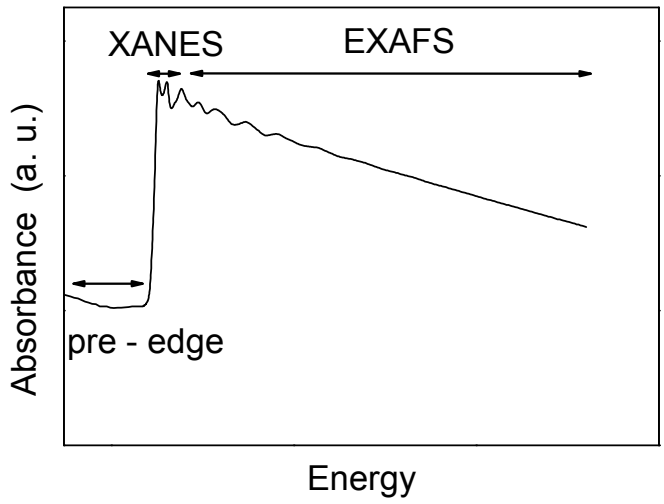

Figure 7: Sketch of an XAS spectrum

The sudden increase of the absorption at a specific energy is due to the fact that at this point the photon energy is sufficiently high, that excitation of a core electron of the absorbing atom into the lowest unoccupied state above Fermi level becomes feasible. This energy jump is defined as edge jump. Since it is not always straight forward to define the exact position of the edge, the exact energy value is given by the inflection point of the curve. There are different types of edges, e.g., L_1, L_2 and L_3 (L-edge), where electrons from the 2s, $2p_{1/2}$ and $2p_{3/2}$ levels are exited. An electron exited from 1s core level is called a K-edge signal (Figure 8). These transitions follow selection rules: the dipole selection rule $\Delta l = \pm 1$, the quadrupole selection rule $\Delta l = \pm 2$. Measurements at the L_2/L_3 edge give information on the DOS of the d orbitals and the oxidation state, since transitions from 2p to nd are allowed. Experiments at this edge can only be performed, if the spin-orbit splitting is large enough, otherwise

EXAFS experiments are not possible (only XANES, as for Ru). Moreover, if the L_2 or L_3 edge energy is below 4 keV, the experiments can only be conducted under vacuum conditions, since absorption of N_2 would be too high otherwise. The measurements presented in this work were measured at the Ru K-edge due to the latter reasons. When measuring at the K edge, only transitions from 1s to np (here: 5p) energy levels are allowed. Hence, no information on the d-band structure can be obtained. However, since the shape of the edge also correlates with the oxidation state of the sample, conclusions on the oxidation state of the sample can be drawn by comparison with known reference compounds.

A pre-edge signal, caused by the transition of an 1s electron to an 4d electron, maybe observed at lower energy values than the K-edge signal, due to the above mentioned quadrupole transitions. These resulting signals are normally two orders of magnitude lower than the electric dipole allowed transition. It may be intensified if a 5p-4d orbital intermixing occurs, due to ligand effects [107]. Therefore this feature strongly depends on the particle conformation [107]. In combination with the XANES region, conclusions on the coordination symmetry and electronic configuration can be drawn [107].

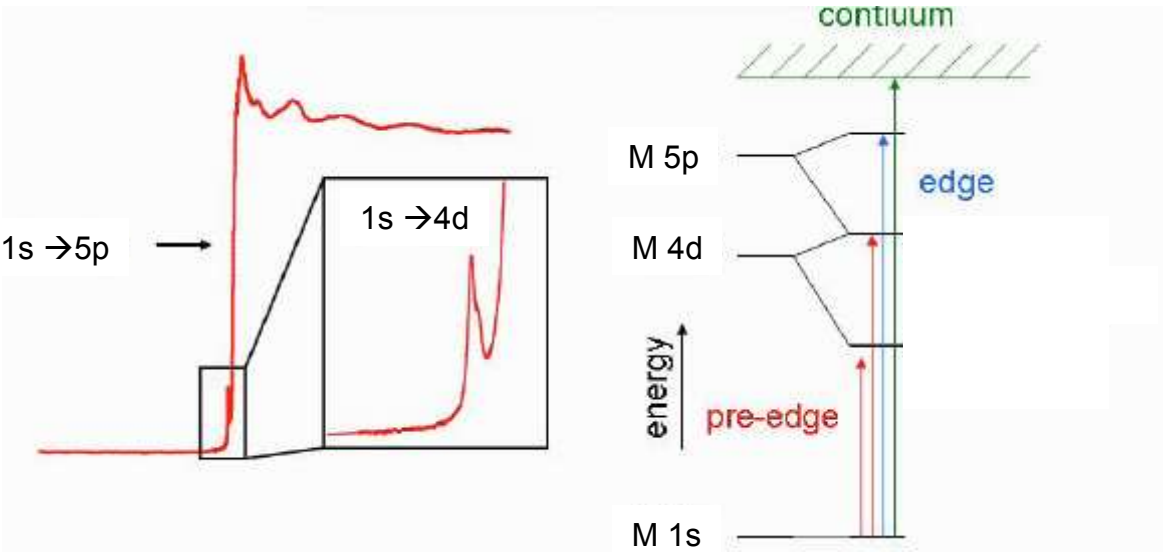

Figure 8: Sketch of a K-edge excitation

At higher energies (150 eV above the edge), in the EXAFS region, a damped sinusoidal fine structure can be observed, which contains information on the structural neighborhood of the absorbing atom [106;108]. The absorption of the EXAFS region is measured over an as wide as possible energy range after the edge

jump (500-1500 eV), in order to gain a sufficiently detailed spectrum. The details of the EXAFS theory will be explained in the next section.

2.8.4 EXAFS: mathematical description

When a photon, defined by the frequency ω, hits matter it is usually absorbed. The degree of absorption in principle follows the Lambert-Beer Law (eq. 2.34) with the absorption depending on the energy of the photons.

$$I_t = I_0 e^{-\mu(E)x} \qquad \textit{eq. 2.34}$$

where μ = absorption coefficient

x = sample thickness

Upon absorption of an X-ray photon by matter an electron with mass m_e may be emitted from a core level (E_b) of the absorbing atom if the photon energy is higher than the edge energy. The kinetic energy (E_k) of the emitted electron is defined by:

$$E_k = \hbar\omega - E_b \qquad \textit{eq. 2.35}$$

In order to describe the following scattering process, the electron is usually regarded as a wave which interacts with neighbouring atoms, resulting in the extended X-ray absorption fine structure (EXAFS). The scattering process (see Figure 9) can easily be described by a wave using the wave particle dualism by de Broglie:

$$\lambda = \frac{h}{\sqrt{2m_e E_k}} \qquad \textit{eq. 2.36}$$

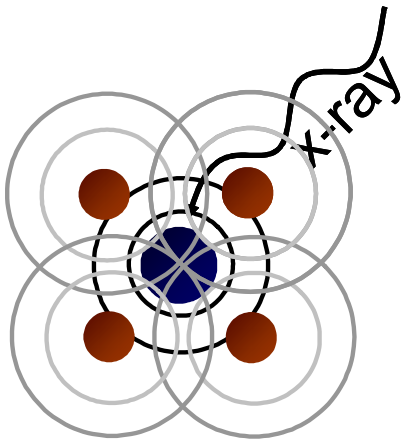

Figure 9: Schematic view of absorption of an X-ray photon; electron wave (black lines) and backscattered wave from neighboring atoms (grey lines)

This wave is scattered from neighboring atoms (backscatterers) and the characteristics of these scattered waves are defined by the properties of the backscatterers. Since the wavelength of the backscattered wave depends on the

kinetic energy of the photoelectron (and thus finally on the incident energy), a dependence of the absorption coefficient on the energy arises from that, resulting in local minima and maxima (constructive and destructive interference) in the EXAFS spectrum [103]. In addition, the EXAFS oscillations depend on the number of neighbors, where a higher density of neighboring atoms result in higher amplitude of the EXAFS oscillation, since more scattering processes contribute to the resulting signal. However, a too dense sample will result in a too high absorption coefficient and eventually in a low signal. Second, if there is a high degree of disorder in the system, i.e., if the scatterers are at different distances, different patterns will be generated, which cause a decrease in the EXAFS amplitude. This, in turn, results in poor quality data, which can hardly be evaluated. The same effect is observed when experiments are conducted at higher temperatures, due to an increased oscillation ($\Delta\sigma$) of the atoms. This interference increases with increasing photon energies; at high energies the EXAFS oscillations decay faster.

The main information gained from the EXAFS signal is the number of backscatterers (N), their distance from the absorber (R) and their displacement given by the Debye Waller factor (σ).

The EXAFS function itself is described as:

$$\chi(k) = \sum_{j}^{N(shells)} N_j F_j(k) \cdot \frac{S_0^2}{kR_j^2} \cdot \exp\left(\frac{-2R_j}{\lambda}\right) \cdot \exp\left(-2\sigma^2 k^2\right) \sin(2kR_j + \varphi_j(k)) \qquad \textit{eq. 2.37}$$

where N: coordination number

σ : Debye Waller factor

S_0^2: damping factor

F_j': scattering power of the neighbor

φ: phase shift

λ: mean free path of the photoelectrons

R: distance between absorber/scatterer pair.

The probability of the scattering processes depends on F_j' (see eq. 2.37), which is element specific and a function of energy [103]. S_0^2 has values between 0.7 and 0.9, since usually between 10% and 30% of the ejected electrons do not contribute to the EXAFS, as they take part in shake up/shake off processes. φ_{eff} describes the phase shift when the electron wave is scattered once by the absorber and once by the scatterer [103]. The local structure around the absorber is described by R

representing the scatterer / backscatterer distance, N the number of neighbors, the intensity decrease of the EXAFS spectrum with increasing disorder of the scatterers is characterized by σ and is sample specific. The remaining parameters in eq. 2.37 are element specific and can be obtained from calculations, tables or extracted from EXAFS spectra of reference compounds [103]. In order to compensate for the sinusoidal damping and to obtain a uniform amplitude, the EXAFS spectra are weighted by a certain factor before the evaluation. For systems with absorbers containing an atomic number Z>36, a k^3 weighting is used. Absorbers with atomic numbers between 36<Z<57, k^2 weighting is applied, and a k^1 weighting is used for higher values of Z. However, a higher weighting causes the noise to increase in spectral regions with higher k values, which has to be accounted for during the fitting process.

2.8.5 Sample preparation and experiment

XAS experiments presented in this work were conducted at HASYLAB (Beamline X1) and ESRF (Beamline DUBBLE) at an energy range of 20917-22117 eV. The EXAFS experiments were performed at the X1 beamline at Hasylab and BM26 at ESRF, using a Si(311) double crystal monochromator and a beam size of approximately 6 mm vertical and 2 mm horizontal. The monochromator was stabilized by a MOSTAB system, which keeps the two monochromator crystals parallel in lateral direction by piezo crystals. The reaction cell consisted of a stainless steel ring with a cylindrical channel (i.d. 4 mm) along the diameter, which contained the catalyst bed (length ca. 10 mm, ~25 mg catalyst, undiluted, conversion <15%) (see Figure 10)

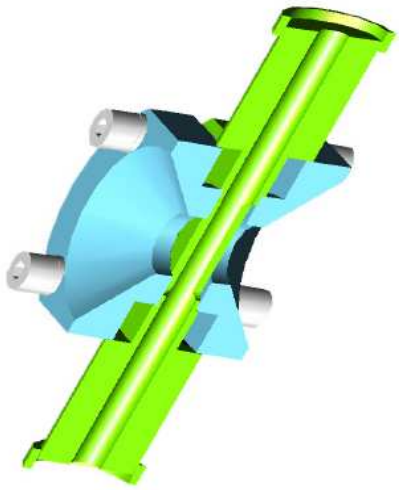

Figure 10: Sketch of the XAS reaction cell

A second bore along the central axis of the ring and perpendicular to the catalyst bed, allowed the X-ray beam to pass through the catalyst bed. In these directions, the reaction cell was closed by two Kapton windows. Sample heating was achieved by 4 wires, which passed through the ring in 4 small bores parallel to the reaction channel. A NiCr/Ni thermocouple was used to monitor the temperature. The reaction cell was placed between two He filled ionization chambers (ic_1 and ic_2) for collecting the spectra at the Ru K-edge (22117 eV) in transmission geometry. A Ru metal foil placed in between the second and a subsequent third ionization chamber (Ic_3) allowed for internal energy calibration during all measurements. A scheme of the set-up is shown in Figure 11. The pre-edge region was measured from 21867-22087 eV, with a step size of 10 eV, for the XANES region from 22087 to 22157 eV, in steps of 0.5 eV, and for the EXAFS region from 22157 to 23317 eV in steps of 0.98 eV.

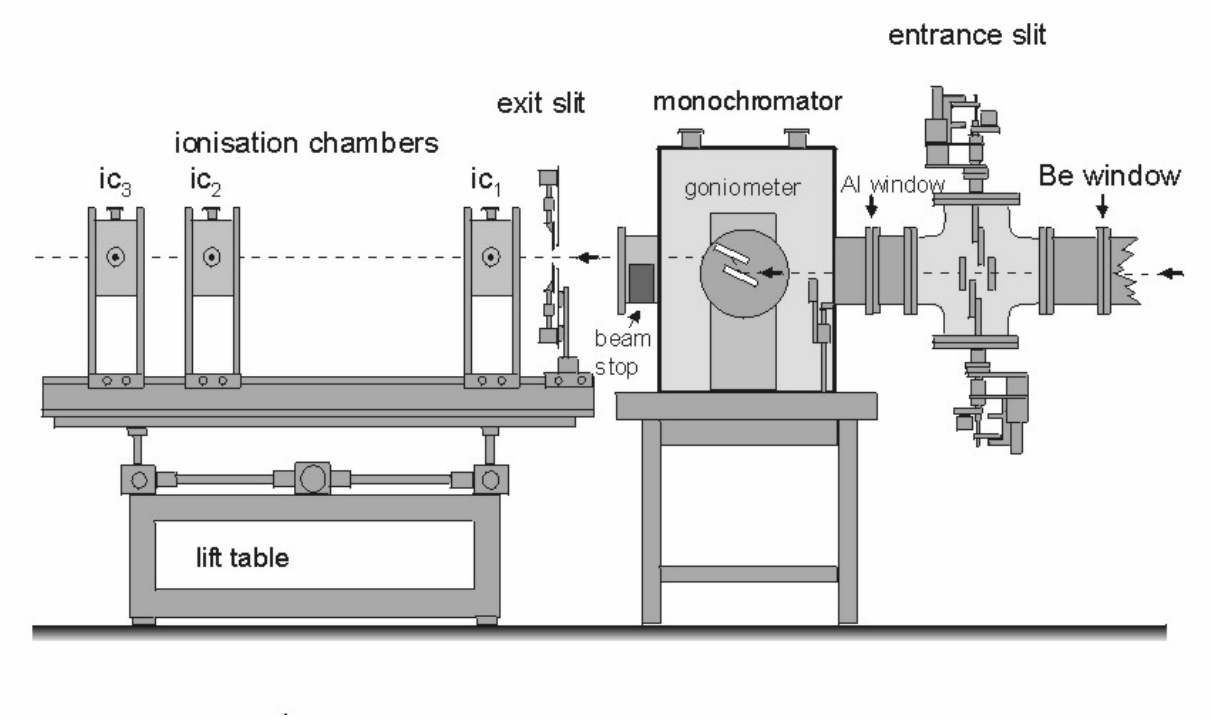

Figure 11: Experimental set-up beamline X1 Hasylab

The *in situ* measurements were conducted with high purity gases (99.999%), which were passed through the reaction cell (gas flow 41.6 Nml min^{-1}). The reaction gas mixtures were prepared via mass flow controllers (Bronkhorst F201C-FA-88V) in a custom made portable gas mixing unit (see section 2.1.3). Prior to the *in situ* experiments, the catalysts were heated up in a N_2 stream to 150°C, and subsequently heated within 10 min to the reaction temperature in the reaction gas atmosphere. The *in situ* EXAFS measurements were performed at 190°C reaction temperature in idealized reformate at atmospheric pressure (0.6% CO, 3% N_2, balance H_2), until steady-state conditions were achieved, but at least for 500 min time on stream (max. 1000 min).

Due to experimental reasons it was not possible to monitor the reaction from the beginning, within the first 2 min of the reaction, since the safety system did not allow valve switching while the beam shutter was open. Therefore the reaction was started and subsequently shutter was opened after all safety features were addressed to. XAS spectra were recorded while monitoring the reaction by a gas chromatograph.

2.8.6 EXAFS evaluation

The evaluation of XAS spectra will be explained in the following section. In principle, the procedure can be separated into three different steps:

(i) Data reduction

(ii) Generation of reference spectra

(iii) Fitting process

All of these steps were performed with the commercially available software 'XDAP'. The calculation of theoretical references was performed with the software ATOMS and FEFF8.0.

(i) Data reduction: Before the EXAFS spectra (sample or reference) can be evaluated, different steps have to be performed in order to obtain a good quality 'pre-edge and background subtracted', normalized EXAFS spectrum. In 'XDAP', all of these steps can be performed under the tab 'data reduction', which opens a menu where the user is guided through a step by step process.

The general principle of the data reduction is described by the following function:

$$\chi(k) = \frac{\mu(E) - \mu(PE) - \mu_0(E)}{\mu_0(E)} \qquad \textit{eq. 2.38}$$

where μ(E): uncorrected spectrum

μ(PE): pre-edge subtracted spectrum

μ_0(E): background subtracted spectrum

(a) Pre-edge subtraction, edge jump and deglitching:

A raw XAS spectrum consists of the sum of:

(i) absorption of other atoms in the sample

(ii) absorption of the probed atom due to absorption at lower edges

(iii) the actual absorption edge, which consists of the atomic absorption and the superimposed EXAFS.

Hence, to obtain the desired EXAFS signal from the measured absorption the 'pre-edge' has to be subtracted from the measured absorption to account for absorption by other atoms and the absorption of lower edges of the probed atom. It is accurately modelled with a Victoreen curve [103]:

$$\mu(PE) = C_1 + \frac{C_2}{E^3} + \frac{C_3}{E^4} \qquad \textit{eq. 2.39}$$

The constants C_1, C_2, C_3 depend on the composition of the sample and the experimental conditions. Therefore, they are determined by the measured absorption before the edge and then extrapolated throughout the complete energy range of the spectrum. Most of the times, the 'normal' Victoreen curve crosses the actual measured absorption at approximately 800 eV above the edge, therefore a modified Victoreen has been introduced where the power of the denominators was reduced to 1 and 2 [103], which was particularly successful. This modified Victoreen curve is commonly used for all EXAFS evaluations. In 'XDAP', the pre-edge subtraction is performed by graphically defining start and end points of the visible pre-edge. According to the modified Victoreen curve explained above, the pre-edge is extrapolated throughout the complete energy range and subsequently subtracted. Figure 12 shows an XAS spectrum before (a) and after (b) pre-edge subtraction.

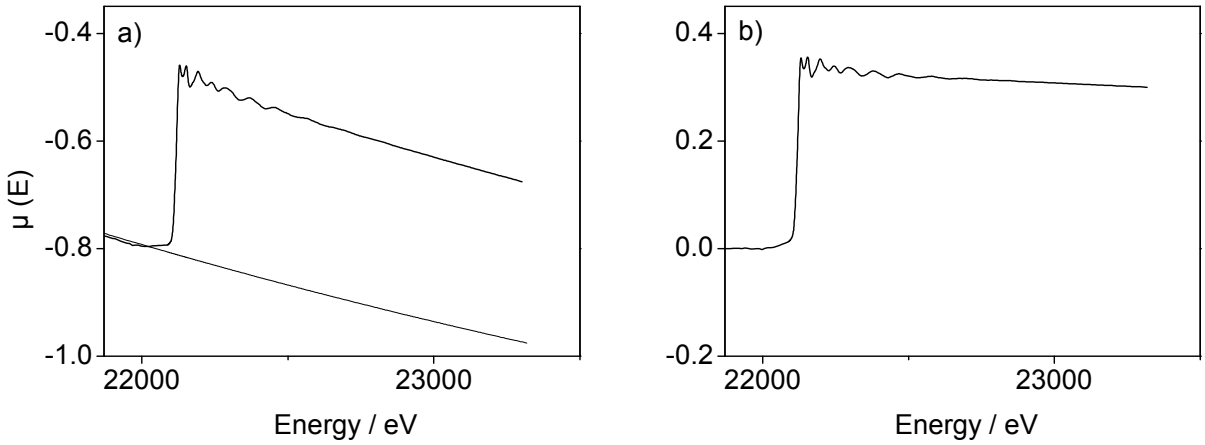

Figure 12: Example of a Ru catalyst (a) before and (b) after pre-edge subtraction

Next, the edge jump has to be defined. As mentioned before, this is commonly done by calculating the inflection point of the edge, which is automatically done by XDAP. However, the program also offers the possibility to define a specific energy as edge jump; subsequently the spectrum is calibrated against this value (Figure 13).

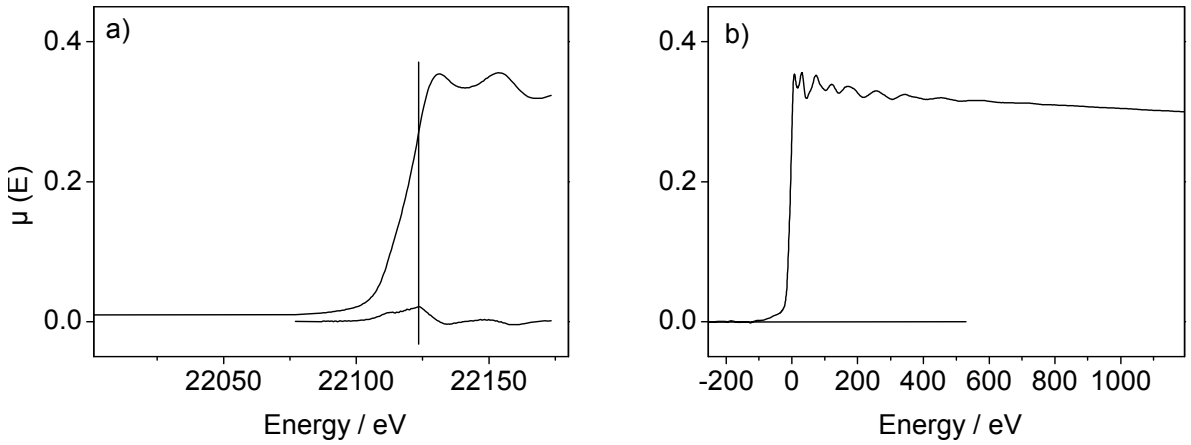

Figure 13: Defining the edge energy (a) before and (b) after calibration

After defining the edge jump, 'XDAP' offers the possibility to erase runaway data points which should not contribute to the EXAFS. This is achieved by 'deglitching' where the raw data is magnified and plotted in parts, that the obviously wrong data points can be identified and deleted.

(b) Background subtraction and normalization: A proper background subtraction is the key to obtain a good description of the atomic absorption. In principle, the applied background represents a single atom which absorbs photons, resulting in a smooth line, since no backscatterers are present. Usually the background is fitted by a polynomial function or by a smoothing spline (as done for the measurements reported in this work) defined by:

$$\sum_{i=1}^{NPTS} \frac{\left(\mu x_i - BCK_i\right)^2}{e^{-WEk_i^2}} \leq SM \qquad \textit{eq. 2.40}$$

where

μx_i: XAS sample spectrum

BCK_i: background

WE: weighting factor

i: NPTS defines start energy and end energy of the background

The background is fitted by SM (smoothing parameter) through the measured data in such a way that the actual signal of interest, in R space, is increased to its maximum, and the obvious noise (region below 1 Å) is minimized [106;108]. The effect on the Fourier transformed XAS spectrum of different smoothing parameters for a Ru system is displayed in Figure 14. It is obvious, that the smoothing parameter for the

cyan and blue coloured spectra is too large (1.2 and 1.1), as they show artificial signals below 1 Å. The green curve exhibits the largest smoothing parameter (1.0) without a prominent signal below 1 Å, whereas the other curves also do not show any artificial signals, but their value for the smoothing parameter is lower. Thus, in the present case 1.0 would be chosen as the smoothing parameter.

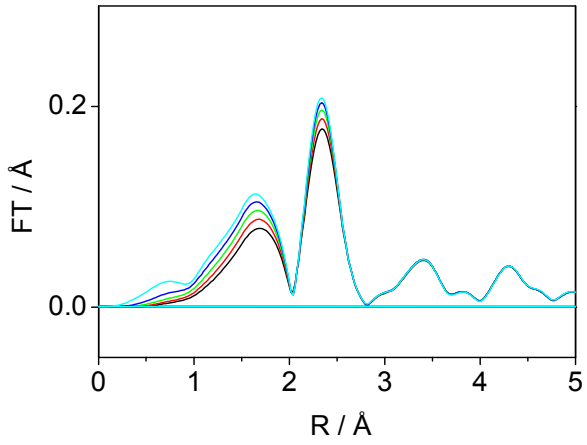

Figure 14: Resulting XAS spectra of a Ru-catalyst (metallic and oxidic) for different smoothing parameters: cyan (1.2), blue (1.1), green (1.0), red (0.9) and black (0.8)

The background subtraction is easy for metallic systems, where the first peak appears at about 2.0 Å. Oxide peaks appear at ~1.5 Å with small side lobes to 0 Å, where a proper background subtraction is more challenging [106].

Normalization of the spectra was performed by division by a value $\mu_0(E)$ of the EXAFS spectrum to convert the EXAFS to a 'per atom' value. In order to obtain consistency from experiment to experiment $\mu_0(E)$ is usually set to a value of 50 eV above the edge [106].

After these steps, 'XDAP' automatically converts the raw data from E space into k space (see Figure 18 left panels). However, the resulting wave function cannot be interpreted without additional mathematic conversion. The subsequent Fourier Transformation into R space (see Figure 18, right panels), which represents a radial distribution function around the absorber atom, is performed in a second step. Thus, information on the distance around the absorber atom, where a high electron density and in consequence backscatterers are present, is gained. Details on the procedure can be found in various publications [103;106;108]. The position of the peaks can be allocated to different backscatterers, whereas the intensity corresponds to the occupation number of the specific shell. The width of the peaks is largely defined by the spot uncertainty and thus by the Debye Waller factor. Due to the fact that the

range of measurement is not infinite but limited, abort effects can occur during the Fourier transformation into R space, which may cause side lobes or a higher noise level. Due to the phase shift, the peaks are normally observed at 0.2-0.5 Å lower distances. This can be corrected by a proper phase correction in 'XDAP'. These characteristics must be addressed while evaluating the spectrum, in order to obtain realistic results.

(ii) Reference spectra:

The section above described the data reduction process for all XAS (sample and reference) spectra, in order to obtain normalized and comparable spectra. For fitting a sample, a reference spectrum needs to be created, which is obtained by measuring a standard sample, here a Ru foil (thickness: 50 µm). If experimental references are measured, the coordination number and interatomic distances must be precisely known, e.g., by X ray diffraction. In that case, the backscattering amplitude, phase shift, damping factor and mean free path λ, are still unknown parameters. However, they can be transferred from one compound (sample) to another (reference) with identical absorber backscatterer pairs and thus the local structure can be accessed [106]. If a reference compound is used for data fitting, its EXAFS spectrum is measured and the X(k) (EXAFS in k space) of a specific absorber backscatterer pair is extracted by means of Fourier filtering. The method works well, if the phase and amplitude of the $X_{ref}(k)$ is well separated from other contributions in the Fourier transform, otherwise errors in the Fourier transformation will affect the fitting results. [106;108]. Moreover, the back transformation into R space for data fitting limits the accurate data range of the backscatterer pair at the beginning and the end of the total k range (Δk = 0.5-1 $Å^{-1}$) due to truncation errors. In addition, the phase shifts and backscattering amplitudes derived from EXAFS data of reference compounds are only reliable (in a good case) for a *k*-range above 3.5 $Å^{-1}$ [106;108]. However, for a precise evaluation, a large k-range is desirable, especially at the lower end. This limits the choice of suitable reference material. Due to these problems, the use of calibrated theoretical references is very effective and commonly used [106]. In addition, their *k*-range is reliable down to 2.0 $Å^{-1}$ [108]. This is of great importance if one is interested in the contributions that show significant intensity in the low k-range or if heavy scatterers dominate the EXAFS [106]. Moreover, the analysis is carried out in R space and therefore the back transformation is unnecessary, thus truncation errors will not affect the fitting.

For the measurements presented in this work, these were calculated by the FEFF 8.0 code, which is a self consistent real space, full multiple scattering code that calculates the X-ray absorption spectrum and the backscattering amplitudes as well as the phase shifts at once [106;108;109]. Prior to the theoretical calculation a FEFF input file was generated by the freeware program ATOMS by Bruce Ravel [110]. This program calculated the Ru atom coordinates until the 5th backscatterer shell with crystallographic data of the reference compound. The ATOMS output file (a normal text file) is read by the FEFF 8.0 program, generating a reference spectrum (feff0001.dat), which is processed by the XDAP program. This calculated theoretical reference is then iteratively calibrated (Debye Waller factor and inner potential should be '0') against the experimentally measured standard. Subsequently, the damping factor S_0^2 (between 0.7 and 0.9) is determined by fitting the resulting coordination number of the measured reference of the first shell to that of the theoretical reference [103;106]. The procedure is consistent with those suggested by Koningsberger et al., Vaarkamp et al. and van Bokhoven [103;106;108]. Additionally, due to the information of the phase shift, these references will correct the phase shift occurring in sample measurements in such way that the respective peaks are observed at their real distances. If no experimental reference is available for calibration, only the theoretical reference can be used for evaluation, which may result in lower accuracy of the fits.

(iii) Data Fitting:

Once the references and the raw data are data reduced and calibrated, data fitting was performed in R space with 'XDAP'. Using the tab 'Analyse' and 'multiple shells' opens a window, where samples, references, phase corrections and different fitting parameters can be loaded (Figure 15). Normally, lambda has a value between 5 and 6 (metallic or oxidic correction factor for N_{cor}), N_{cor} (corrected value) and N represent the number of nearest neighbors, DW depicts the Debye Waller factor, R shows the interatomic distance and E_0 equals the energy offset from 0 eV. Usually, the value for N (nearest neighbors) is underestimated by the normal EXAFS function and therefore is corrected (N_{cor}). C3 and C4 are variables (higher cumulants) used for correction of systems with expected high disorder, e.g., when experiments are performed under high pressures and temperatures [111]. The tab 'Limits' provides access to the upper and lower boundaries for the fitting parameters, which should be adjusted. The tabs 'Combinations', 'Plots', and 'Correlations' provide additional information and

combinations of different fitting shells on the plots and peaks. The tabs 'Progress' and 'Errors' provide statistical information on the goodness of the fit (eq. 2.41) and the specific uncertainty of each fitting parameter (see Table 2). The goodness of the fit is defined as follows [108]:

$$\varepsilon_v^{\,2} = \frac{P}{NPTS(P-p)} \sum_{i}^{NPTS} \left(\frac{\chi^i_{\exp} - \chi^i_{\mathrm{mod}\,el}}{\sigma^i_{\exp}} \right)^2 \qquad \textit{eq. 2.41}$$

P: total number of free parameters

p: number of refined parameters

NPTS: number of points in k-range used for analysis

σ_{exp}: standard deviation of each data point

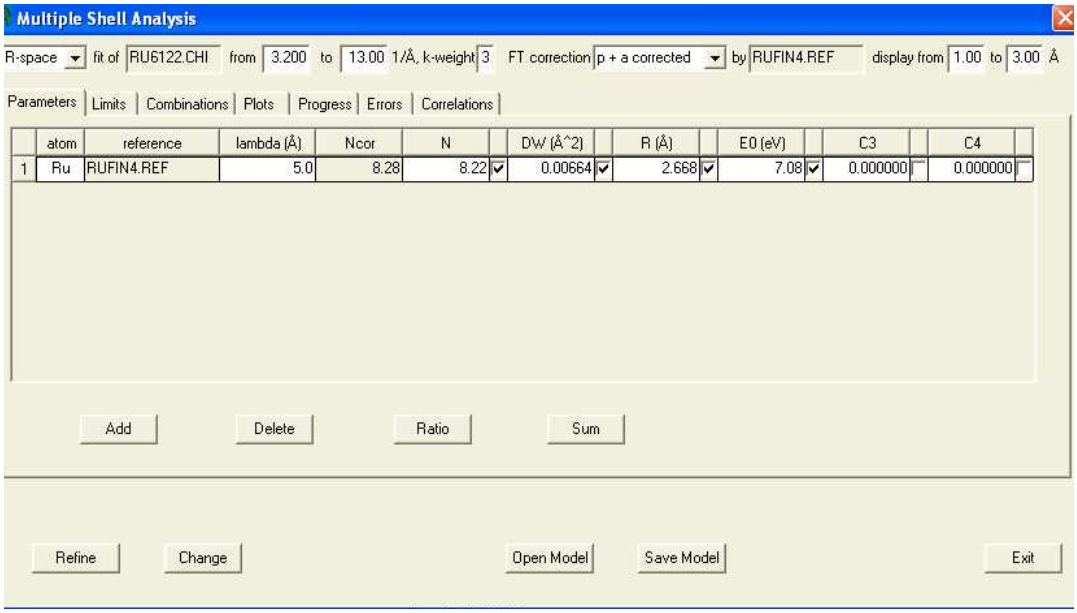

Figure 15: Multiple Shell Analysis window of 'XDAP'

The iterative fitting procedure was performed in a k-range of 3.2-13.0 with a k weighting of 3, due to the metallic character of the catalysts. The spectra were phase corrected. The graphical results of the fitting process and the numerical results of the different catalysts used in this work are shown in Figure 18 and Table 2 (see section 3.1).

3 Results and Discussion

3.1 Catalyst characterization

The Ru/zeolite and the Ru/Al_2O_3 catalysts were characterized by N_2 sorption measurements (surface area), XPS (oxidation state), TEM (Ru particle size), XRD (Ru particle size), H_2 chemisorption (Ru particle size) and XAS (Ru particle size and oxidation state) measurements.

The BET surface area was measured to be 410 $m^2 \cdot g^{-1}$ and 100 $m^2 \cdot g^{-1}$ for the Ru/zeolite support and the Ru/Al_2O_3 catalyst respectively. After Ru loading, the BET surface of the Ru/zeolite catalyst decreased to 300, 311 and 320 $m^2 \cdot g^{-1}$ for the 1.0, 2.2 and 5.6 wt.% Ru/zeolite catalyst. The moderately lower BET surface (by 20%) after Ru loading compared to the BET surface of the pure zeolite is a clear indication that most particles are located inside the zeolite channels and pores, as it was also suggested for other zeolites by Kröger et al. and Korkuna et al. for metal deposition in zeolites [112;113]. Particles agglomerated only on the outer surface, would plug / block the pores which would lead to a more drastic decrease of the BET specific surface area of the loaded catalysts. In addition the Ru/zeolite as well as the Ru/Al_2O_3 catalysts were free of dopants or promoters.

XPS measurements revealed that the Ru nanoparticles of both catalysts (2.2 wt.% Ru/zeolite and 5.0 wt.% $RuAl_2O_3$ catalyst) are mostly oxidic prior to the methanation reaction (Ru^0:Ru^{4+} = 1:4, Figure 16). On the Ru/zeolite catalyst there is some Ti^{4+} present due to the synthesis.

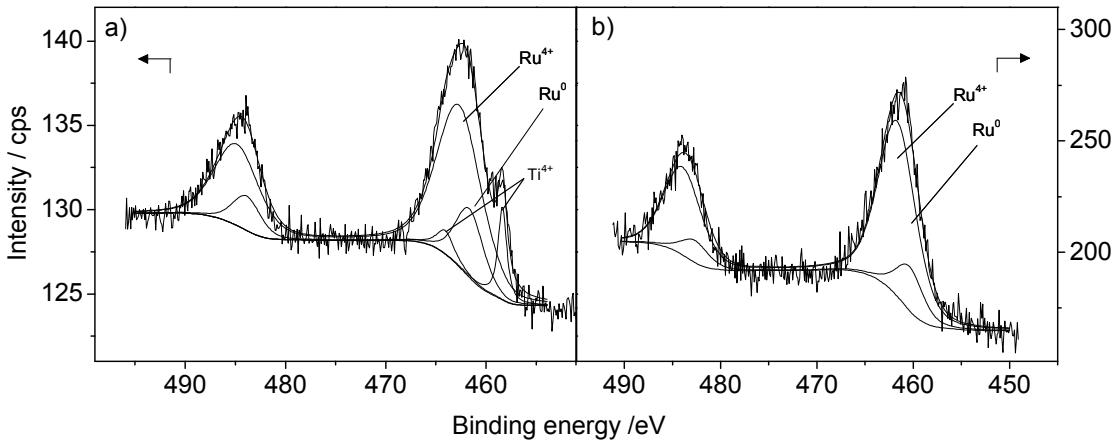

Figure 16: Detail XPS spectra of the Ru(3p) region, a) Ru/zeolite, b) Ru/Al_2O_3

The oxidic Ru prior to reaction was also confirmed by *in situ* XAS measurements prior to reaction (see Figure 42, appendix), where XANES spectra clearly show an intense white line for all Ru catalysts investigated during this work, indicative of oxidic Ru nanoparticles. In addition, it was assumed, that the Ru nanoparticles are located in the very small pores (< 1 nm) of zeolite matrix. This was based on the observation that in previous X-ray photoemission spectroscopy (XPS) measurements the intensity (integrated area) of the Ru(3p) signal on the 2.2 wt.% Ru/zeolite catalyst was only about 5% of that on a non-porous 5 wt.% Ru/Al_2O_3 catalyst, where the Ru NPs are deposited on the surface (Figure 16). In order to assess the metal particle size, the majority of the available publications generally report of the usage of standard techniques to characterize the particle size of the catalysts, such as TEM and / or H_2 adsorption. Most commonly, the H_2 chemisorption method of Dalla Betta [98] was used. During this work it was tried to confirm the small Ru nanoparticles (< 1 nm) present on the Ru/zeolite catalyst by different techniques such as TEM, XRD, H_2 chemisorption and XAS measurements. A detailed knowledge of the particle sizes of the catalytically active component (usually a metal or metal oxide) is important, as size and shape dramatically influence the catalytic behaviour. First, XRD measurements were performed, in order to gain structural information on the Ru NP deposited on the Ru/zeolite catalyst.

Figure 17 depicts the XRD diffractograms of a fresh and used (1000 min ID-ref 6000) Ru/zeolite sample. In addition, the diffractogram of the pure zeolite support is shown. It is clear that the zeolite is crystalline and almost all reflection result from the support. On the fresh Ru/zeolite catalyst (Figure 17 b), a reflection corresponding to metallic Ru is not observed, due to the oxidic Ru particles as discussed above (see Figure 16). A reflection at 41.01° 2θ can be assigned to RuO_2. It is superimposed, however, by a support related signal. For the Ru/zeolite catalyst investigated after reaction, a (very) small and broader Ru^0 signal at support related reflections, (44.8° and 51.4°, Figure 17 a) was observed, indicative of Ru metal nanoparticles or grains. However the signals were not sufficiently well resolved to accurately calculate a particle size. These signals represent larger particles (~10 nm) as they are also observed in TEM investigations (see below), which are exclusively located on the outer surface of the zeolite matrix. The coexistence of smaller particles located in the small pores is not excluded (and cannot be proven by TEM or XRD). This will be discussed with the XAS results. Obviously, the resolution of XRD is too low to identify

the smaller particles (< 1 nm) of the Ru/zeolite catalyst, as the normal detection limit is 2-3 nm, if a good quality spectrum is obtained without additional peaks around the 2θ region of interest. At smaller particle sizes, the FHWM is getting too large, resulting in a small peak caused by the lower number of 'in phase' reflecting planes. Therefore the FHWM of such a signal can hardly be interpreted as it cannot be distinguished from the noise level.

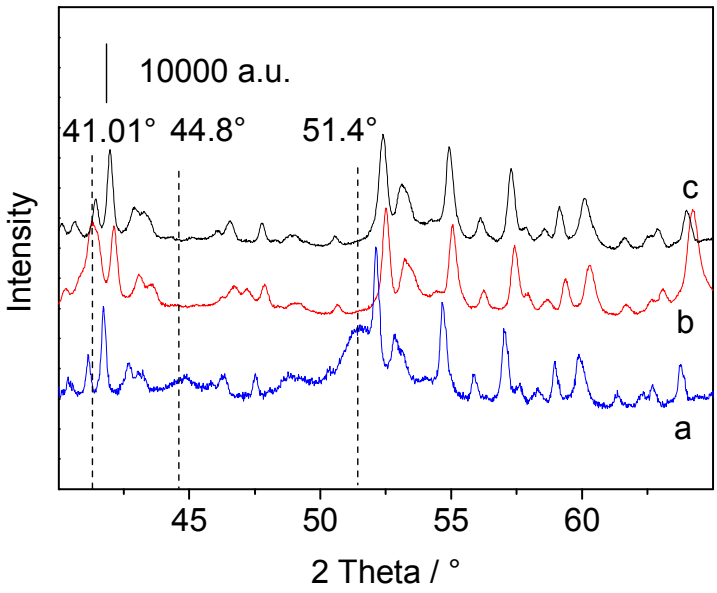

Figure 17: XRD diffractogram of Ru/zeolite catalyst after 1000 min of reaction in ID-ref 6000 (a), fresh Ru/zeolite (b) and the zeolite support (c)

Next, it was tried to evaluate the Ru particle size by TEM imaging. However, high resolution TEM imaging was complicated by electron beam induced decomposition of the zeolite matrice. The images showed a very inhomogeneous distribution of Ru particles, with few individual particles (10-20 nm diameter) and agglomerates of Ru particles, in addition to larger areas without visible nanoparticles (representative TEM images are shown in the appendix). Due to the decomposition of the zeolite it was not possible to statistically analyze the size of Ru particles. Moreover, due the stability problems of the material it was not possible to use the powerful techniques of TEM, e.g. cross section of HAADF to clarify the presence of very small RU NPs inside the porous system. Increasing of the resolution is disadvantageous due to the drastic decomposition of the zeolite matrix upon the irradiation of the sample by the electron beam that is needed for further magnification of the images. Thus, the method can be used only for determination of the larger Ru particles (> ~5 nm in diameter) that will be located exclusively on the surface of the zeolite. The recorded

images (representative TEM images are shown in the appendix (Figure 41), revealed only few individual particles and agglomerates inhomogeneously distributed on the surface. Consequently, most of the surface area is without visible nanoparticles (< 1 nm in diameter). This is in agreement with the previous XRD measurement where small reflections of metallic Ru in the collected diffractograms, typical for the particles around 10 nm, suggested a rather low amount of these crystallites. These findings are explained by the coexistence of the larger particles on the surface and very small Ru nanoparticles, where the latter can be located on both the outer and inner surface of the microporous system. These small particles cannot be detected by the standard methods (TEM and XRD). Further support for the coexistence of large and small Ru NP will be given below (see XAS), where the EXAFS results lead to a mean Ru particle size which is slightly larger (~0.9 nm) than the pores of the zeolite (0.6-0.8 nm).

For the Ru/Al_2O_3 catalyst, the Ru particle size was determined by TEM (statistical analysis) to 2.27 nm diameter (see Figure 41 appendix). This result was expected for the standard Ru/Al_2O_3 catalyst.

Next, H_2 adsorption experiments were conducted on the two catalysts after reduction in H_2 (30 min, 200°C), which yielded active surface areas of 3.7 $m^2\ g^{-1}$ (Ru/Al_2O_3) and 0.095 $m^2\ g^{-1}$ (Ru/zeolite). This would correspond to dispersions / Ru particles sizes of 15%/4.2 nm and <1%/113 nm, respectively. (It should be noted that higher reduction temperatures up to 300°C had no effect on the active surface area, above that temperature, the active surface area decreases, probably due to agglomeration.)

Obviously, the dispersions and particle sizes derived from the adsorption experiments are incompatible with those determined by TEM or XRD in the case of the Ru/Al_2O_3 catalyst. This discrepancy can be explained by assuming that the surface area H_2 adsorption does not necessarily correspond to the whole particle. For the Ru/zeolite catalyst the dispersion calculated by H_2 chemisorption seems to be far too low. Obviously this method is not applicable for this (acidic) zeolite supported catalyst due to suppression of H_2 chemisorption, as it was already reported for acidic zeolites by Wang et al. [114] and McCarthy et al. [115]. They explained this observation to the interaction of the Ru clusters with the protons of the zeolite.

The *in situ* XAS measurements were conducted in idealized reformate gas (ID-ref 6000), until the coordination number did not change any more, at least over 500 min.

By determining the average coordination number of the Ru atoms in the Ru nanoparticles during reaction, the average particle sizes of all catalysts were calculated. The results are shown in Figure 18 and Table 2. The k^3 weighted chi functions obtained on the 2.2, 3.6 and 5.6 wt.% Ru/zeolite and the 5.0 wt.% Ru/Al_2O_3 catalysts are plotted in the k-range from 3.2-13.0 $Å^{-1}$ in the left panels in Figure 18. Measurements on the 1 wt.% Ru/zeolite catalyst could not be evaluated, as the catalyst loading was too low to obtain a good quality spectrum. The right panels show the resulting Fourier transforms in r-space in the range of the first shell (Ru-Ru scattering, r-range:1.0-3.0). It is clear that with higher loading and larger particles, respectively, the signal intensities in both k and r-space increase. The prominent signal (Ru-Ru scattering) at ~2.7 Å in r-space indicates that the particles are essentially metallic under steady-state conditions. It should be noted that the spectra could be fitted with only a single Ru-Ru shell. The result of metallic Ru NPs is compatible with findings of *in situ* DRIFTS measurements, which yielded vibrational frequencies for adsorbed CO similar to those characteristic for CO_{ad} on metallic Ru (see below) [116].

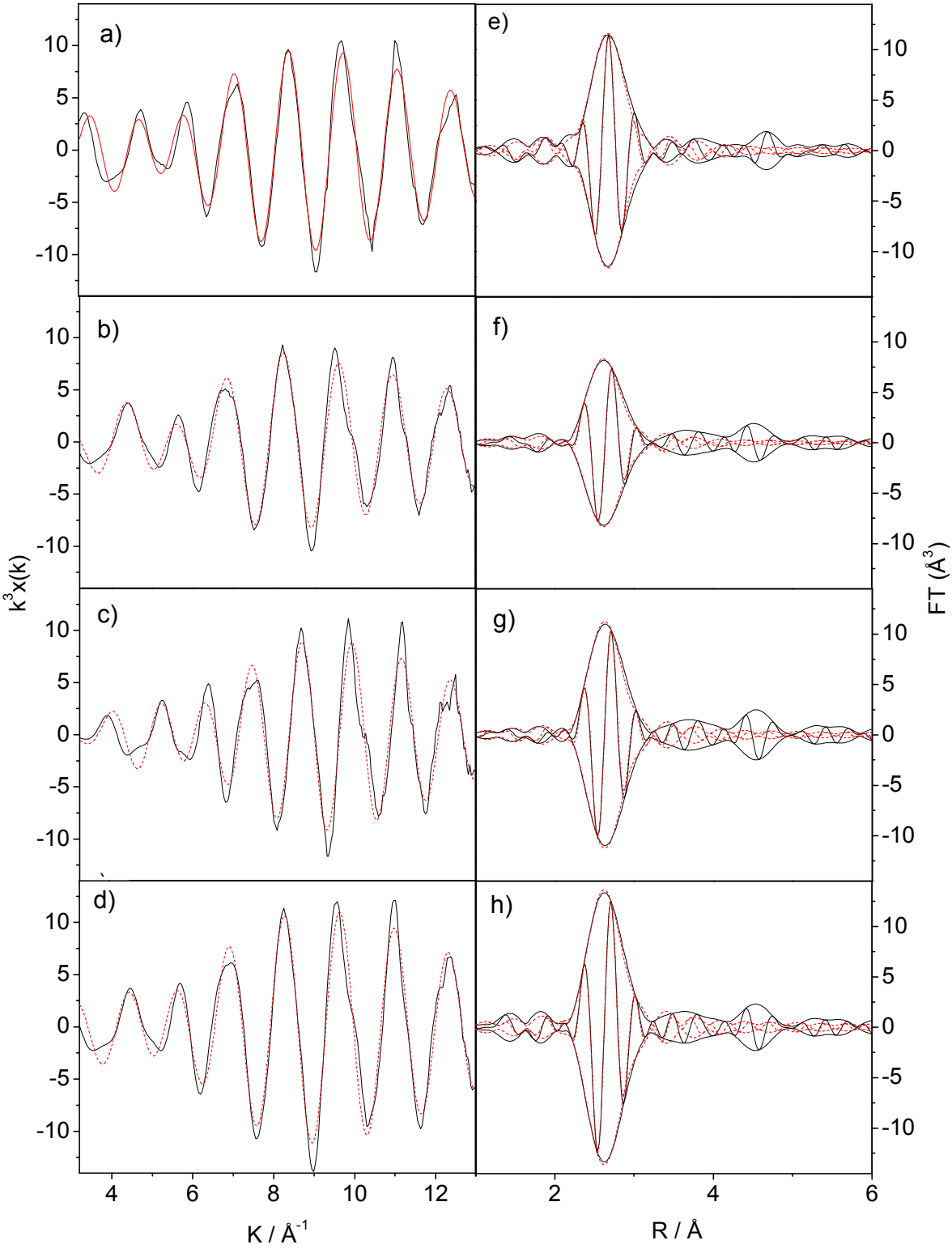

Figure 18: Left: k^3 weighted chi function, right: corresponding Fourier transform (k^3-weighted, 3.2 < k < 13.0 A^{-1}) of (a), (e): Ru/Al_2O_3, (b), (f) 2.2 wt.% Ru/zeolite, (c), (g) 3.6 wt.% Ru/zeolite, (d), (h) 5.6 wt.% Ru/zeolite

It should be noted that EXAFS spectra recorded prior to the experiment confirmed that in this state the Ru NPs of all catalysts are oxidic, as indicated by the XANES spectra (Figure 42, appendix). They are reduced within 2 min after exposure to the reaction atmosphere, which from experimental reasons was not accessible to time-resolved measurements. The Ru-Ru coordination number, which was obtained by fitting the first shell (Ru-Ru at ~2.7 A) to the Ru foil reference (see Fig. 1), can be directly correlated to the mean particle size of the Ru NPs by using a relation determined by Karim et al. [117]. Table 2 summarizes the structural parameters resulting from the fitting procedure. The 'goodness of the fit' (see eq. 2.41) was always between 1 and 2, indicative of a good fit.

Catalyst **Ru/zeolite**	Coordination number	Debye Waller factor /10^{-3} Å^2	Distance / Å	E_0/eV	Mean Ru particle size / nm	Disp. / %
2.2 wt.%	6.71 ± 0.21	6.62 ± 0.41	2.711 ± 0.007	6.12 ± 0.22	0.9	82
3.6 wt.%	8.31 ± 0.24	7.71 ± 0.42	2.673 ± 0.007	7.11 ± 0.21	1.6	45
5.6 wt.%	8.60 ± 0.23	6.83 ± 0.36	2.671 ± 0.003	8.02 ± 0.16	1.9	40
Ru/Al_2O_3 5.0 wt.%	9.21 ± 0.44	2.47 ± 0.91	2.667 ± 0.007	6.0 ± 0.39	2.3	31

Table 2: Results of the EXAFS fit procedure and resulting structural parameters of the different Ru/zeolites catalysts measured under steady-state conditions in idealized reformate (0.6 % CO, balance H_2).

In addition, the coordination numbers did not change significantly when applying different k weightings, underlining the good quality of the fits. The spectra taken at reaction temperature (190°C) show a slightly smaller Ru-Ru bond length of ~2.67 Å compared to 2.70 Å in bulk Ru for all catalysts investigated, indicative of a contraction of the Ru lattice in the very small Ru NPs. In contrast to the constant Ru-Ru bond length, the Ru coordination number increases with increasing catalyst loading, from 6.7 to 8.6 (Table 2), reflecting an increasing Ru particle size in the Ru/zeolite catalysts. This corresponds to particle sizes of 0.9 nm (2.2 wt.%), 1.6 nm (3.6 wt.%) and 1.9 nm (5.6 wt.%). Moreover, the Debye Waller factors change with the Ru particle size. This is due to the different surface to volume atoms ratio on the

Ru catalysts, where surface atoms experience a different ‘neighborhood’ than volume atoms and in consequence have a larger Debye Waller factor. The very small Ru particle size obtained from EXAFS for the 2.2 wt.% Ru/zeolite catalyst supports the proposal above, according to which most of the Ru NPs of the 2.2 wt.% Ru/zeolite catalyst are located inside the pores of the zeolite (0.6-0.8 nm diameter). It can not be ruled out that in addition to the very small Ru NPs proposed to be located in the pores (0.6-0.8 nm) of the zeolite also a few larger Ru NPs are present on the outer surface. Their number, however, must be rather small on the 2.2 wt.% catalyst. For the catalysts with higher Ru loading, the 3.6 and 5.6 wt.% Ru/zeolite catalysts, it is tentatively suggested that the larger mean particle sizes obtained from the EXAFS measurements (1.6 and 1.9 nm, respectively) result from a higher fraction of larger particles, in addition to the very small Ru NPs in the pores of the zeolite. In semi-realistic reformate (SR-ref 6000), containing 15.5% CO_2 in addition to 6000 ppm CO, similar Ru particle sizes as determined in idealized reformate were expected, since CO_{ad} will block the surface and hence the active sites for CO_2 dissociation and methanation. Therefore, the presence of CO_2 is not expected to measurably affect the Ru particle size. The particle size derived by the EXAFS measurements of the Ru/Al_2O_3 catalyst (2.3 nm) is in good accordance with the TEM results, which proves the compatibility of both methods. However, a deviation is observed when comparing these results to the results of the H_2 chemisorption (2.3 nm vs. 4.2 nm). The result of the H_2 chemisorption corresponds most likely to the catalytically active surface, most probably due to the partially blocking of active surface area by carbonaceous deposits, resulting in a smaller surface for H_2 chemisorption, which in fact is not measured by the EXAFS experiments.

For calculating TOFs during this work it is most appropriate to take the particle sizes derived by XAS measurements for all catalysts investigated. Only in section 3.3 where the intermediate of the CO and CO_2 methanation is investigated on the Ru Al_2O_3 catalyst, the active surface derived by H_2 chemisorption is used, since this is directly correlated to the methanation reaction mechanism.

3.2 Activity, selectivity, and adsorbed reaction intermediates/reaction side products in the selective methanation of CO in reformate gases on supported Ru catalysts

This section provides a general insight of the characteristics and performance of the catalysts under different reactive feed gases. At first the catalytic behaviour of both catalysts is determined by 'temperature screening' experiments, where the activity of the two Ru catalysts for the conversion of CO and CO_2 to CH_4 and the influence of CH_4, H_2O and CO_2 on the CO methanation reaction in different gas mixtures under integral reaction conditions (see Table 3 and Table 4) were explored. Next, the activities of both catalysts are determined under differential reaction conditions in various reaction gas atmospheres. Additional kinetic information is obtained by measuring the apparent activation energy and the reaction order for H_2 and CO. Finally, the time resolved production of surface products is investigated in *in situ* DRIFTS measurements, which were performed under identical reaction conditions as in the kinetic measurements. A transient 'shut off' experiment, where a CO/H_2 atmosphere is replaced by a N_2/H_2 atmosphere, provides evidence on reaction intermediates and side products. Some of the presented data were obtained during my diploma thesis, which are marked accordingly.

The following sections were published in the Journal of Catalysis 269 (2010) 255: S. Eckle, Y. Denkwitz, R.J. Behm, *Activity, selectivity, and adsorbed reaction intermediates/reaction side products in the selective methanation of CO in reformate gases on supported Ru catalysts*.

3.2.1 Temperature screening experiments

Figure 19 shows the temperature dependent conversions of CO and CO_2 on the Ru/Al_2O_3 (left panels) and Ru/zeolite catalysts (right panels, data taken from *[118]*). The upper and lower panels depict the conversion during the methanation reaction in CO_2-free and CO_2-rich gas mixtures, respectively. In the different gas mixtures, the CO conversion on both catalysts results in a typical S-shaped curve, starting at 150°C with a very low conversion (< 5%).

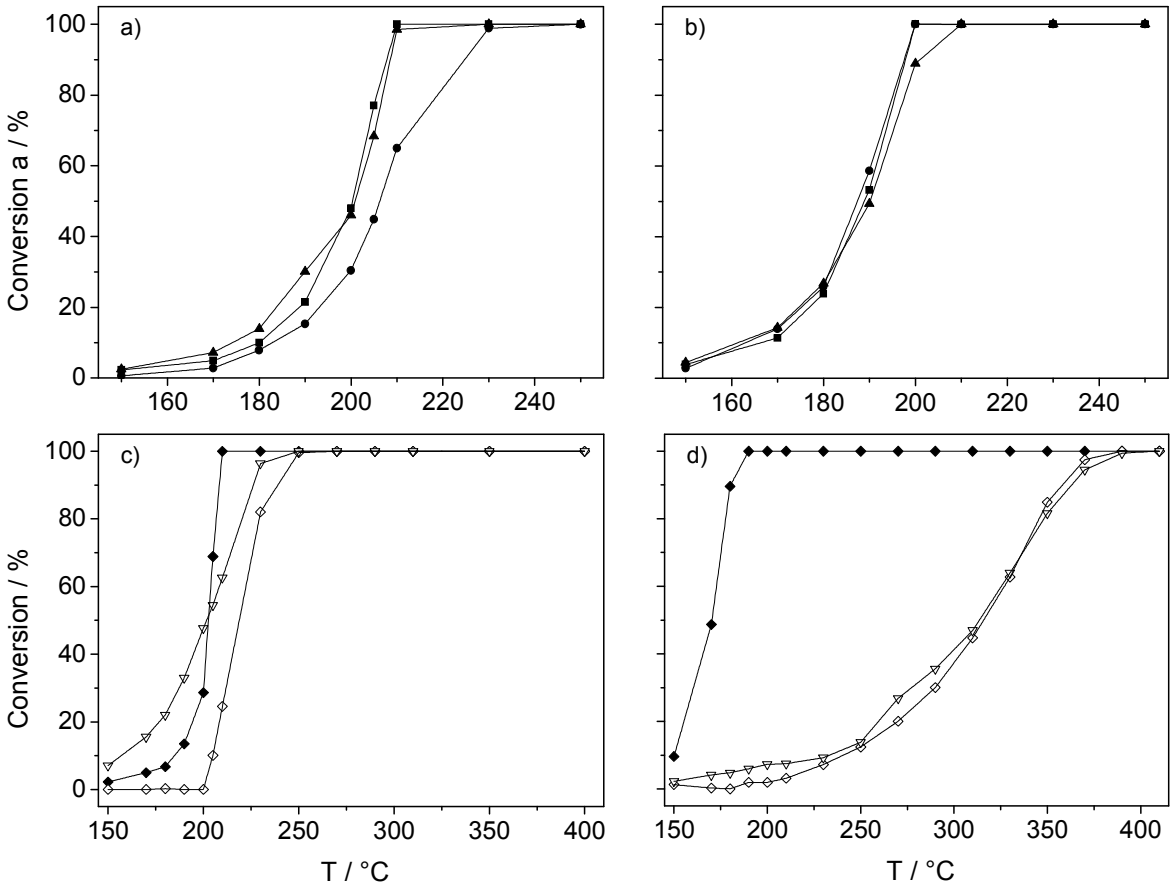

Figure 19: Temperature dependence (150-400°C) of the CO conversion (filled symbols) and CO_2 conversion (open symbols) on a Ru/Al_2O_3 (a, c) and a Ru/zeolite (b, d, taken from [118]) catalyst (210 mg; GHSV: 5000·h^{-1}) in different reformate gases: (■) ID-ref 6000, (▲) H_2O-rich ID-ref 6000, (●) CH_4-rich ID-ref 6000; (◆, ◇) CO_2-rich ID-ref 6000 and ▽: CO_2-ref.

For reaction in a CO/H_2 mixture (ID-ref 6000, 0.6 % CO, 2.6 % N_2, rest H_2), 50% CO conversion to CH_4 (T_{50}) are reached at 200 and 190°C for the Ru/Al_2O_3 and Ru/zeolite catalysts, respectively, under present reaction conditions (Figure 19, top panels).

Reaction gas	Reaction gas-composition	T_{50} = 50% conversion (CO)	T_{100} = 100% conversion (CO)	T_{50} = 50% conversion (CO_2)	T_{100} = 100% conversion (CO_2)
Idealized reformate	0.6 % CO, 2.8 % N_2, balance H_2	200°C	210°C	-	-
CH_4-rich idealized reformate	0.6 % CO, 2.8 % N_2, 4.5 % CH_4, balance H_2	200°C	230°C	-	-
H_2O-rich idealized reformate	0.6 % CO, 2.8 % N_2, 5 % H_2O, balance H_2	205°C	230°C	-	-
CO_2- rich idealized reformate	0.6 % CO, 2.8 % N_2, 1.2 % CO_2, balance H_2	205°C	230°C	225°C	270°C
CO-free idealized reformate	1.2 % CO_2, 2.8 % N_2, balance H_2	-	-	205°C	250°C

Table 3: Reaction temperature for 50 and 100% CO/CO_2 conversion in the methanation reaction on 210 mg Ru/Al_2O_3 catalyst (5 wt.% Ru, GSVH: 5000 h^{-1})

Reaction gas	Reaction gas composition	T_{50} = 50% conversion (CO)	T_{100} = 100% conversion (CO)	T_{50} = 50% conversion (CO_2)	T_{100} = 100% conversion (CO_2)
Idealized reformate	0.6 % CO, 2.8 % N_2, balance H_2	190°C	200°C	-	-
CH_4-rich idealized reformate	0.6 % CO, 2.8 % N_2, 4.5 % CH_4, balance H_2	190°C	210°C	-	-
H_2O-rich idealized reformate	0.6 % CO, 2.8 % N_2, 5 % H_2O, balance H_2	190°C	210°C	-	-
CO_2- rich idealized reformate	0.6 % CO, 2.8 % N_2, 1.2 % CO_2, balance H_2	170°C	190°C	330°C	410°C
CO-free idealized reformate	1.2 % CO_2, 2.8 % N_2, balance H_2	-	-	330°C	410°C

.

Table 4: Reaction temperature for 50 and 100% CO/CO_2 conversion in the methanation reaction on 210 mg Ru/zeolite catalyst (2.2 wt.% Ru, GSVH: 5000 h^{-1}). Data taken from [118]

After reaching full conversion, a further increase of the temperature did not exert any effect on the CH_4 production on either catalyst. Full CO conversion is reached at 10°C lower temperature on the Ru/zeolite catalyst (200°C) than on the Ru/Al_2O_3 catalyst (210°C) (see Table 3 and Table). Since the Ru loading of the Ru/zeolite catalyst (2.2 wt.%) is less than half of that of the Ru/Al_2O_3 catalyst (5 wt.%), its Ru mass normalized activity is higher than that of the latter catalyst. Similar trends are observed when adding H_2O (H_2O-rich ID-ref 6000) or CH_4 (CH_4-rich ID-ref 6000) to the gas-mixture, with the differences in activity becoming slightly larger (Figure 19, top panels; Table 3 and Table 4). For both the H_2O-rich and the CH_4-rich reformate, the temperature dependence does not change for the Ru/zeolite catalyst. The Ru/Al_2O_3 catalyst behaves similarly in the CH_4-rich reformate, while in H_2O-rich reformate the T_{50} temperature is shifted to slightly higher values, from 200 to 205°C.

Next, the CO_2 methanation reaction in low CO_2-ref (CO-free) reaction gas mixture (H_2/CO_2 mixture) was investigated. The general shape of the temperature dependent CO_2 methanation curve is comparable to that for CO methanation in ID-ref 6000 (0.6 % CO; 2.6 % N_2; rest H_2) for the Ru/Al_2O_3 catalyst, except for a slight shift to higher temperatures (CO_2 conversion: T_{50} = 205°C, CO conversion: T_{50} = 200°C, see). In contrast, on the Ru/zeolite catalyst the increase of the CO_2 conversion with increasing temperature is significantly slower. The temperature for 50% conversion (T_{50}) is shifted to 330°C (CO methanation: T_{50} = 190°C, see Table 4), and full conversion is reached only at 410°C (CO methanation: 200°C, see Table 4).

Adding CO to the gas-mixture (CO_2-rich ID-ref 6000: 0.6 % CO, 2.8 % N_2, 1.2 % CO_2, rest H_2), the general shape of the conversion curve for CO and CO_2 methanation does not change, neither for the Ru/zeolite nor for the Ru/Al_2O_3 catalyst (Figure 19, bottom panels; (Table 3and Table 4). For the Ru/Al_2O_3 catalyst, however, the CO_2 conversion curve is shifted to higher temperatures, and seems to be suppressed by the presence of CO, at least over a temperature range of 20°C. The temperature for 50% CO_2 conversion is shifted from 205°C in a H_2/CO_2 mixture to 225°C in the presence of CO, in CO_2-rich ID-ref 6000. Nevertheless, CO_2 conversion starts already well before all CO is converted to CH_4. At 100% CO conversion (230°C), the selectivity is 48%. On the other hand, for the Ru/zeolite catalyst, the CO_2 methanation reaction is only little affected by the presence of CO. Furthermore, the CO methanation is accelerated by the presence of CO_2, and 50% CO conversion was reached at 170°C in CO_2-rich

idealized reformate rather than at 190°C in idealized reformate. In the presence of CO_2, the reaction is 100% selective for CO methanation on the Ru/zeolite catalyst up to 190°C. Only at 230°C, the CO_2 conversion reaches 10%, i.e., there is a temperature window of 40°C where the selectivity for CO methanation is >85%.

Comparison of the temperature screenings results with previously reported data is hardly possible, at least not on a quantitative scale, because of the different reaction conditions, reaction mixtures and procedures for catalyst pre-treatment. For the Ru/zeolite catalyst, there are no previous studies on the CO methanation reaction at all. For CO methanation in idealized reformate on a Ru/Al_2O_3 catalyst, Randhava et al. [23] reported a T_{50} value (200°C) which is similar to the result obtained in this work. It was measured, however, on a lower loaded 0.5 wt.% Ru/Al_2O_3 catalyst in 0.3% CO (rest H_2) at a significantly higher space velocity (GHSV: 36000 h^{-1}, measurement presented here: GSHV: 5000 h^{-1}). They observed that the T_{50} value shifts to higher temperature with higher GHSV and attributed this to the lower contact time (CO conversion of 50% at 230°C for a GHSV of 36000 h^{-1}). Echigo and Tabata [17] performed temperature screening experiments on a 1 wt.% Ru/Al_2O_3 catalyst at a lower GHSV (7500 h^{-1}) in H_2O-rich reformate (0.54% CO, 20% H_2O, rest H_2) and in realistic reformate (0.54% CO, 21% CO_2, 20% H_2O, rest H_2). In the first gas mixture, they measured a T_{50} temperature of 190°C, and full conversion (<10 ppm) was reached at 210°C. Adding CO_2 to the gas mixture, the CO conversion at 190°C dropped to about 45%, and full conversion was not reached up to 230°C (maximum conversion 96% at 230°C). Comparable to the observations for the Ru/Al_2O_3 catalyst in this work, not all CO is converted, although the methane production exceeds the CO consumption. The CO_2 conversion starts already at 205°C; at 230°C the selectivity was 40%. Adding CH_4 to the gas-mixture did not change the performance of their catalyst. Dagle et al. [40] also investigated the methanation reaction in realistic reformate (0,9% CO, 24,5% CO_2, 5,7% H_2O, rest H_2) on differently loaded Ru/Al_2O_3 catalysts (3 wt.%, 5 wt.% and 7 wt.%, GHSV 13500 h^{-1}). They observed the same T_{50} value (T_{50} = 205°C) on their 5 wt.% Ru/Al_2O_3 catalyst as determined on the 5 wt.% Ru/Al_2O_3 catalyst, but at significantly higher CO, CO_2 and H_2O contents and at a higher space velocity. At higher temperatures, however, their catalyst became active for the reverse water gas shift (RWGS) reaction, which was evidenced by the onset of CO production at higher temperatures. Such effects were not observed in the present work, neither for the Ru/zeolite nor for the Ru/Al_2O_3 catalyst. The temperature for 99

% conversion (100 ppm CO in the gas mixture) was lowest for the 5 wt.% catalyst, and increased in the order 5 wt.% < 3 wt.% << 7 wt.%.

In total, the activity, measured in terms of conversion curves and T_{50} values, and the selectivity of the Ru/Al_2O_3 catalyst in this work are comparable to those reported in previous studies [17;23;40]. The Ru/zeolite catalyst shows a comparable activity, despite of the much lower Ru content, and a significantly higher selectivity for the CO methanation in the presence of CO_2 over a wide temperature range.

3.2.2 Kinetic measurements

For more detailed information on the time dependent activity and the stability of the catalysts under reaction conditions, the reaction rates were evaluated under differential reaction conditions (conversion < 15%) as a function of increasing time on stream, up to over 1000 min reaction time. This time was chosen since initial measurements showed only very slow changes in the reaction behavior after 800 min on stream. The activity is given in Ru mass normalized rates in Figure 20. In addition, these data were used to calculate turn-over frequencies (TOFs) using the Ru surface areas determined by the *in situ* XAS experiments (see section 3.1), which are listed in Table 2 where 190°C were used as reaction temperature. At this temperature, both Ru catalysts showed 100% selectivity in CO_2-rich ID-ref 6000 reformates in the temperature screening measurements and both catalysts exhibited a high CO activity (Figure 19). The conversion was reduced by using smaller amounts of catalyst (see section 2.1.1).

Figure 20 illustrates the reactivity-time curves resulting for the two catalysts at 190°C in different reaction atmospheres. In order to approach more realistic situations, two gas mixtures with higher CO_2 contents (semirealistic conditions) were included, namely SR-ref 6000 (0.6 % CO, 2.8 % N_2, 15.5 % CO_2, balance H_2) and H_2O-rich SR-ref 6000 reformate (0.6 % CO, 2.8 % N_2, 15.5 % CO_2, 5 % H_2O, balance H_2), in addition to the ID-ref 6000 and the CH_4-rich ID-ref 6000 used also in the temperature screening experiments.

For reaction in ID-ref 6000 (0.6 % CO, 2.8 % N_2, balance H_2; Figure 20a), the catalysts exhibit initial reaction rates of 65×10^{-6} and 3.4×10^{-6} $mol\cdot s^{-1}\cdot g_{Ru}^{-1}$ for the Ru/zeolite (data taken from [118]) and the Ru/Al_2O_3 catalyst, respectively. At the beginning of the reaction, over ~50 min, the Ru/zeolite catalyst shows a slight increase in activity and then decays slowly, reaching ~80% of its maximum intensity

after 1000 min. In contrast, on the Ru/Al_2O_3 the reaction is about stable over the entire time on stream of 1000 min.

The steady-state reaction rates for the Ru/zeolite and the Ru/Al_2O_3 catalyst are $63.9\pm1.5\times10^{-6}$ $mol\cdot s^{-1}\cdot g_{Ru}^{-1}$ and $3.4\pm0.3\times10^{-6}$ $mol\cdot s^{-1}\cdot g_{Ru}^{-1}$ respectively, equivalent to TOFs of 7.9 s^{-1} and 1.1 s^{-1}. It should be noted that the TOFs were calculated by the average particle size derived by the XAS measurements. Therefore deviations caused by missing very small Ru nanoparticles or clusters, e.g. in TEM images, do not affect these results. Changing to CH_4-rich ID-ref 6000 or SR-ref 6000 does not influence the activity and its characteristic development during 1000 min reaction for either of the two catalysts. In the SR-ref 6000 gas mixture (Figure 20, b), both catalysts are 100% selective, which was associated with the high remaining CO partial pressure (about 10% CO conversion) and the low reaction temperature (CO_{ad} blocking of the catalyst surface). In all cases, the Ru/zeolite catalyst shows a significantly higher activity than the Ru/Al_2O_3 catalyst. It exceeds that of the latter catalyst by at least a factor of about 10 for the Ru mass normalized reaction rate. The small differences between the rates measured for different gas compositions are within the precision of the measurements. A significantly lower activity (~50%) is obtained, however, in H_2O-rich SR-ref 6000, on the Ru/zeolite catalyst. The other characteristics, the low deactivation with time by about 20% over 1000 min and 100% selectivity remain unchanged. On the Ru/Al_2O_3 catalyst, the addition of water to SR-ref 6000 has essentially no consequences on the reaction behavior.

Comparing the Ru mass normalized rates for the methanation reaction with results reported previously for reaction on supported Ru catalysts (see Table 10, appendix) [41;42;61;119-121], the Ru/zeolite catalyst exhibits a high activity at lower reaction temperature (190°C) even in SR-ref 6000. Only the Ru/Al_2O_3 catalyst studied by Kowalczyk et al. [41] shows a higher reaction rate, yet their measurement was performed at a higher temperature. The Ru/Al_2O_3 catalyst exhibits a lower activity compared to the rates reported for other Ru/Al_2O_3 catalysts (Table 10, appendix). However, one has to take into account that the reaction temperature and the gas compositions used in the previous studies differ considerably. Panagiotopoulou et al. [42] measured the CO methanation rate on a 0.5 wt.% Ru/Al_2O_3 catalyst at 250°C in idealized reformate as well as in more realistic gas mixtures (see Table 10, appendix), and obtained higher reaction rates than determined in this work.

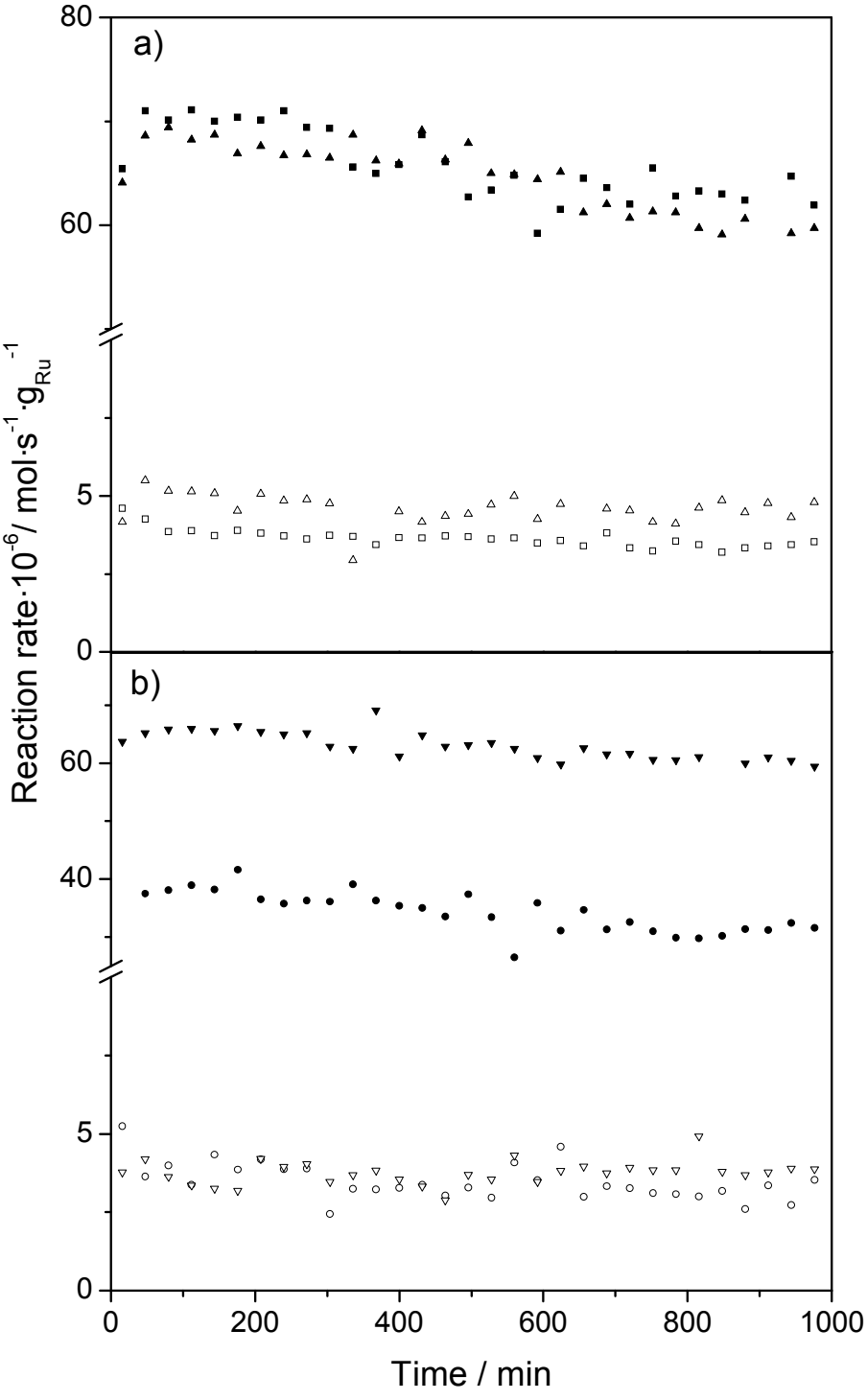

Figure 20: Reaction rates on the Ru/zeolite (filled symbols, diluted 1:10 with SiO_2) and the Ru/Al_2O_3 (open symbols, diluted 1:3 with Al_2O_3) catalyst in different reformate gases: a) (■, □) ID-ref 6000; a) (▲, △) CH_4-rich ID-ref 6000; b) (▼, ▽) SR-ref 6000; b) (●, ○) H_2O-rich SR-ref 6000 (see Table 1 for abbreviations)

The higher reaction temperature in their measurements has a positive effect on the activity, but they also used a gas mixture with higher CO and lower H_2 concentration, which has a negative influence on the activity [26]. Additionally, they used a different Ru loading, which may also affect the activity [40].

Using turn-over frequencies as a measure of the intrinsic activity of the Ru particle surface rather than the Ru mass normalized rates for comparison (see Table 10, appendix), the very high activity of the Ru/zeolite catalyst is even more obvious, showing a smaller but comparable TOF value, despite the lower reaction temperature in the present study (Table 10). The general trends of the mass normalized activities, however, are reproduced. It is important to realize that the turnover frequencies reported in the different studies are based on different methods for determining the active Ru particle surface. Kowalczyk et al. [41] used O_2 chemisorption at 0°C after reduction at 430°C or 520°C for 20h. Subsequently, the catalyst was reduced at the same temperatures again and CO chemisorption was performed at room temperature (stoichiometries: 1.1 O atoms per Ru surface atom, 0.6 CO molecules per Ru surface atom). Panagiotopoulou et al [42] performed H_2 chemisorption at 100°C to calculate the Ru dispersion. All other groups [119;121;122] used reversible/irreversible H_2 chemisorption at room temperature to determine the Ru surface area and thus the Ru particle size.

Comparing two 3 wt.% Ru/Al_2O_3 catalysts with 10 nm and 34 nm Ru particles, Dagle et al. [40] found 99% CO conversion at a 20°C lower temperature on the former catalyst (10 nm) than on the other one. These authors concluded that catalysts with higher dispersion exhibit a higher activity for the CO methanation, while the lower dispersed catalyst tends to suppress the CO_2 conversion better. A similar particle size dependence of the activity was observed also by other groups [123;124], whereas other studies reported a decreasing activity with increasing Ru dispersion [25;41;125]. Gupta et al. [31;32] concluded from combined DRIFTS and kinetic measurements, that the influence of the Ru dispersion on the methanation activity depends on the reaction temperature and suggested that different mechanisms are dominant below and above 220°C. Only at temperatures below 220°C, a dispersion dependent mechanism prevails.

The much higher activity of the Ru/Zeolite compared to the Ru/Al_2O_3 catalyst observed in this study, both in terms of Ru mass normalized rates and in turnover frequencies, is attributed to several reasons. Most directly, support effects arising from

the different morphology (porous structure) and the different chemical properties of the zeolite surface (higher acidity) may contribute to the higher activity of the Ru/zeolite catalyst. In addition to changes in the surface chemistry, these effects may also modify the diffusion properties and thus the effective contact time [126]. Support effects were reported also in earlier studies [79;119]. Sciré et al. suggested that zeolites (in their work: ZSM-5) stabilize Ru in an oxidized, cationic form [79], while this is not or to a lesser extent possible for Al_2O_3 or SiO_2. The positive polarization of the Ru species was suggested to weaken the Ru-CO bond, via the resulting higher H_{ad} steady-state coverage, and thus to enhance the activity for the methanation reaction. Furthermore, the presence of very small Ru particles in the Ru/zeolite catalyst (< 1 nm Ru particles) compared to the Ru/Al_2O_3 catalyst (~2.3 nm Ru particles) may also affect the activity of this catalyst via particle size effects. However, different groups stated smaller particles to be less active than larger particles [25;44;45;127] this will be discussed in detail in section 3.5). The higher activity of the Ru/zeolite in contrast to the Ru/Al_2O_3 catalyst is therefore deduced to metal support interactions. From measurements in ID-ref 6000, SR-ref 6000 and H_2O-rich SR-ref 6000, the apparent activation energies of the CO methanation reaction on the Ru/Al_2O_3 and the Ru/zeolite catalysts was determined. The data regarding to the Ru/zeolite catalyst in ID-ref 6000 are taken from [118] The measurements were performed in the temperature range between 165°C and 190°C, after initial equilibration during 1000 min reaction at 190°C (see Figure 21a). To avoid irreversible changes of the catalyst, the reaction temperature was limited to 190°C at maximum. The apparent activation energies obtained for the two catalysts are listed in Table 11 (appendix). The measurements were performed first from high to low temperatures and then back to high temperatures again. For similar reaction conditions, the apparent activation energies are slightly lower on the Ru/zeolite catalyst than on the Ru/Al_2O_3 catalyst. In idealized reformate, the apparent activation energies are 90±11 and 111±10 kJ mol^{-1} for the Ru/zeolite and the Ru/Al_2O_3 catalyst, respectively. The values do not change significantly for reaction in SR-ref 6000 and H_2O-rich SR-ref 6000 despite of the lower activity of the Ru/zeolite catalyst in the latter reaction atmosphere. The close similarity of the activation barriers points to a similar rate limiting step for both catalysts and in different reaction mixtures.

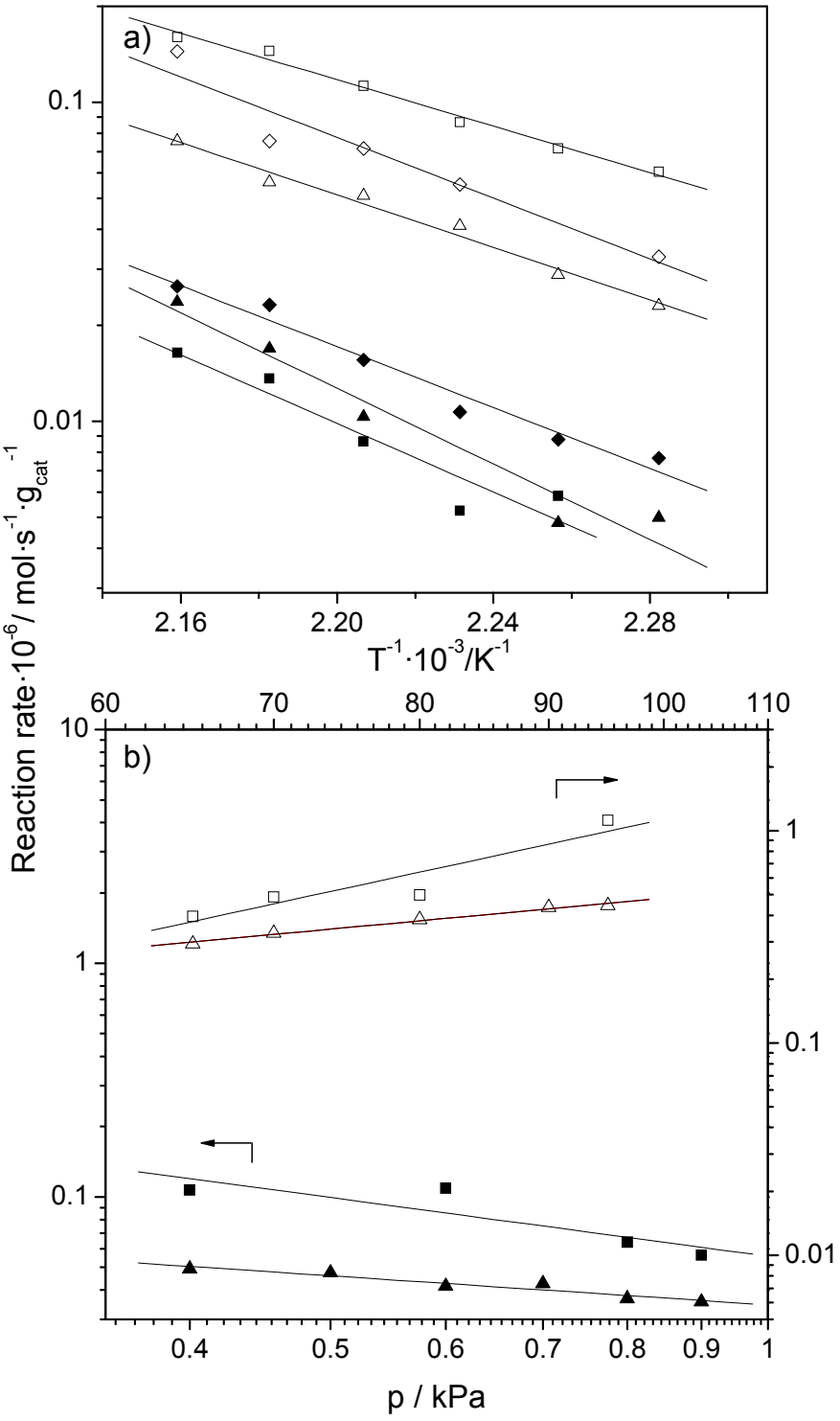

Figure 21: a) Arrhenius plot of temperature dependent reaction rates after 1000 min methanation reaction on the Ru/Al_2O_3 (filled symbols) and the Ru/zeolite (open symbols) catalysts in different reformate gases: (▲,△) ID-ref 6000; (■,□) SR-ref 6000; (◆,◇) H_2O-rich SR-ref 6000. b) Logarithmic plot of the partial pressure dependent reaction rates after 1000 min methanation reaction on the Ru/Al_2O_3 (▲,△) and the Ru/zeolite (■,□) catalysts in ID-ref 6000 (see Table 1 for abbreviations): H_2 reaction order (□, △), CO reaction order (■,▲).

Comparable values for the activation energy were reported by Dalla Betta et al. [128] and Ekerdt and Bell [27] for reaction in a CO/H_2 mixture on Ru/Al_2O_3 and Ru/SiO_2 catalysts, respectively (Table 11, appendix). In contrast, other groups reported higher values between 121 and 156 $kJ \cdot mol^{-1}$ for reaction in CO/H_2 mixtures on differently loaded Ru/Al_2O_3 catalysts (Table 11, appendix) [23;42;129;130]. The spread in apparent activation energies is most likely due to the different reaction conditions in the different studies (see Table 1 supporting information). Finally, Panagiotopoulou et al. [42] reported that adding 15 % CO_2 to a CO/H_2 mixture lowers the activation energy on a 0.5 wt.% Ru/Al_2O_3 catalyst from 121 $kJ \cdot mol^{-1}$ to 77 $kJ \cdot mol^{-1}$. This result contrasts the observation of a negligible variation in the activation energy upon variation of the reaction atmosphere in this work. However, they measured the activation energy at higher temperatures (200°C to 300°C). The differences in the apparent activation energies in the presence of CO_2 in the reformate may indicate a change of the rate limiting step above 190°C.

The influence of the reactant concentration on the methanation reaction in ID-ref 6000 was investigated by determining the reaction orders for CO and H_2 on both catalysts (Figure 21 b). This was done by stepwise varying the CO (H_2) partial pressure from 0.9 to 0.4 % (from 96.4 to 65 %), while keeping that of the second reactant constant (H_2: 96.4 %, CO: 0.6 %), and going back again to the initial partial pressure. Since the data agree closely, only the downwards runs are shown. The resulting CO reaction orders of -0.7±0.1 and -0.5±0.1 are of similar order of magnitude for the Ru/zeolite (taken from [118]) and the Ru/Al_2O_3 catalyst, respectively. For H_2, the Ru/zeolite catalyst (reaction order: 2.7±0.2, taken from [118]) shows a much more pronounced dependence of the activity on the H_2 concentration than the Ru/Al_2O_3 catalyst (reaction order: 1.0±0.1). For comparison, Ekerdt and Bell. [27] reported reaction orders of -0.6 and 1.5 for CO and H_2 on a Ru/Al_2O_3 catalyst at 240°C and in idealized reformate (CO: 1 %, H_2: 1-20 %), respectively. The high reaction order of H_2 over of the Ru/zeolite catalyst may be a reason for its high activity, compared to the Ru/Al_2O_3 catalyst.

3.2.3 DRIFTS measurements

In order to characterize the temporal evolution of the adsorbed surface species during the methanation reaction, *in situ* IR measurements under the same reaction conditions as applied in the kinetic measurements described above (Figure 20) were performed. Sequences of DRIFT spectra, recorded during 1000 min reaction on the Ru/zeolite and the Ru/Al_2O_3 catalyst in different reaction atmospheres, are shown in Figure 22 and Figure 23. The spectra are split into 3 frequency ranges, the region of the OH (4000-3500 cm^{-1}, top left) and CH_x (3000-2800 cm^{-1}, top right) stretch vibrations in the top panels, respectively, and the spectral range between 800 and 2300 cm^{-1} including the CO stretch (2300-1900 cm^{-1}) and the OCO bending (1600-800 cm^{-1}) vibrations (bottom panel). The temporal evolution of the different surface species was followed by the peak intensities. For reaction in ID-ref 6000 and CH_4-rich ID-ref 6000 (Figure 22), a fast build-up of signals in the CO region at 2075, 2036 and 1980 cm^{-1} on the Ru/Zeolite catalyst, and at 2030 and 1940 cm^{-1} on the Ru/Al_2O_3 catalyst is observed. On the latter catalyst, a dynamic equilibrium is reached after ~100 min, while on the Ru/zeolite catalyst the intensity decreased steadily until about 800 min of reaction. These signals are attributed to CO adsorbed on Ru [31;65;79;131-138]. The exact position depends on the pre-treatment of the catalyst and on the reaction conditions used in the experiment. The signal at 2036 cm^{-1} is commonly assigned to linearly adsorbed CO on Ru^0 [65;133;136;139]. In measurements on Ru/TiO_2 and Ru/Al_2O_3 catalysts, Londhe et al. [61] interpreted this signal as CO_{ad} linearly adsorbed on Ru, coadsorbed with and adjacent to O_{ad} species. Guglielminotti et al. [136] observed a similar signal during the methanation reaction on a completely pre-reduced (only Ru^0 species) Ru/TiO_2 catalyst, and related this to linearly adsorbed CO on Ru^0. Measurements performed at different CO pressures revealed that the wave number of the linearly bound CO_{ad} species depends on the coverage, in good agreement with results of CO adsorption experiments on Ru (0001) [139]. The signals at 1980 cm^{-1} and 1940 cm^{-1} observed on the Ru/zeolite and the Ru/Al_2O_3 catalyst, respectively, were related to a bridge bonded CO_{ad} adsorbed on Ru^0 [140]. Finally, the CO_{ad} related signal at higher wave numbers (2080 cm^{-1}), which is observed only on the Ru/Zeolite catalyst, is assigned to dicarbonyl CO species adsorbed on very small Ru clusters or atoms on the support. These Ru species were proposed to result from oxidative disruption of Ru-Ru bonds, and by some authors

identified as oxidized Ru^{n+} sites [132;134;135;138]. In previous studies on the hydrogenation of CO over Ru/Al_2O_3 and Ru/SiO_2 catalysts, this signal was accompanied by a peak at 2135 cm^{-1} which can be detected at longer reaction times in the experiments as well. It should be noted, however, that the quantification of this signal is hindered by its overlap with the gas phase CO signal. After reactive pretreatment, the CO adsorption behavior was similar as during reaction.

In the OH region, two peaks at 3740 and 3600 cm^{-1} are observed on the Ru/zeolite catalyst, which are related to structural silanol and/or isolated OH_{ad} groups on the support (Figure 22) [141;142]. They are visible already at the beginning of the reaction and do not change significantly in intensity during the reaction. On the Ru/Al_2O_3 catalyst, four additional OH_{ad} signals are present at 3680, 3650, 3620 and 3540 cm^{-1} during the reaction. With ongoing reaction, the intensity of the peak at 3740 cm^{-1} remains constant, whereas that of the other four signals decreases.

In the OCO region, peaks at 1590, 1440, 1040 and 915 cm^{-1} appear after about 100 min reaction on the Ru/Zeolite catalyst (Figure 22). They continuously increase in intensity and do not reach a steady-state during the reaction time. On the Ru/Al_2O_3 catalyst (Figure 22), the OCO region exhibits peaks at 1590, 1390, 1040 and 915 cm^{-1}, which appear after 35 min reaction and steadily increase in intensity. According to previous studies, peaks at ~1585 - 1590 and 1390 cm^{-1} result from the antisymmetric and symmetric bending vibrations of surface formates, respectively [26;30;136;143], which can be formed during the methanation reaction by reaction of CO with water. The corresponding C-H vibration, which was reported to appear at ~2902 cm^{-1}, appears here at ~2905 cm^{-1} (see below). As discussed in earlier studies, these formate species are at least mainly located on the Al_2O_3 support [144], although additional adsorption on the Ru nanoparticles can not be ruled out. During methanation on Ru/TiO_2 and Ru/Al_2O_3 catalysts, Gupta et al. [30] and Dalla Betta et al. [26] also detected a peak at 1440 cm^{-1}, which they assigned to the OCO bending vibration of a surface carbonate species. In the present work, a comparable signal is only detected on the Ru/zeolite catalyst at 1440 cm^{-1}. Comparing with earlier methanol adsorption experiments on a $Cu\text{-}ZnO/Al_2O_3$ catalyst [145], the signal at 1040 cm^{-1} may be related to a methoxy or methanol species adsorbed on the support. It is usually accompanied by a peak at 1085 cm^{-1} [145], which is not observed here. Possibly, the latter peak is obscured by the intense signal at 1040 cm^{-1}. The peak at 915 cm^{-1} is tentatively assigned to a deformation mode of $CH_{2,ad}$ species

CO methanation:

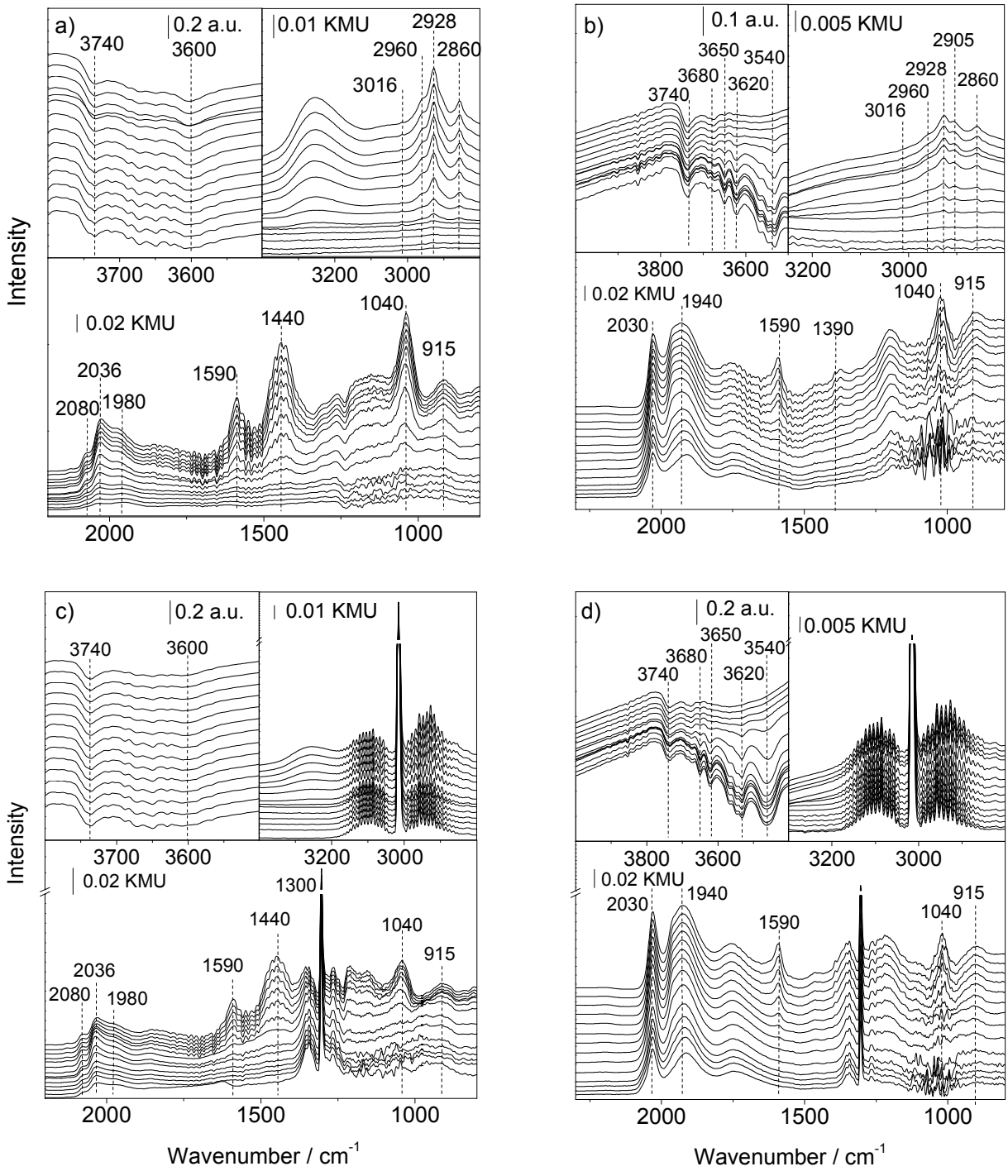

Figure 22: Sequences of DRIFT spectra recorded during 1000 min methanation reaction over the Ru/zeolite catalyst (a and c) (taken from [118]) and over the Ru/Al_2O_3 catalyst (b and d) at 190°C in a) and b) ID-ref 6000; c) and d) CH_4-rich ID-ref 6000(see Table 1 for abbreviations), The spectra were recorded after 1, 2, 3, 5, 7, 15, 35, 105, 195, 345, 495, 645, 795, 945 min reaction time (from bottom to top).

adsorbed on the Al_2O_3 support [145], pointing to possible CH_x chain growth on the support during the reaction [145]. Adding CH_4 to the idealized gas mixture, three additional peaks appeared at 1305 cm^{-1}, 1344 and 1264 cm^{-1}, which represent the Q, P and R branches of gas phase methane [65].

The CH spectral region (Figure 22 and Figure 23) shows the typical $CH_{x,ad}$ signals at around 3016, 2960, 2928, and 2860 cm^{-1}, arising from CH_4, $CH_{3,ad}$, and the symmetric and asymmetric $CH_{2,ad}$ vibrations on the two catalysts [27;65;79]. These surface species start to grow in after about five minutes reaction time. They increase further until reaching a steady-state after 340 and 1000 min reaction on the Ru/Al_2O_3 and Ru/zeolite catalyst, respectively. The shoulder at ~2905 cm^{-1} can be assigned to the CH vibration of a surface formate [26;30]. During reaction in the CH_4-rich reformate, the $CH_{x,ad}$ related signals are obscured by the strong CH_4 signal in the range of ~2800 cm^{-1}-~3200 cm^{-1} [65].

Comparing the reaction in ID-ref 6000 and in CH_4-rich ID-ref 6000 (Figure 22), no major differences in the surface species are found. The situation is very different, when the adlayer and its evolution with time are compared for the Ru/Al_2O_3 and the Ru/zeolite catalyst. Here a number of differences are observed, with the major ones being:

I) On the Ru/zeolite catalyst, the intensity of the signal at 2036 cm^{-1}, which is related to Ru-CO, decays slowly with time, and this decay agrees perfectly with the slight deactivation of the catalysts with time (Figure 20 and Figure 24). For the Ru/Al_2O_3 catalyst, the signal is stable, and this catalyst is essentially stable against deactivation.

II) The CO_{ad} signal on oxidized Ru at 2080 cm^{-1} is observed only on the Ru/zeolite catalyst and absent on the Ru/Al_2O_3 catalyst.

III) On the Ru/Al_2O_3 catalyst, additional signals related to OH_{ad} groups are observed at 3680, 3650, 3620 and 3540 cm^{-1}.

IV) The build-up of surface carbonates is negligible on the Ru/Al_2O_3 catalyst, whereas on the Ru/zeolite catalyst surface carbonate growth is strong.

The close correlation in the time dependences of the CO methanation activity and the time evolution of the signal intensity at 2036 cm^{-1} indicates that the same Ru^0 sites active for CO adsorption are also active for the methanation reaction, making the number of Ru^0 surface sites crucial for the reaction. The CO_{ad} on Ru^0 sites visible in IR may be directly involved in the reaction, but this is not necessarily required, and,

though unlikely, they may also act as spectator species. This correlation and therefore also the mechanistic conclusion are true for both catalysts.

Gupta et al. had suggested that at lower temperatures (<220°C) Ru^{n+}-$(CO)_m$ species represent the active species [32]. Other groups [65;143;146], however, have questioned this proposal because of the rather weak adsorption of CO on Ru^{n+} sites and the resulting low steady-state coverage of these species under reaction conditions. Furthermore, the weak interaction between Ru^{n+} sites and CO is likely to result in a less pronounced weakening of the C-O bond compared to bonding on Ru^0 sites, due to a lower population of the antibonding 2π* orbital of the CO_{ad}. Contributions from oxidized Ru^{n+} sites and Ru^{n+}–CO species can not be ruled from the present data, but are also not supported by them.

Another difference between the Ru/Al_2O_3 and the Ru/zeolite catalyst lies in the stability of the Ru nanoparticles. For the Ru/zeolite catalyst, a decrease by ca. 20% of the signal at 2036 cm^{-1} was observed, which is related to linear adsorbed CO_{ad} on Ru^0, after 105 min on stream, and a similar intensity decrease was observed also for the other Ru-CO signals. This can be explained in two ways, either by sintering or reductive agglomeration of the Ru particles, which was also suggested by Solymosi et al. [134], or by partial covering of the Ru surface by adsorbates such as $CH_{x,ad}$ species. The decay in Ru surface area active for CO adsorption is not correlated with a decrease or increase of the IR signals related to other surface species (e.g., $CH_{x,ad}$, surface formates or surface carbonates). During the methanation reaction on the Ru/Al_2O_3 catalyst, the Ru^0- CO related signals are stable after about 100 min.

From the absence of any correlations between the temporal evaluation of surface formates and surface carbonates on the one hand and the methanation activity on the other hand it is concluded that the reaction is not dominated by the reaction/decomposition of either of these surface species.

The relative intensities and the temporal evolution of the $CH_{x,ad}$ related intensities differ widely on both catalysts, with the relative intensities being higher on the Ru/zeolite catalyst. On the same catalyst, the signal intensities and hence the coverages of the related surface species reach a dynamic equilibrium situation after about 1000 min, while on the Ru/Al_2O_3 catalyst this occurs after 340 min. Most simply this is explained by either a much slower build-up of the $CH_{x,ad}$ species on the Ru/zeolite catalyst or their faster decomposition on the Ru/Al_2O_3 catalyst. This agrees also with the lower steady-state coverage of these species on the Ru/Al_2O_3 catalyst.

In addition, due to the higher surface area of the Ru/zeolite support, more adsorption sites for the $CH_{x,ad}$ species are expected. The $CH_{x,ad}$ species were suggested as intermediates in the methanation reaction [28;147] will be discussed later in more detail (section 3.2.4).

The role of surface formates and carbonates, which are formed by reaction of CO with H_2O during the methanation reaction, is not clear yet. Since carbonates are only present on the Ru/zeolite catalyst, it is more likely that these species represent reaction side products. Regarding the role of the surface formates, several groups proposed them to be side products of the reaction [26;27;30]. Praire et al. [73] suggested that during CO_2 methanation surface formates may serve as a reversible CO reservoir. The role of the surface formates will be discussed in more detail in section 3.2.4.

Selective methanation

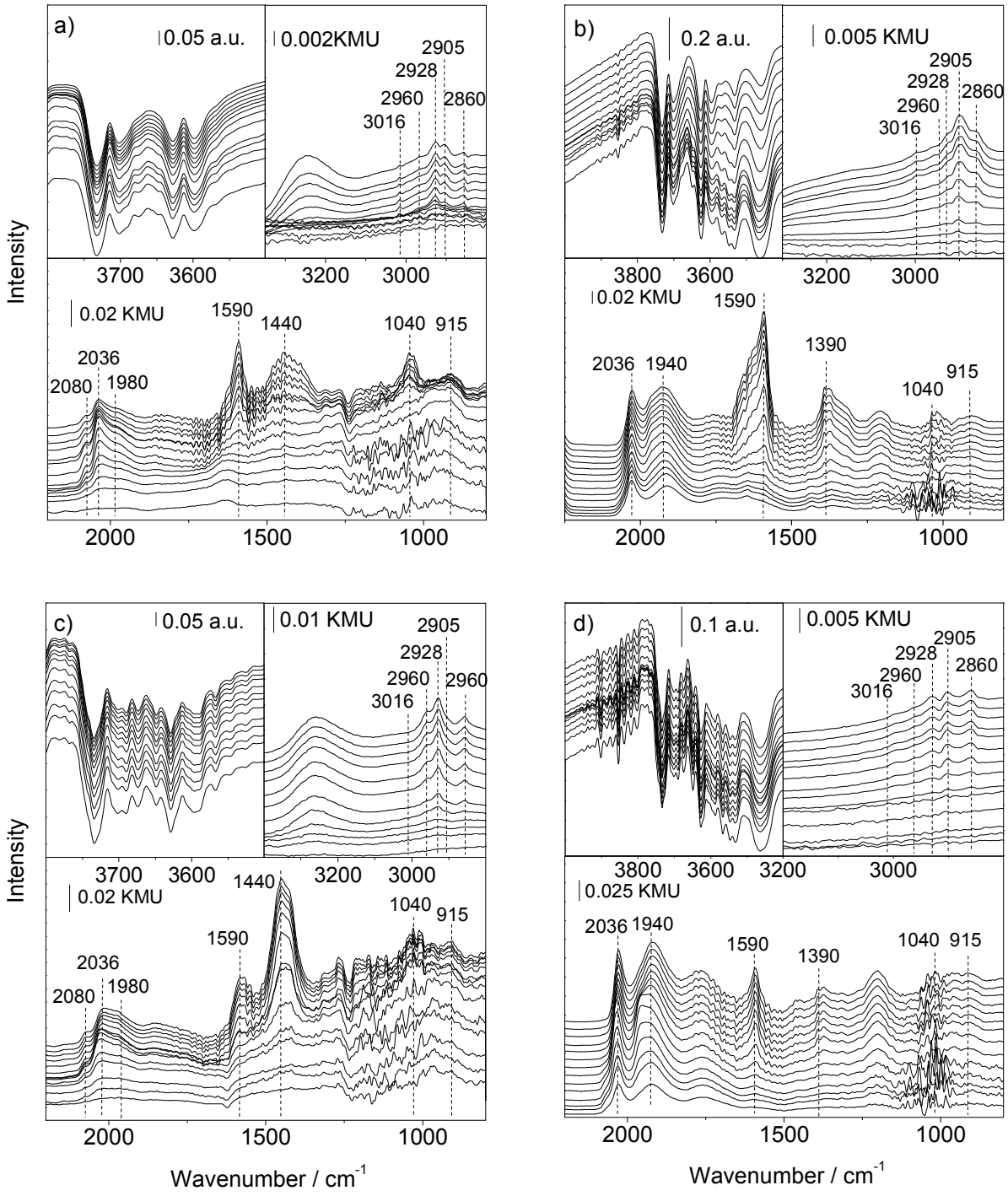

Figure 23: Sequences of DRIFT spectra recorded during 1000 min methanation reaction over the Ru/zeolite catalyst (a and c) (taken from [118]) and over the Ru/Al_2O_3 catalyst (b and d) at 190°C in a) and b) SR-ref 6000 (see Table 1 for abbreviations); c) and d) H_2O-rich SR-ref 6000 (see Table 1 for abbreviations).The spectra were recorded after 1, 2, 3, 5, 7, 15, 35, 105, 195, 345, 495, 645, 795, 945 min reaction time (from bottom to top).

Similar *in situ* DRIFTS experiments as described above were performed in SR-ref 6000 and in H_2O-rich SR-ref 6000, containing both CO and CO_2 (Figure 23). The general characteristics of the resulting spectra are rather similar to those obtained in idealized reformate (Figure 22), with the following differences:

I) The presence of CO_2 leads to overtone signals of CO_2 in the OH region on both catalysts; therefore the intensities related to the OH groups could not be evaluated.

III) The tendency for surface formate and/or carbonates formation is more pronounced (higher steady-state coverage) on both catalysts in these reaction atmospheres compared to reaction in CO_2-free idealized reformates.

III) In H_2O-rich semi-realistic atmosphere, a signal at 2075 cm^{-1} (shoulder) is detected also on Ru/Al_2O_3, which was not observed in the other gas-mixtures. It is attributed to CO_{ad} on oxidized Ru^{n+} species.

IV) For the Ru/zeolite catalyst, the temporal evolution of the CO_{ad} species changes in the presence of H_2O (H_2O-rich semi-realistic reformate) compared to all H_2O free reaction mixtures, leading to much lower CO_{ad} coverages during the reaction.

It is interesting to note that among the different additional components only water has a negative effect on the adsorption behavior of CO on Ru (Figure 23 c), and only on the Ru/zeolite catalyst. In the presence of water vapor, the intensity of linear and bridge bonded CO_{ad} species on Ru^0 decreased compared to reaction in water-free atmosphere. This is may be due to a blocking of adsorption sites by adsorbed water or, alternatively, by Ru (surface) oxidation. The CO_{ad} species adsorbed on oxidized Ru, however, does not seem to be influenced much by water addition, and the total amount of Ru^{n+}-CO species stays the same. Together with the lower intensity in the Ru^0–CO signal, also the CO methanation activity is lower in H_2O-rich atmosphere than in H_2O-free atmosphere, and both of them decrease slowly with time. On the other hand, for the Ru/Al_2O_3 catalyst, the presence of water in the reaction atmosphere leads to a signal at 2080 cm^{-1} (formation of a small shoulder), while neither the intensity of the 2036 cm^{-1} signal nor the CO methanation activity are lower in the presence of H_2O than in (H_2O-free) semi-realistic reformate. The observed close correlation between Ru^0–CO signal intensity and the CO methanation activity also upon changing to a H_2O-rich gas mixture provides further support for the above conclusion that the activity of the Ru catalysts is closely correlated with the number of accessible Ru^0 sites in the reaction.

The addition of CO_2 has a direct influence on the formation of surface carbonate and/or formate species on both catalysts. The intensity of the signal at ~1590 cm^{-1}, which is related to surface formate species, grows very fast on the Ru/zeolite catalyst and reaches an even higher value than that of the surface carbonate related peak at ~1440 cm^{-1} , while this is opposite in idealized reformate. The same trends are observed for the Ru/Al_2O_3 catalyst. Praire et al. [73] had shown that CO_2 and H_2 react to a formate species on Ru/TiO_2 and Ru/Al_2O_3 catalysts, which explains the increased tendency for surface formate formation of the catalysts upon CO_2 addition. The addition of water, on the other hand, suppresses the build-up of formates. Most likely, this proceeds via an enhanced formate decomposition, since a dynamic equilibrium is reached after 200 min. Marwood et al. [148] observed similar trends during the CO_2 methanation reaction, finding a strong decrease of the surface formate species with increasing water concentration. This may be due to blocking of adsorption sites by OH_{ad} groups or due to water induced faster decomposition of the surface formates. Finally, the build-up of the surface carbonates (1440 cm^{-1}) increases on the Ru/zeolite catalyst when adding water to the gas-mixture (Figure 23 c).

Comparing the temporal evolution of the CO methanation activity (Figure 20) with the results of the above DRIFTS experiments reveals a distinct correlation between the time dependence of the activity and the intensities/concentrations of the Ru^0–CO species (Figure 24). The kinetic measurements show, after a subtle initial increase during the first ~50 min, a slow decay of both the methanation activity and the Ru^0–CO signal intensity with time, by about 20% over 1000 min on stream, whereas for the Ru/Al_2O_3 catalyst, both remain constant with time.

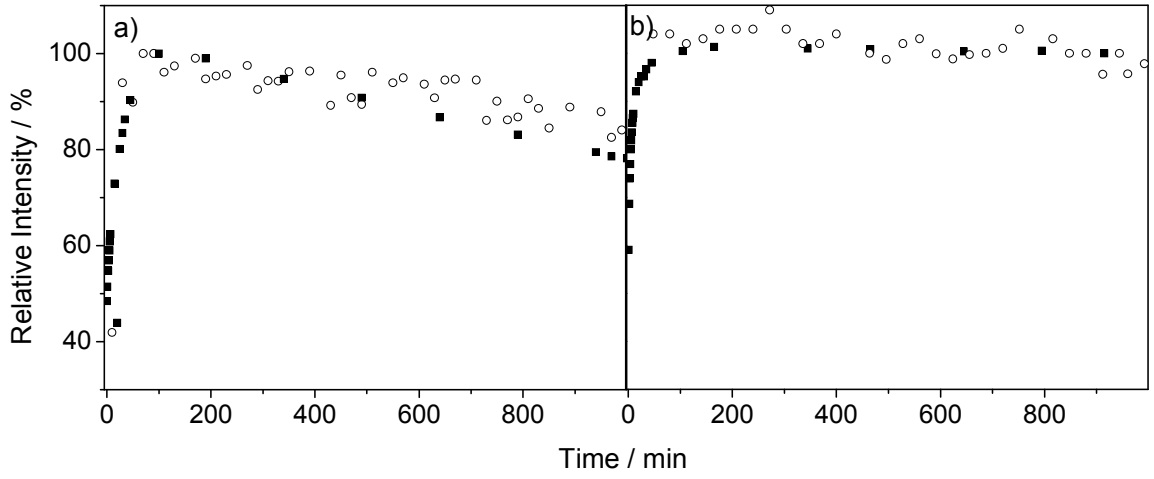

Figure 24: Relative intensity development of the Ru-CO band and the relative CO methanation activity for (a) the Ru/zeolite and (b) Ru/Al_2O_3 catalyst; (■) CO_{ad} band intensity (○) methanation rate

Furthermore, the lower activity of the Ru/zeolite catalyst in H_2O-rich SR-ref 6000 relative to the other gas mixtures (see section 3.2.2) goes along with a lower Ru^0–CO signal intensity. The close correlation lead to the proposal that the number of active sites is closely related to the number of Ru^0 sites, and that they are likely to represent active sites in the methanation reaction on both catalysts (see earlier discussion in this section).

The surface formates and carbonates increase steadily in intensity, and the $CH_{x,ad}$ species seem to saturate between 900 and 1000 min on the Ru/zeolite catalyst and after 340 min on the Ru/Al_2O_3 catalyst, respectively. Hence, there is no simple correlation between the intensity and concentration behavior of any of these species and the methanation activity. Therefore it is not likely that the reaction is dominated by the reaction/decomposition of any of these surface species, which will be discussed in more detail in the following section.

3.2.4 Transient experiments

After following the build-up of the surface species during the methanation reaction in adsorption transients in different reaction atmospheres on the Ru/Al_2O_3 and Ru/zeolite catalysts in the last section, the stability of these surface species in ID-ref 6000 in decomposition transients were evaluated. This was done by following their transient behavior upon replacing CO in the reaction atmosphere by N_2 after 1000 min reaction, i.e., by changing from a CO/H_2 mixture to a N_2/H_2 atmosphere. The temporal evolution

of the signal intensities related to $CH_{x,ad}$, surface formate and surface carbonate species was evaluated from a sequence of DRIFT spectra recorded upon $CO/H_2 \leftrightarrow N_2/H_2$ exchange.

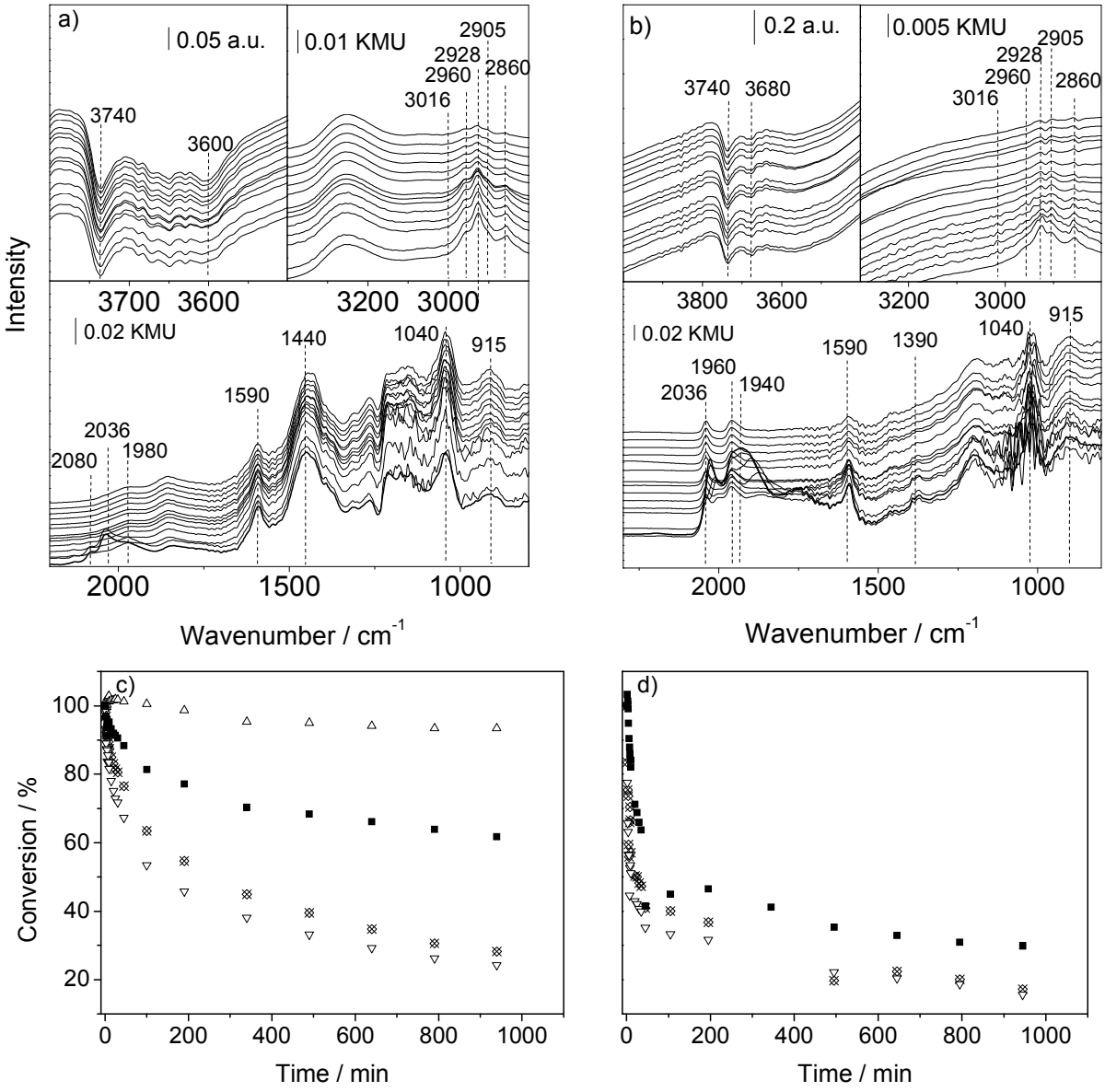

Figure 25: Upper Panels: Sequences of DRIFT spectra recorded upon exchanging CO by N_2 in the reaction gas mixture over a) the Ru/zeolite catalyst (taken from [118]) and b) the Ru/Al_2O_3 catalyst at 190°C in ID-ref 6000 (see Table 1 for abbreviations) after 1000 min reaction. The spectra were recorded after: 0 min (end of the 1000 min reaction), 1, 2, 3, 5, 7, 15, 35, 105, 195, 345, 495, 645, 795, and 945 min (from bottom to top).
Bottom Panels: Relative intensities of the $CH_{x,ad,}$ surface formate and surface carbonate related signals at 2958 cm^{-1}, 2927 cm^{-1},2857 cm^{-1},, 1590 cm^{-} and at 1440 cm^{-1} during the transient experiment on the Ru/zeolite (c) and the Ru/Al_2O_3 (d) catalyst. (△) surface carbonate, (■) surface formate, (▽) $CH_{2,ad}$, (※) $CH_{3,ad}$.

The resulting changes in the adlayer on the Ru/zeolite and on the Ru/Al_2O_3 catalyst are illustrated in Figure 25. On the Ru/zeolite catalyst (Figure 25a), the CO_{ad} related signals vanish within the first 3 min. Also on the Ru/Al_2O_3 catalyst (Figure 25b), the CO_{ad} signal decreases within 3 min, but does not disappear completely. Even 1000 min after the exchange, two peaks at 2040 and 1960 cm^{-1} are present, which indicate the presence of linear and bridged bonded CO_{ad} on Ru^0. The rapid decay of the CO_{ad} related intensity is explained by CO_{ad} reaction, e.g., with the H_2 present in the gas phase, and by CO_{ad} desorption. The reason for the persistence of the remaining CO_{ad} signals is still unclear.

Following the intensities related to surface formates, surface carbonates, $CH_{2,ad}$ and $CH_{3,ad}$ at 1590, 1440, 2928 and 2960 cm^{-1} on the Ru/zeolite catalyst, respectively, it is obvious that all of these species decrease in concentration with time. The stability of these species follows the order surface carbonate > surface formate > $CH_{3,ad} \geq CH_{2,ad}$. Since the initial rate of the decrease in intensity is low for the surface carbonates and formates, and certainly well below the methanation rate [149], it is suggested that these species are side products. The $CH_{x,ad}$ species adsorbed on the support of the catalyst (they are formed also on the pure zeolite) show the highest relative decrease in intensity, decreasing to 30% of the value after 1000 min reaction.

On the Ru/Al_2O_3 catalyst, the intensities of the adsorbed surface species decrease much more rapidly than on the Ru/zeolite catalyst. Within the first 45 min, the signals related to surface formates and $CH_{x,ad}$ species decay to almost their final intensity, and then remain essentially constant. The intensity loss of the $CH_{x,ad}$ related signals (2960, 2928, 2860 cm^{-1}) is about 80%, which is even more pronounced than on the Ru/zeolite catalyst, while the formate intensities decrease by about 60% relative to the initial intensity (after 1000 min reaction). Surface carbonates were not formed on this catalyst during the reaction. Finally, the signals of the methoxy species and of the $CH_{2,ad}$ species at 1040 and 915 cm^{-1}, respectively, increase rather than decrease in intensity upon changing from $CO/H_2 \rightarrow N_2/H_2$. This increase in methoxy species, which probably results from other adsorbed surface species such as surface formates, indicates that these are not part of the reaction chain. The growing intensity of the 915 cm^{-1} signal is attributed to accumulation of $(CH_2)_x$ chains on the surface [145].

Ekerdt and Bell suggested that $CH_{x,ad}$ species are side products in the methanation reaction [27]. They concluded this from transient isotope labeling IR experiments. Yamasaki et al. [28] also investigated the reaction pathway of CO and hydrogen on a

Ru/SiO_2 catalyst. They used an indirect method proposed by Wexler [150] for quantifying the coverages of the adsorbed methylene and methyl groups, and calculated the mean chain length of adsorbed hydrocarbon chains from the ratio of these groups. From transient IR experiments, they proposed a complex mechanism for the CO methanation reaction, where $CH_{x,ad}$ species act as reaction intermediates and CH_4 formation proceeds via formation and decomposition of adsorbed hydrocarbon chains [28]. Since, however, the authors could not demonstrate that the decomposition rate of the hydrocarbon chains under steady-state conditions corresponds quantitatively to the CH_4 formation rate, definite proof for this proposal is still missing.

For more quantitative information on these aspects, in particular on the correlation between decomposition of the $CH_{x,ad}$ species and CH_4 formation rate on the Ru/zeolite catalyst, a similar transient experiment as shown in Figure 25 was performed, but following the decay of the CH_4 formation rate by a mass spectrometer. The resulting CH_4 formation transient, recorded upon changing from a CO/H_2 mixture to an Ar/H_2 mixture under similar reaction conditions as before (see Figure 25), is plotted in Figure 26.

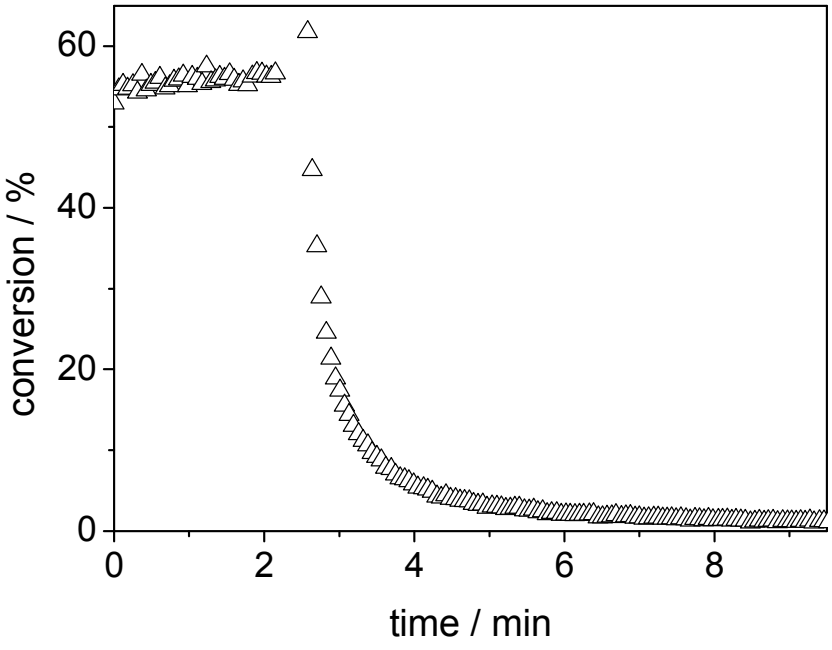

Figure 26: Transient activity measurement of Ru/Zeolite upon exchange of CO by Ar under ID-ref 6000 (see Table 1 for abbreviations) after 1000 min reaction at 190°C; △: CH_4 conversion

Upon changing from the reaction mixture to the Ar/H_2 mixture, the formation of CH_4 decreases rapidly and reaches the background level within 3 to 4 min. For comparison, the decay of the IR intensities related to $CH_{2,ad}$ and $CH_{3,ad}$ proceeds on a much longer time scale (Figure 25). After 100 min exposure to Ar/H_2, the related signals show still more than 50% of their initial intensity, and the further decay of the $CH_{x,ad}$ related signals is rather slow. Even after 1000 min exposure to an Ar/H_2 mixture, the intensity of these signals is still around 25% of the initial value. Hence, hydrogenation of the $CH_{x,ad}$ species visible in IR to $CH_{4,ad}$ and its subsequent rapid desorption can not represent the rate limiting step for CH_4 formation. The question for the rate limiting step and the nature of the reaction intermediate in the dominant reaction pathway is, at least from the experimental point of view, still open. Based on the present data, the $CH_{x,ad}$ species visible in the IR spectra represent spectator species, whose reaction to CH_4 is much slower than required for explaining the observed CH_4 formation rate. Therefore, the formation and hydrogenation of the $CH_{x,ad}$ species visible in IR can not represent the dominant reaction pathway. This conclusion agrees well with recent predictions based on density functional theory calculations [37;64;72], which favor a reaction pathway via formyl formation rather than via C-O bond splitting and subsequent hydrogenation. Based on the similar trends in the DRIFTS transients shown in Figure 25, it is expected that these mechanistic conclusions are valid for both Ru catalysts, although the removal of the adsorbed $CH_{x,ad}$ species is faster on the Ru/Al_2O_3 catalyst than on the Ru/zeolite catalyst.

3.2.5 Summary

The selective methanation of CO in different CO_2 containing reformates on a 2.2 wt.% Ru/zeolite catalyst and, for comparison, on a 5 wt.% Ru/Al_2O_3 catalyst by temperature screening measurements, kinetic measurements under differential reaction conditions and by transient *in situ* DRIFTS and mass spectrometric measurements was investigated. The latter experiments focused on the build-up of adsorbed surface species during the reaction and their decomposition upon replacing the CO/H_2 mixture in the reaction gas by a N_2/H_2 mixture. These measurements led to the following results:

Temperature dependent conversion measurements showed that both catalysts are active for the selective methanation reaction. Under present reaction conditions, full

conversion of CO was achieved at 200°C and 230°C for the Ru/zeolite and the Ru/Al_2O_3 catalyst, respectively, in ID-ref 6000. The addition of water and methane did not influence the CO methanation activity on the Ru/zeolite catalyst and caused only minor changes in the CO conversion on the Ru/Al_2O_3 catalyst. The addition of CO_2 (CO_2-rich idealized reformate) led to an acceleration of the reaction on the Ru/zeolite catalyst, where complete CO conversion (T_{100}) was reached now at 190°C. On that catalyst, CO_2 methanation started after complete CO conversion, and the selectivity for CO conversion remained above 85% over a temperature range of 40°C. On the Ru/Al_2O_3 catalyst, CO_2 conversion started at 200°C, where CO still was still left in the reformate. With increasing temperature, both CO and CO_2 are converted and at full CO conversion the selectivity for CO methanation has decreased to 48% under present reaction conditions. In the absence of CO, in CO_2/H_2 mixtures, the CO_2 conversion exhibits similar conversion characteristics as the CO conversion on the Ru/Al_2O_3 catalyst. On the Ru/zeolite catalyst, in contrast, the onset of CO_2 conversion is shifted to lower temperature (170°C), and the subsequent increase in conversion is rather slow, reaching full conversion only at 410°C. The latter behavior points to a kinetic hindrance in CO_2 methanation, in the absence and presence of CO.

Kinetic measurements performed under differential conditions exhibited an ~10 - ~20 times higher Ru mass normalized reaction rate over the Ru/zeolite catalyst compared to the Ru/Al_2O_3 catalyst, depending on the reaction gas. For the inherent activity, expressed by the turnover frequency, the differences are also distinct with factors between 3.9 and 7.3, which correspond to TOFs between 3.9 and 8 s^{-1} on the Ru/zeolite catalyst, depending on the reaction atmosphere. Temperature dependent measurements, performed in idealized reformate after 1000 min on stream in the range 190-160°C, revealed comparable apparent activation energies for both catalysts under these conditions, pointing to a similar rate limiting step on both catalysts. On the Ru/Al_2O_3 catalyst, reaction orders of -0.5 and 1.0 were obtained for CO and H_2, respectively. Higher reaction orders of -0.7 and 2.7 for CO and H_2, respectively, were observed on the Ru/zeolite catalyst. One may speculate that the high value for the reaction order of H_2 is linked to the high activity of this catalyst.

In situ IR (DRIFTS) measurements showed that exposing the catalysts to different reaction mixtures under reaction conditions leads to the immediate adsorption of linearly and bridge bonded CO_{ad} species on Ru^0 sites on both catalysts. On the Ru/zeolite catalyst, an additional signal appeared at higher frequency (2075 cm^{-1}),

which is attributed to CO_{ad} on Ru^{n+} sites. This species was not observed on the Ru/Al_2O_3 catalyst in H_2O-free reaction atmospheres, whereas in the presence of water a small shoulder of this signal developed, due to the more oxidizing reaction conditions. In addition, on both catalysts the build-up of surface formates and $CH_{x,ad}$ species were observed, while surface carbonates were formed on the Ru/zeolite catalyst only. Thus, the presence of a Ru^{n+}-CO species and the observation of an additional OH_{ad} signal are the most striking differences in the IR spectra between the two catalysts.

The temporal evolution of the DRIFTS signals related to the different adsorbed CO surface species differs significantly between the two catalysts. On the Ru/zeolite catalyst, the intensity of the CO_{ad} related signals passes through a maximum after 100 min reaction, whereas for the Ru/Al_2O_3 a steady-state situation is reached at the same time. The signals related to surface formates and carbonates do not saturate during 1000 min on stream, those related to $CH_{x,ad}$ species reach a dynamic equilibrium after about 1000 min on the Ru/zeolite catalyst and after 340 min on the Ru/Al_2O_3 catalyst, respectively.

From the close correlation between Ru^0–CO signal intensity and the methanation activity on both catalysts, which is observed in the time dependent behavior and also when comparing different gas mixtures, it is proposed that the activity in the methanation reaction is determined by the number of accessible Ru^0 sites on the two catalysts. Ru^0–CO species may act as active sites and active species, but other species adsorbed on Ru^0 sites may be possible as well. On the other hand, the absence of such correlations between surface formates and surface carbonates and methanation activity indicates that the reaction is not dominated by the reaction/decomposition of either of these surface species.

Changing from CO-containing to CO-free reaction atmosphere after 1000 min on stream in idealized reformate, surface formates and $CH_{x,ad}$ species disappear with time on both catalysts. The initial rate of decomposition, however, differs significantly from the steady-state reaction rate. Therefore, the reaction between the $CH_{x.ad}$ species visible by IR and hydrogen can not represent the rate limiting step in the *dominant reaction pathway. The same experiment performed with a mass spectrometer shows that CH_4 is not produced anymore after three minutes upon switching to an Ar/H_2 mixture, providing further support for the above conclusion. The

signals representing (-CH_2-) chain groups were growing even after replacement of CO, and are therefore identified as side products.

The kinetic and DRIFTS measurements showed that both Ru catalysts are active and selective for the CO methanation even at low temperatures (190°C). Using zeolite as support material, the Ru catalyst shows significantly higher activity and selectivity, probably due to specific interactions between the more acidic support and the Ru nanoparticles and via the stabilization of very small metallic and partly oxidic Ru particles, which result in pronounced modifications of the intrinsic Ru surface activity described by turnover frequencies. The higher surface area of the zeolite support may further contribute to the better performance of this catalyst.

3.3 Reaction intermediates and side products in the methanation of CO and CO_2 over supported Ru catalysts in H_2-rich reformate gases

The previous sections gave insight in the general reaction characteristics and proved that the spectroscopically observed CH_x species are unlikely to take part in the dominant reaction pathway. This section will elucidate the reaction intermediates of the CO and the CO_2 methanation on the supported Ru catalysts. Aiming at a mechanistic understanding of the CO and CO_2 methanation reaction over supported Ru catalysts and the underlying physical reasons for the mechanism, the methanation of CO and CO_2 over a Ru/zeolite and a Ru/Al_2O_3 catalyst was investigated by *in situ* diffuse reflectance infrared Fourier transform spectroscopy (DRIFTS) measurements, in idealized and CO_2-rich reformate gases, employing quantitative steady-state isotope transient kinetic analysis (SSITKA) techniques, where one educt, e.g., ^{12}CO is replaced by its isotopomer ^{13}CO.

The results of the following sections were published in the Journal of Physical Chemistry C, 115 (2010) 1361: *Reaction Intermediates and Side Products in the Methanation of CO and CO_2 over Supported Ru Catalysts in H_2-Rich Reformate Gases.*

3.3.1 CO methanation

In a first set of experiments, reaction intermediates and side products of the CO methanation on the Ru/zeolite and Ru/Al_2O_3 catalyst, respectively, were investigated and characterized in idealized reformate ($CO/H_2/N_2$) by sequences of *in situ* DRIFTS measurements (Figure 27). The relative intensities of the respective surface species (HCO, CH_4 and CO) are plotted as function of time in Figure 28. The characteristic bands arising on the Ru/zeolite and the Ru/Al_2O_3 catalyst from the interaction with the reaction atmosphere are evident from the spectra presented in Figure 27 a and Figure 27 b, which were recorded during 1000 min on stream. Panels Figure 27 c and Figure 27 d, show the resulting spectra of the first 40 minutes during the SSITKA measurement, where after 1000 min of reaction one educt (^{12}CO) was replaced by its isotope labeled analog (^{13}CO). This procedure allowed me to distinguish between reaction intermediates and side products, since in the first case the signal of the respective

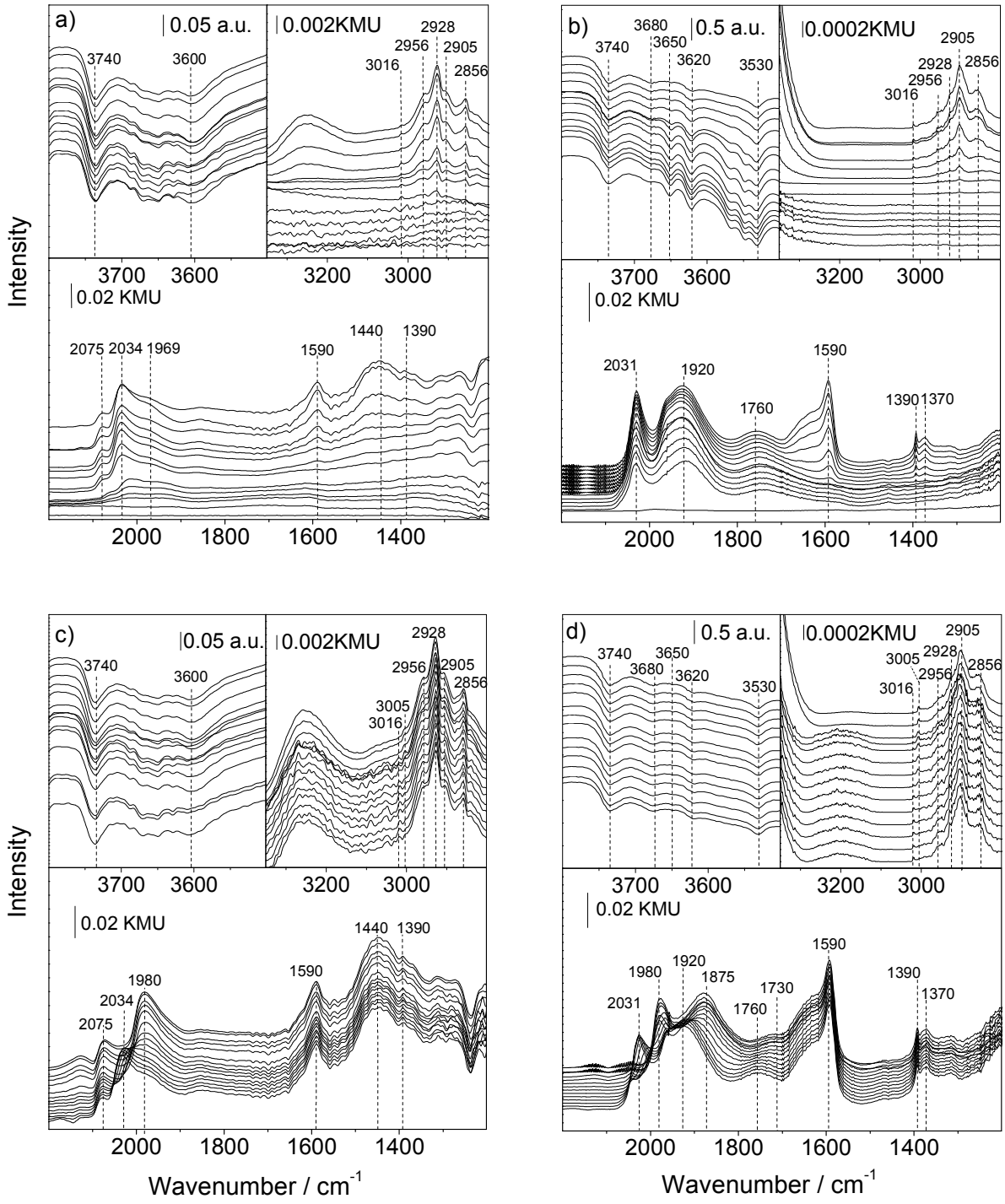

Figure 27: Sequences of DRIFT spectra recorded during 1000 min methanation reaction at 190°C (equilibration of surface species) over the Ru/zeolite (left panels) and the Ru/Al_2O_3 catalysts (right panels) in ID-ref 6000 (see Table 1 for abbreviations) and subsequent change to ^{13}CO containing atmosphere. (a), (b): ^{12}CO containing reaction atmosphere, (c) and (d): ^{13}CO containing reaction atmosphere; from bottom to top: (a) and (b) 0, 2, 3, 5, 7, 15, 45, 105, 195, 345, 495, 645, 795, 915 min; (c) and (d): 1000, 0.25, 0.5, 0.75, 1, 1.25, 1.5 1.75, 2, 2.25, 3, 5, 7, 10, 45 min.

surface species should decrease fast, and in the latter case, the respective signals will prevail while a new signal belonging to the ^{13}C containing species will start to grow in.

The assignments of the main bands (see lines) will be briefly summarized below, a detailed discussion was given in section 3.2.3.

During reaction in idealized reformate (Figure 27 a and Figure 27 b) on both catalysts characteristic signals are observed in the CO_{ad} region at ~2034 cm^{-1} and 1969 on the Ru/zeolite and at 2031 and 1920 cm^{-1} on the Ru/Al_2O_3 catalyst, respectively, which are generally attributed to CO adsorbed linearly or in a bridged configuration on Ru [31;65;79;132-134;136-138;151]. A signal at 2075 cm^{-1}, only appearing on the Ru/zeolite, is usually attributed to CO adsorbed on oxidized Ru^{n+} or coadsorbed with O_{ad} on Ru [65;132;152]. Again, no evidence is found for a band at 2075 cm^{-1} on the Ru/Al_2O_3 catalyst. A dynamic equilibrium of- the adsorbed CO_{ad} surface species is reached after 100 min on both catalysts.

In the OH region, two peaks at 3740 and 3600 cm^{-1} appear on the Ru/zeolite catalyst, which is related to silanol and structural or isolated OH_{ad} groups on the support [141;142] and which do not change during reaction. On the Ru/Al_2O_3 catalyst, the peak at 3740 cm^{-1} is accompanied by four additional OH_{ad} signals at 3680, 3650, 3620 and 3530 cm^{-1}, which were attributed to OH groups on different Al_2O_3 crystal facets [141]. With ongoing reaction, the intensity of the peaks at 3735 and 3670 cm^{-1}, attributed to terminal and isolated OH groups, remains constant, whereas that of the other two signals decreases.

The CH_x spectral region shows the typical $CH_{x,ad}$ signals at 3016, 2956, 2928, and 2856 cm^{-1}, arising from CH_4, $CH_{3,ad}$, and the symmetric and asymmetric $CH_{2,ad}$ vibrations on the two catalysts [27;65;79]. On both catalysts, these species (except for CH_4) start to grow in after about 15 min of reaction and reach a steady-state situation after 340 minutes on the Ru/Al_2O_3 catalyst and after 1000 minutes on the Ru/zeolite catalyst. For the CH_4 signal, steady-state is reached much faster on both catalysts, after about 10 min. A shoulder at ~2905 cm^{-1} observed on both catalysts was assigned to the C-H vibration of a surface formate [26;30].

In the OCO region, bands at 1590, 1440 and 1390 cm^{-1}, which appear after about 100 min on stream on the Ru/zeolite catalyst, were assigned to surface formates (1590 and 1390 cm^{-1}) and carbonates (1440 cm^{-1}) [26;30;136]. On the Ru/Al_2O_3 catalyst, the corresponding bands start to grow in after 45 min of reaction at 1590, 1390, 1370 cm^{-1}

(additional formate vibration). The carbonate band is missing on this catalyst. An additional band at 1760 cm^{-1} is ascribed to adsorbed HCO species [36;153]. While this band is clearly visible on the Ru/Al_2O_3 catalyst, it is not seen on the Ru/zeolite catalyst. In addition Wu and Goodman [154] could observe such a signal on a Ru single crystal after admission of H_2 to a CO_{ad} covered surface. Admission of only CO did only result in linearly CO_{ad} at 2030cm^{-1}. They ascribed this signal to a weakened CO_{ad} species, due to coadsorption / perturbation of hydrogen and proposed it as intermediate during CO hydrogenation. Visconti et al [155] observed a similar feature during Fischer-Tropsch reactions on Co/Al2O3 catalysts describing as CHO_{ad} species. On both catalysts, the bands in the OCO region (except for the HCO band) grow steadily and do not saturate over 1000 min.

Sequences of DRIFT spectra, recorded after changing from ^{12}CO to ^{13}CO after 1000 min on stream on the Ru/zeolite and the Ru/Al_2O_3 catalysts, are shown in Figure 27 c and Figure 27 d. For more clarity, only spectra recorded during the first 40 min after the exchange step are shown, since the relevant changes of the adsorbed surface species occur on a short time scale (~10min).

On the Ru/zeolite catalyst, the $^{12}CO_{ad}$ signals at 2075 and 2034 cm^{-1}, belonging to linearly adsorbed CO_{ad} on Ru^{n+} and on Ru^0, respectively, vanish within the first three minutes after the substitution by ^{13}CO, and the respective $^{13}CO_{ad}$ signals start to grow in at 1980 cm^{-1} (linearly adsorbed $^{13}CO_{ad}$). The same happens on the Ru/Al_2O_3 catalyst with the respective $^{12}CO_{ad}$ signals at 2031 and 1920 cm^{-1} (linearly adsorbed CO_{ad} and bridge bonded CO_{ad}), which are replaced by signals at 1980 and 1875 cm^{-1} (linearly adsorbed and bridge bonded $^{13}CO_{ad}$). The signal related to linear $^{13}CO_{ad}$ on Ru^{n+} on the Ru/zeolite catalyst, which is expected at ~2040 cm^{-1}, is probably obscured by the prominent ^{13}CO gas phase signals at 2172 and 2072 cm^{-1}. The ^{12}CO signal at 1980 cm^{-1} ($^{12}CO_{ad}$ in a bridged configuration on Ru) on the Ru/zeolite catalyst does not seem to change, and a new signal at about 40 cm^{-1} lower wave number cannot be observed to grow in. The expected changes in the 1980 cm^{-1} band are obscured by the evolution of the prominent band at 1980 cm^{-1}, and the same is expected also for the weak shoulder expected at ~1940 cm^{-1}.

Hardly any changes are observed in the CH_x region, except for the anticipated replacement of the $^{12}CH_4$ signal at 3016 cm^{-1} by a $^{13}CH_4$ band at ~3005 cm^{-1} [156] within the first three minutes, comparable to the changes in the CO region. Since the

other CH_x surface species do not change, at least not on this time scale, they do not seem to be involved in the main reaction pathway to CH_4 (see section 3.2.4) [26;27]. It may, however, well be that significant amounts of inactive CH_x species (e.g. CH_x chains etc.) obscure the signals of active surface CH_x species. In the latter case it would hardly be possible to detect the active CH_x surface species and separate it from inactive species.

The OCO region shows almost no changes for the Ru/zeolite and the Ru/Al_2O_3 catalyst over the reaction time covered in these spectra (40 min). The formate and carbonate bands do not change in frequency, and also their intensity remains about constant. At longer reaction times (after 100 min, not shown), new formate bands related to the corresponding ^{13}C species appear in addition to those at 1590 cm^{-1} (Ru/zeolite), 1390 and 1370 cm^{-1} (Ru/Al_2O_3), indicating that these formate species are side products in the reaction rather than reaction intermediates, as already stated above (see section 3.2).

Only for the signal at 1760 cm^{-1} on the Ru/Al_2O_3 catalyst, attributed to an HCO_{ad} species, [36] the situation is different. Here, a new signal develops at a lower wave number at ~1730 cm^{-1}, while the signal at 1760 cm^{-1} decreases in intensity. The decrease of the HCO_{ad} signal at 1760 cm^{-1} agrees quantitatively with the increase of the new signal at 1730 cm^{-1}. Furthermore, the decrease/increase of these signals with time agrees qualitatively with that of the linearly adsorbed $^{13}CO_{ad}$ / $^{12}CO_{ad}$ species at 1981 and 2031 cm^{-1} and the $^{13}CH_{4,ad}$ / $^{12}CH_{4,ad}$ products at 3005 and 3017 cm^{-1}. This is illustrated in Figure 28 a, which shows the relative intensities of the different surface species ($^{12}CO_{ad}$, $^{13}CH_{4,ad}$, (inverted) $^{12}HCO_{ad}$ and $^{13}HCO_{ad}$) as a function of time. Since the rates of depletion of the $^{12}CH_{4,ad}$ and $^{12}CO_{ad}$ signals agree quantitatively with the rate of increase of the $^{13}CH_{4,ad}$ and $^{13}CO_{ad}$ signals, respectively, only the evolution of the $^{12}CO_{ad}$, $^{13}CH_{4,ad}$, (inverted) $^{12}HCO_{ad}$ and $^{13}HCO_{ad}$ signals are shown for clarity. To illustrate the quantitative agreement between the intensity loss of the ^{12}C isotopomer and the intensity growth of the ^{13}C isotopomer, the evolution of the $H^{13}CO_{ad}$ surface species and the inverted intensity of that species (1-I($H^{12}CO$)) is included, together with the intensity decay of the $H^{12}CO$ species, with time in Figure 28 a. These plots demonstrate that the intensity change upon $^{12}CO/^{13}CO$ exchange is fastest for the CO_{ad} related signals, while that of the HCO_{ad} related signals are somewhat slower, though on a similar time scale.

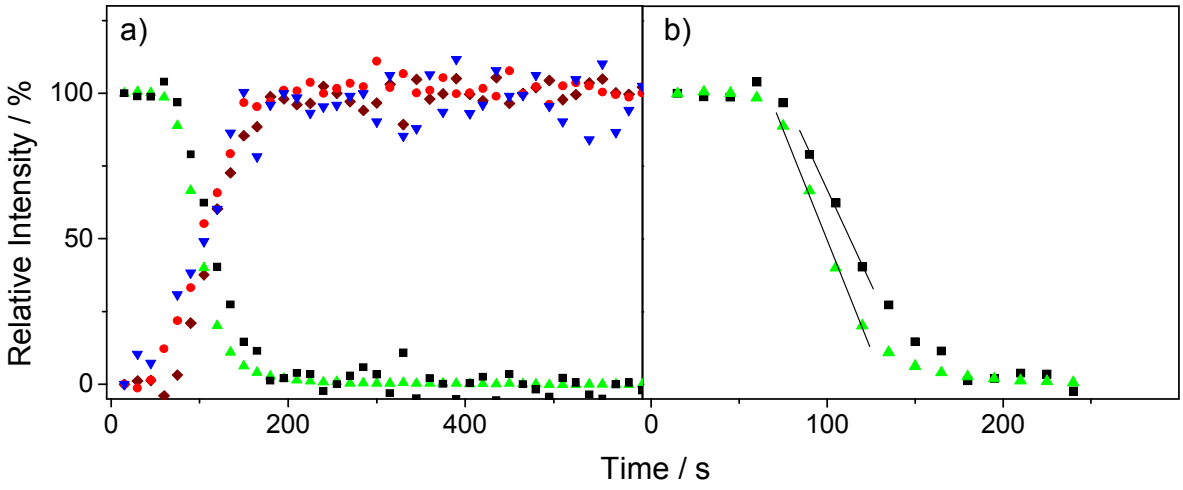

Figure 28: (a) Relative intensities of (▲) $^{12}CO_{ad}$, (■) $^{12}HCO_{ad}$, (◆) inverted relative intensity of $^{12}HCO_{ad}$ (1-I($H^{12}CO_{ad}$)), (●)$H^{13}CO_{ad}$, (▼)$^{13}CH_{4,ad}$; during CO methanation upon changing from ^{12}CO to ^{13}CO containing atmosphere (data from Fig. 1). (b) Intensity decay of (▲) $^{12}CO_{ad}$ and (■)$H^{12}CO_{ad}$ on an expanded time scale. Lines: initial slopes of the intensity decay.

In a reaction mechanism where the reaction starts via adsorption of CO, this can be explained by the participation of two competing processes for the $^{12}CO_{ad}$ depletion under reaction conditions, desorption of CO and replacement by adsorbing ^{13}CO and reaction with hydrogen to HCO_{ad}, followed by further reaction to CH_4 and finally desorption. For the adsorbed formyl species (HCO_{ad}), removal is only possible by reaction with H_{ad} to CH_4, and therefore slower.

The above results indicate that CO_{ad} desorption is faster than its further reaction to HCO_{ad} and that reaction of CO_{ad} with hydrogen results in HCO_{ad} species. Though this would agree with a mechanism where HCO_{ad} acts as reaction intermediate, it does not provide final proof for that assignment, at least not for the identification as reaction intermediate in the rate determining reaction pathway. In the latter case, the rate for HCO_{ad} conversion under steady-state reaction conditions should be identical to the reaction rate, i.e., the rate for CH_4 formation under these conditions. This can be tested by determining the initial rate of the $H^{12}CO$ intensity decay (see Figure 28 b). From the initial slope of the intensity-time curve in Fig. 2b, a rate for the HCO_{ad} exchange of $dI/dt = 0.012\ I_{ss}\ s^{-1}$ is obtained, where I_{ss} denotes the intensity under steady-state conditions. For determining the actual reaction rate, the dispersion (fraction of active Ru surface atoms of all Ru atoms) has to be known, the correlation between HCO_{ad} signal intensity and HCO_{ad} coverage, and the HCO_{ad} coverage under steady-state conditions. It is assumed that the intensity is proportional to the HCO_{ad} coverage, which seems to be justified in the limits of low steady-state coverages; the

catalytically active dispersion of the Ru/Al_2O_3 catalyst was determined to 15% (section 3.1). For the steady-state HCO_{ad} coverage, a value of 0.065 monolayers (ML) is estimated. This value, which would be obtained for similar cross-sections of the C-O stretch vibration in HCO_{ad} and CO_{ad}, can certainly only serve as rough estimate. On the other hand, since the purpose of this evaluation is to check whether the HCO_{ad} exchange rate and the reaction (CH_4 formation) rate are of similar order of magnitude, and since the coverage goes linearly into the rate, deviations by small factors are tolerable. With these data, a HCO_{ad} conversion rate of 1.2×10^{-6} $mol\cdot g_{Ru}\cdot s^{-1}$ is calculated, which is rather close to the reaction rate of 3.6×10^{-6} $mol\cdot g_{Ru}\cdot s^{-1}$ determined for CH_4 formation (see section 3.2.2).

For comparison, the rate for the initial intensity decay of the $^{12}CO_{ad}$ related signal is also evaluated (Figure 28 a, b). It yields a rate of $dI/dt = 0.015\ I_{ss}\cdot s^{-1}$. Assuming that under steady-state conditions (p_{CO} = 10 mbar, 190°C) the CO_{ad} coverage is close to saturation including also the HCO_{ad} coverage (this can be derived from the adsorption isotherm, using adsorption characteristics typical for CO/Ru) and that the intensity is proportional to the CO_{ad} coverage, this corresponds to a CO_{ad} exchange rate of 1.5×10^{-5} $mol\cdot g_{Ru}\cdot s^{-1}$. The difference in rate compared to HCO_{ad} exchange results mainly from the much higher steady-state coverage of CO_{ad} compared to HCO_{ad}. As discussed above, the much higher rate for CO_{ad} exchange compared to HCO_{ad} exchange and CH_4 formation is mainly due to the additional fast equilibrium for CO adsorption / desorption.

These results unambiguously prove that adsorbed formyl species indeed act as reaction intermediate in the rate determining majority reaction pathway for CO methanation over a Ru/Al_2O_3 catalyst under present reaction conditions. Its direct spectroscopic identification was possible because of its significant coverage under present steady-state reaction conditions. This indicates that the rate constants for HCO_{ad} formation and its further reaction are of similar order of magnitude. If the latter were much higher, the steady-state HCO_{ad} coverage would be correspondingly lower and vanish below the detection limit of these measurements.

These observations are backed by other studies, where the role of the formyl species was discussed and emphasized as well. Mitchell et al. found that on Ru(001) and at 100 K a HCO_{ad} species was formed during reaction of CO_{ad} with atomic hydrogen [153]. Their study, however, did not allow any conclusions on whether this species

indeed acts as reaction intermediate in the CO methanation reaction under typical reaction conditions. Investigating the CO methanation on different Ni surfaces experimentally and theoretically over a wide (partial) pressure range, Andersson et al. showed that depending on the Ni sites, different surface species are favorable (HCO_{ad} or COH_{ad}) [36]. In all cases, however, H-assisted CO dissociation was always more facile than direct CO dissociation. Comparable results were obtained by Inderwildi et al., who using DFT techniques calculated that on Ru surfaces the methanation reaction proceeds via a H-assisted CO dissociation; reaction via the formyl mechanism was found to be more favorable than a possible CH_x mechanism, where CO is dissociated right in the first step [64].

Interestingly, such a formyl species is not observed on the Ru/zeolite catalyst. While on a first view this may point to a different reaction mechanism, the apparent absence of this species is related to the much higher activity of this catalyst, which is, depending on the reaction conditions, about 10 to 20 times higher than that of the Ru/Al_2O_3 catalyst (see section 3.2.2). If the increase of the rate constant for formyl off-reaction (decomposition) on the Ru/zeolite catalyst, relative to the Ru/Al_2O_3 catalyst, is more pronounced than that for formyl formation, the steady-state coverage of HCO_{ad} will be correspondingly lower on the Ru/zeolite catalyst. In that case, the signal of the formyl species may well be below the detection limit of the DRIFTS measurement.

The stability of the ^{12}C-formate related bands and the additional slow appearance of ^{13}C-formate related bands on both catalysts clearly demonstrates, that these surface formate species represent stable side products in the methanation reaction under present reaction conditions rather than reaction intermediates, in agreement with earlier reports [26;27;30].

3.3.2 Carbon dioxide methanation

In a second, similar set of experiments, possible intermediates and side products of the CO_2 methanation reaction on the Ru/zeolite and a Ru/Al_2O_3 catalyst in CO_2-rich reformate ($CO_2/H_2/N_2$) were investigated. Figure 29 shows a sequence of DRIFT spectra recorded during the CO_2 methanation reaction and the subsequent SSITKA experiment on the Ru/zeolite (a and c) and on the Ru/Al_2O_3 (b and d) catalyst. During 1000 min of reaction, similar bands appear on both catalysts as during CO methanation (see above).

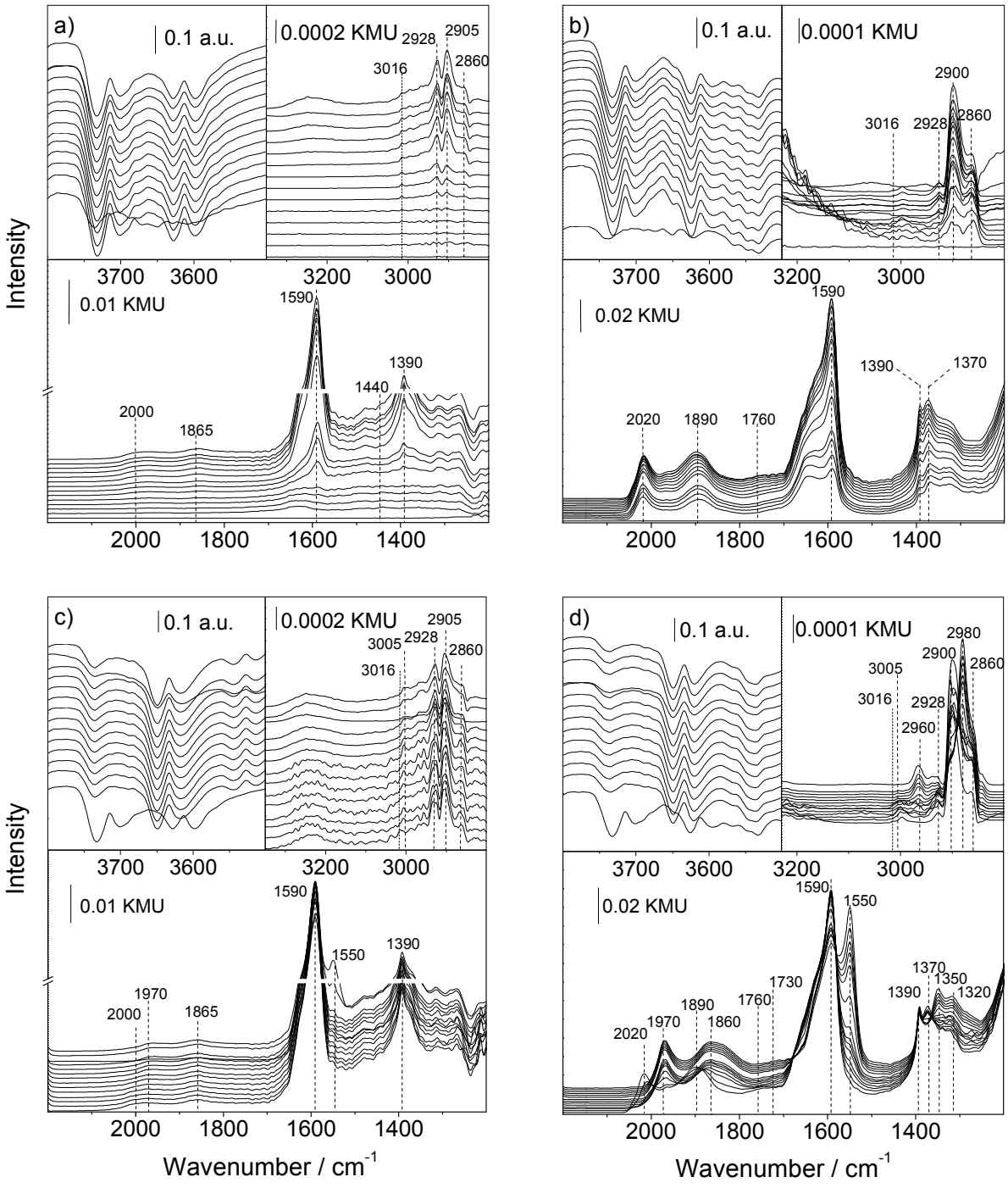

Figure 29: Sequences of DRIFT spectra recorded during 1000 min methanation reaction at 190°C (equilibration of surface species) over the Ru/zeolite (left panels) and the Ru/Al_2O_3 catalysts (right panels) in CO_2-ref (see Table 1 for abbreviations) and subsequent change to $^{13}CO_2$ containing atmosphere. (a), (b): $^{12}CO_2$ containing reaction atmosphere, (c) and (d): $^{13}CO_2$ containing reaction atmosphere; from bottom to top: (a) and (b) 0, 2, 3, 5, 7, 15, 45, 105, 195, 345, 495, 645, 795, 915 min; (c) and (d) 1000, 1, 2, 3, 5, 6, 7, 10, 15, 20. 25, 30, 35, 45 min.

In the following, only the differences to the signals described in the above section will be pointed out.

In the OH region, CO_2-related overtone signals (not marked) appear at 3600, 3640, 3700 and 3740 cm^{-1}, in addition to the OH-related signals in this region, which obscure the OH signals.

The CO region only exhibits two weak signals at ~2000 and 1865 cm^{-1} on the Ru/zeolite catalyst, commonly attributed to linearly adsorbed CO_{ad} on Ru and CO_{ad} in a bridged configuration. They appear after 45 min (Figure 29 a) and reach a steady-state situation after about 100 min. The steady-state intensity is about $^1/_{16}$ of that obtained during CO methanation (Figure 27) (see also section 3.4.1). On the Ru/Al_2O_3 catalyst, in contrast, prominent CO_{ad} signals at 2020 cm^{-1} (linearly CO_{ad}) and 1890 cm^{-1} (bridge bonded CO_{ad}) appear during the first minutes of reaction and increase, until reaching steady-state conditions after 100 min at an intensity which is comparable to that obtained during CO methanation (Figure 27 b). The much lower intensity of the CO_{ad} related bands on the Ru/zeolite catalyst compared to the Ru/Al_2O_3 catalyst agrees perfectly with the much higher CO_2 methanation activity of the latter catalyst under similar reaction conditions reported above (section 3.2). The slight deviation of the CO_{ad} peak positions during CO_2 methanation compared to those observed in the CO methanation experiments discussed above is attributed to the different CO_{ad} coverages in both cases [139].

Main difference in the OCO region compared to the CO methanation experiments described above (Figure 27 a and Figure 27 b) are the much more pronounced formate bands at 1590, 1390 and 1370 on both catalysts in the presence of CO_2, indicating its strong effect on the growth / coverage of surface formates. Similar observations were reported and discussed above (section 3.2.3). Also for reaction of CO_2, HCO_{ad} surface species are formed on the Ru/Al_2O_3 catalyst, as indicated by the small peak at 1760 cm^{-1}. Comparable differences are observed in the CH region, which reveals the typical signals at 3016, 2960, 2928, ~2900, 2860 cm^{-1} as discussed above on both catalysts, but a much more pronounced band at ~2900 cm^{-1} attributed to a C-H vibration of the formate.

Changing from $^{12}CO_2$ to $^{13}CO_2$ (Figure 29 c and Figure 29 d) after 1000 min on stream causes the following main changes in the spectra:

- The CO_{ad} signals at ~2000 cm^{-1} on the Ru/zeolite catalyst and at 2020 and 1890 cm^{-1} on the Ru/Al_2O_3 catalyst are replaced by bands at 1970 and 1860 cm^{-1}, respectively, within the first 3 minutes.

- At the same time, also the $^{12}CH_4$ signal decreases and disappears and the $^{13}CH_4$ related signal grows in and saturates.
- On the Ru/Al_2O_3 catalyst, the band at 1760 cm^{-1} related to HCO_{ad} species decreases and is replaced by a signal at 1730 cm^{-1}, observable as a small shoulder within 3 minutes.
- The formate bands at 1590, 1390 and 1370 cm^{-1} decrease only very little during that time, while new bands of a ^{13}C containing formate at 1550, 1350 and 1320 cm^{-1} grow in and increase rapidly in intensity. Furthermore, a new signal at 2880 cm^{-1} develops, which is attributed to the C-H vibration of the ^{13}C surface formate signal. The ^{12}C signal is still present as a shoulder of the ^{13}C signal.

A quantitative evaluation shows that also in this case the loss of ^{12}C related intensities of CO_{ad} is identical to the gain in ^{13}C-related CO intensity. Furthermore, the quantitative agreement between the $^{12}CO_{ad}$ / $^{13}CO_{ad}$ and the $^{12}CH_{4,ad}$ / $^{13}CH_{4,ad}$ exchange characteristics confirms the earlier proposals that CO_{ad} acts as reaction intermediate in the main reaction pathway for CO_2 methanation on Ru catalysts [71;73]. For the Ru/Al_2O_3 catalyst, comparison of the peak intensity of CO_{ad} derived from CO_2 with that obtained in idealized reformate shows that CO_2 dissociation leads to a CO_{ad} coverage close to saturation. This explains the high CO_2 methanation activity of the Ru/Al_2O_3 catalyst discussed below (see section 3.4). Moreover, the decomposition rate of $^{12}HCO_{ad}$ on the Ru/Al_2O_3 catalyst ($9 \cdot 10^{-7}$ $mol \cdot g_{Ru} \cdot s^{-1}$) is of similar magnitude as that calculated above for CO methanation, which is clear proof that the reaction pathway via formation of CO_{ad} and subsequent formation/off-reaction of HCO_{ad} to CH_4 is the dominant reaction pathway for CO_2 methanation.

In addition, these observations perfectly agree with the mechanism responsible for the high CO selectivity of the Ru/zeolite catalyst during the methanation of reformate gases containing large amounts of CO_2 in addition to CO, which will be discussed later (section 3.4). In that section it is postulated that the high selectivity of the Ru/zeolite catalyst is mainly driven by its inherent low activity for CO_2 dissociation. In contrast, on the Ru/Al_2O_3 catalyst, where CO_2 is readily dissociated to CO_{ad} on free active sites, the CO selectivity is determined by the abundance of free active sites. In that case, high selectivities are only reached for sufficiently high CO partial pressures (low coverage of free active sites) under steady-state conditions. Otherwise, CO_2 is readily dissociated to CO_{ad} on free active sites, leading to a high CO_2 methanation

rate at low CO partial pressures. As already discussed in the introduction, the mechanism for CO_{ad} formation during CO_2 methanation over Group VIII metal supported catalysts is still under debate [71;73-78]. Mostly it is assumed that CO_{ad} is produced via the Reverse Water Gas Shift Reaction (RWGS), either involving the formation and subsequent decomposition of surface formate species [73;76-78;157]. However these studies do not provide a quantitative evaluation of the suggested formate intermediate and neither is it correlated to the CO_{ad} species, which should be connected to the intermediate. Second, a redox mechanism is proposed [80]. As a third alternative, dissociative adsorption of CO_2 was discussed [74]. Under present reaction conditions and for the Ru catalyst investigated, a redox mechanism can be excluded because of the non-reducible support material. Also the formate mechanism is highly unlikely, though it should be favored by the high H_2 partial pressure. It would require a similarly rapid decrease of the formate related bands, at least of those attributed to one surface formate species, upon changing from $^{12}CO_2$ to $^{13}CO_2$. This is in contrast to the experimental observations, which show a very slow decrease of the $H^{12}COO$ related bands only, in contrast to the rapid exchange of the CO_{ad} related bands. Instead, bands related to ^{13}C-containing formate species grow in additionally, indicating that the (total) surface formate coverage has not reached steady-state conditions after 1000 min on stream. Hence, under present experimental conditions, CO_{ad} formation via formate formation/decomposition can not represent the dominant reaction pathway, although contributions from this reaction pathway as minority pathway can not be ruled out. In consequence, no evidence is provided for CO_{ad} formation via the RWGS reaction in the CO_2 methanation reaction, at least not in the main reaction pathway, and therefore propose that under present reaction conditions (high H_2 excess, atmospheric pressure) CO_2 methanation on Ru catalysts proceeds via dissociative adsorption of CO_2 to form CO_{ad} and O_{ad}, which subsequently reacts to CH_4 and H_2O. As the results and observations described above hold true for both catalysts, CO_2 adsorbs dissociatively on the Ru/Al_2O_3 and on the Ru/zeolite catalyst.

3.3.3 Conclusion

Based on time resolved DRIFTS measurements during the methanation of CO and CO_2 over two supported Ru catalyst, a Ru/zeolite catalyst and a Ru/Al_2O_3 catalyst, and employing SSITKA type exchange techniques, adsorbed formyl species with a characteristic band at 1760 cm^{-1} were unambiguously identified as reaction

intermediate for CO methanation in a $CO/H_2/N_2$ mixture on the Ru/Al_2O_3 catalyst under reaction conditions typical for reformate purification. The identification as reaction intermediate rather than a spectator type reaction side product is based on its formation/reaction rate under steady-state conditions, which is of similar order of magnitude as the overall ration rate (CH_4 formation rate). For the Ru/zeolite catalyst, the same reaction mechanism is proposed. The absence of a similar band on the Ru/zeolite catalyst is attributed to a much lower steady-state coverage of that species, which is rationalized by the much higher reaction rate on that catalyst. Similar experiments performed for the CO_2 methanation reaction revealed that under present reaction conditions the reaction proceeds via formation and further reaction of CO_{ad}. This, however, can not be formed via a formate based reverse water gas shift reaction, at least not as main reaction pathway, since the decomposition of surface formate species is too slow compared to the CO_{ad} exchange rate. Since a redox RWGS mechanism involving reaction with the catalyst is equally unlikely for the present catalysts, it is suggested that under present reaction conditions CO_{ad} is formed via dissociative adsorption of CO_2 to form CO_{ad} and O_{ad}, which subsequently reacts to CH_4 and H_2O.

3.4 What drives the selectivity for CO methanation in the methanation of CO_2-rich refomate gases on supported Ru catalysts?

The previous sections gave insight into the general behavior and characteristics of the two Ru supported catalysts, and elucidated the reaction intermediate of the methanation reaction. The following section will show the differences in the selectivity mechanisms, which apply for the CO selectivity of the Ru catalysts. The effect of the CO content on the adsorption and reaction behavior on a Ru/zeolite and a Ru/Al_2O_3 catalyst will be investigated in a combined kinetic and *in situ* IR spectroscopic study on, focusing on correlations between CO_{ad} coverage and selectivity. The measurements were performed in a number of different idealized (H_2/CO) and semi-realistic (H_2/CO/CO_2) reaction atmospheres, decreasing the CO content to as low as 100 ppm. The temporal evolution of the adsorbed surface species during the methanation reaction in different reaction atmospheres, characterized by time-resolved *in situ* IR measurements, is described in section 3.4.1. In combination, these measurements allow me to not only to determine the steady-state CO_{ad} coverages in different reaction atmospheres, but also to qualitatively assess the contribution from CO_2 decomposition to the CO_{ad} signal in the experiments performed under semi-realistic conditions. The influence of the CO content on the CO methanation activity and on the selectivity for CO methanation is topic of the following section 3.4.2. The resulting correlations between CO_{ad} coverage and the selectivity for CO methanation as well as consequences on the molecular scale mechanism responsible for the selectivity are discussed. Finally, it will be briefly commented on consequences of these findings for technical applications of the reaction.

All results of the following sections were published in Applied Catalysis A: 391 (2011) 325: *What drives the selectivity for CO methanation in the methanation of CO_2-rich refomate gases on supported Ru catalysts.*

3.4.1 In situ DRIFTS measurements

The interaction of the different reaction atmospheres with the two catalysts and the resulting adlayer build-up were characterized by sequences of *in situ* DRIFTS measurements. These were preformed in different reaction atmospheres, including

semi-realistic atmospheres with different CO contents (SR-ref 100, SR-ref 1000, SR-ref 6000) and, for comparison, idealized (CO_2-free) (ID-ref 100 and ID-ref 1000) as well as (CO-free) CO_2 reformate (CO_2-ref) (seeTable 1).

The spectra of the measurements in ID-ref 1000 and in SR-ref 6000 are not shown here because they largely resemble the other data sets, but the final spectra and the intensities of the CO_{ad} bands are included in Figure 30 and Figure 33.

The characteristic bands arising from the interaction with the respective reaction atmospheres are evident form the spectra in Figure 30, which were recorded after 1000 min on stream. The spectra are split into 3 frequency ranges, the region of the OH (4000-3400 cm^{-1}, top left) and CH_x (3300-2800 cm^{-1}, top right) stretch vibrations in the top panels, respectively, and the spectral range between 2200 and 800 cm^{-1} including the CO stretch (2200-1900 cm^{-1}) and the OCO bending (1600-800 cm^{-1}) vibrations in the bottom panel. The spectra in the OH region are shown as raw data, since the significant change in the background intensity in this region with time do no allow me to determine a proper background signal for the background subtraction. The assignments of the main bands (see dashed lines) will be briefly summarized here, a detailed discussion was given in the section 3.2.3.

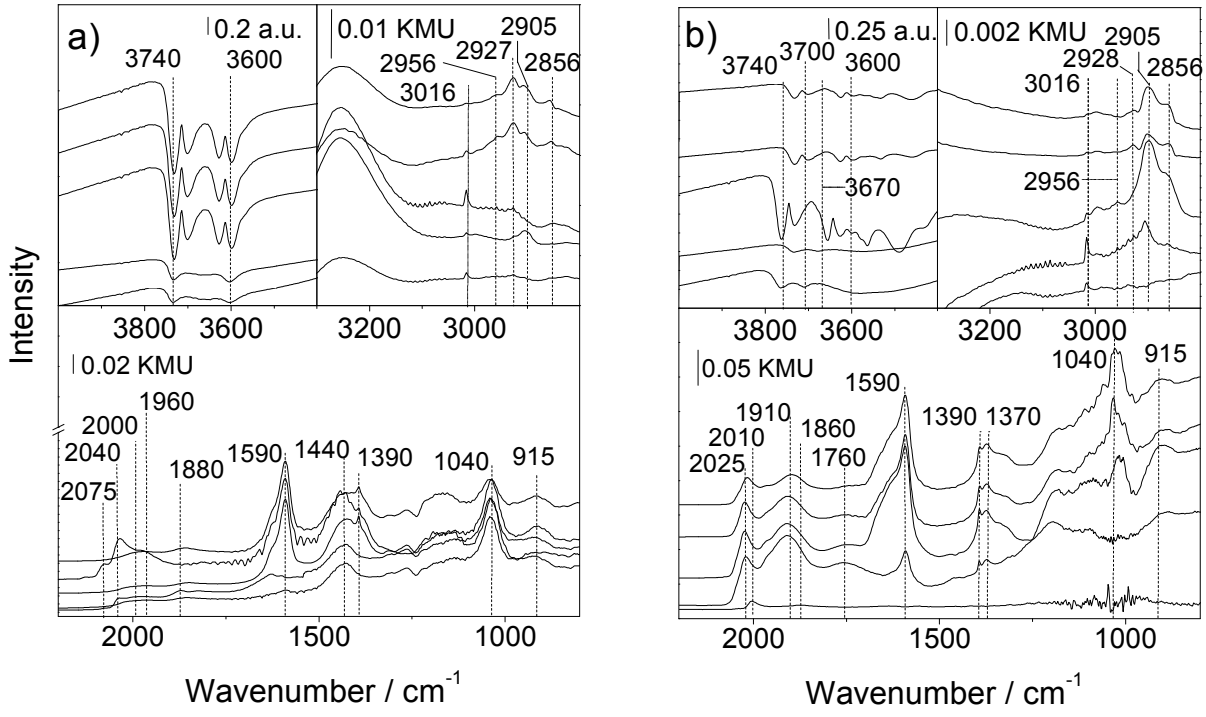

Figure 30: Sequences of DRIFT spectra recorded after 1000 min methanation reaction at 190°C over the Ru/zeolite (a) and the Ru/Al_2O_3 (b) catalysts in different reaction atmospheres. From bottom to top: ID-ref 100, ID-ref 1000, SR-ref 100, SR-ref 1000, SR-ref 6000, CO_2-ref (see Table 1 for abbreviations)

On both catalysts, characteristic signals in the CO_{ad} region at ~2000 / 2040 cm^{-1} and 1960 / ~1880 cm^{-1} on the Ru/zeolite, depending on the CO content in the gas mixture, and at ~2010 / 2025 cm^{-1} and ~1860 / 1910 cm^{-1} on the Ru/Al_2O_3 catalyst are found, which are generally attributed to CO adsorbed linearly or in a bridged configuration on Ru [31;65;79;132-134;136-138;151]. A signal at 2075 cm^{-1} on the Ru/zeolite is usually assigned to CO adsorbed on Ru^{n+} [65;152]. The exact frequencies vary slightly with reaction conditions.

The OH region exhibits two peaks at 3740 and 3600 cm^{-1} on the Ru/zeolite catalyst, which are related to structural silanol and/or isolated OH_{ad} groups on the support [141;142]. After 1000 min of reaction on the Ru/Al_2O_3 catalyst, two additional OH_{ad} signals appear at 3700, 3670 cm^{-1}, which were attributed to OH_{ad} groups on different Al_2O_3 crystal facets [141]. Isolated OH groups are observed on this catalyst at 3740 cm^{-1} again. In CO_2 containing reformates, CO_2-related overtone signals (not marked) appear at 3600, 3640, 3700 and 3740 cm^{-1}, in addition to the OH-related signals in this region.

The CH_x spectral region shows the typical $CH_{x,ad}$ signals at 3016, 2956, 2928, and 2856 cm^{-1}, arising from CH_4, $CH_{3,ad}$, and the symmetric and asymmetric $CH_{2,ad}$ vibrations on the two catalysts [27;65;79]. A shoulder at ~2905 cm^{-1} was assigned to the CH vibration of a surface formate [26;30]. Depending on the catalyst and the reaction conditions, only some of the bands are resolved. At higher conversions, all of these bands are visible.

In the OCO region, bands at 1590, 1440, 1390, 1040 and 915 cm^{-1} on the Ru/Zeolite catalyst were assigned to surface formates (1590 and 1390 cm^{-1}), carbonates (1440 cm^{-1}), possibly methoxy (1040 cm^{-1}) species and CH_2 vibrations (915 cm^{-1}) resulting from chain growth. On the Ru/Al_2O_3 catalyst, the corresponding bands appear at 1590, 1390, 1370 (additional formate vibration), 1040 and 915 cm^{-1}, except for the carbonate band, which is not formed on this catalyst (see section 3.2).

Sequences of DRIFT spectra, recorded during 1000 min reaction on the Ru/zeolite and the Ru/Al_2O_3 catalyst in different reaction atmospheres, are shown in Figure 31 and Figure 32 (Figure 31: (a) Ru/zeolite and (b) Ru/Al_2O_3: ID-ref 100, (c) Ru/zeolite and (d) Ru/Al_2O_3: SR-ref 100; Figure 32: (a) Ru/zeolite and (b) Ru/Al_2O_3: CO_2–ref.

Reaction in ID-ref 100 (100 ppm CO): First the build-up and evolution of the different surface species on both catalysts in ID-ref 100 were followed (Figure 31). On both catalysts, CO_{ad} bands appear at 2000 cm^{-1} / 1880 cm^{-1} on the Ru/zeolite and at 2010 cm^{-1} and 1860 cm^{-1} on the Ru/Al_2O_3 catalyst after ~2 and ~1 min, respectively. A dynamic equilibrium is reached after 100 min. The CO_{ad} signals appear at a significantly lower wavenumber than reported in section 3.2.3 with a higher CO concentration (6000 ppm CO), which is explained by the lower CO_{ad} coverage under present conditions [139]. Interestingly, no evidence is found for bands at 2075 cm^{-1} or 2135 cm^{-1}, which were attributed to CO adsorbed on oxidized Ru^{n+} or coadsorbed with O_{ad} on Ru [132;134;135;138], on either of the two catalysts, in contrast to previous findings discussed above for the Ru/zeolite catalyst. This apparent discrepancy can be explained by the much lower CO partial pressure in the present measurements as compared to the previous ones. Also for 0.6% CO in idealized reformate it took about 100 min, until a small shoulder of the CO_{ad} signal at 2075 cm^{-1} was detected (see section 3.2.3).

The two bands at 3740 and 3600 cm^{-1} on the Ru/zeolite catalyst related to structural silanol and isolated OH_{ad} groups on the support [141;142] are visible already at the beginning of the reaction and do not change significantly in intensity during the reaction. On the Ru/Al_2O_3 catalyst, additional OH_{ad} signals, besides the feature at 3740 cm^{-1}, can be observed at 3680, 3640, 3620, 3530 and 3460 cm^{-1} at the beginning and during the reaction, which were previously assigned to OH groups on different Al_2O_3 facets [141]. With ongoing reaction, the intensity of the peak at 3740 and 3680 cm^{-1}, attributed to terminal and isolated OH groups, remains constant, whereas that of the other four signals decreases. This can either result from a reconstruction of the Al_2O_3 crystallites, induced by the loss of the OH species, or it simply reflects the loss of OH species due to reaction with hydrogen and subsequent desorption of water.

In the OCO region, bands at 1590, 1440, 1040 and 915 cm^{-1}, which were attributed to surface formates, carbonates, methoxy and CH_2 vibrations, appear after about 100 min reaction on the Ru/Zeolite catalyst. On the Ru/Al_2O_3 catalyst, the respective bands start growing in after about 45 min, except for the surface carbonate band, which is not observed at all on this catalyst.

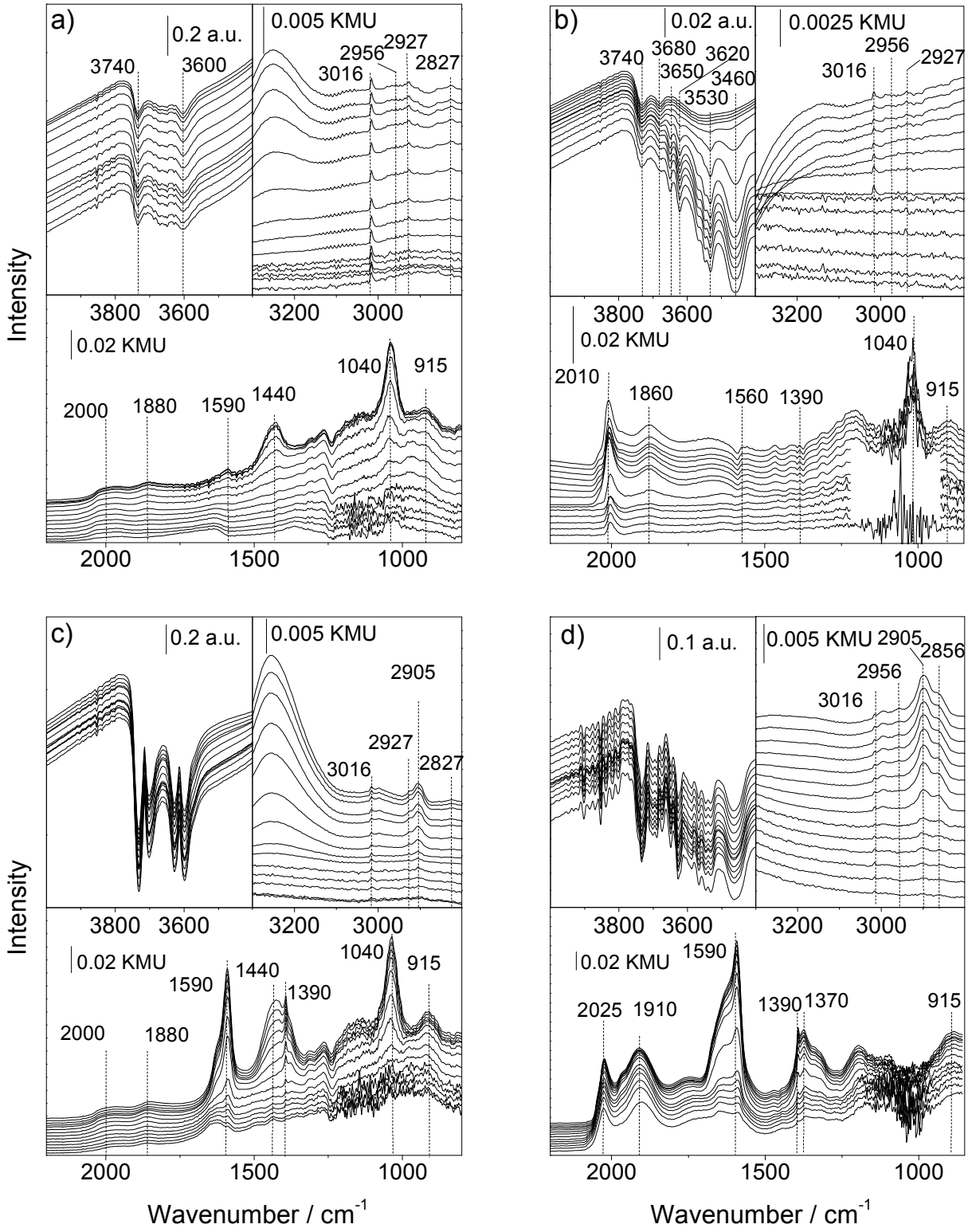

Figure 31: Sequences of DRIFT spectra recorded during 1000 min methanation reaction at 190°C over the Ru/zeolite ((a),(c)) and the Ru/Al_2O_3 ((b),)(d)) catalysts in reaction gases with low CO content (100 ppm); (a),(b) ID-ref 100 and (c),(d) SR-ref 100 (see Table 1 for abbreviations). The spectra were recorded after 1, 2, 3, 5, 7, 15, 35, 105, 195, 345, 495, 645, 795, 945 min reaction time (from bottom to top), upper left panel: O-H band region, upper right panel: C-H region, bottom panel: CO and OCO band region.

Depending on the gas mixture the formate band is shifted to 1560 cm^{-1}. Additionally, a signal at 1390 cm^{-1} is observed, which is attributed to an additional formate vibration. The bands steadily increase in intensity and do not reach a steady-state situation after 1000 min, similar to previous observations in idealized and (H_2O-rich) semi-realistic atmospheres (section 3.2.3). An additional band at 1760 cm-1 is related to adsorbed HCO species, which was proposed to play a major role as reaction intermediate for CO methanation (see section 3.3). In the CH_x spectral region (Figure 31 a and b), the typical $CH_{x,ad}$ signals at 3016, 2956, 2927, and 2827 cm^{-1} (Ru/zeolite) and 3016, 2956 and 2927 cm^{-1} (Ru/Al_2O_3) (assignment see above) start to grow in after about fifteen minutes reaction time. They increase further until saturating after 340 and 1000 min reaction on the Ru/Al_2O_3 and Ru/zeolite catalyst, respectively. Hence, in contrast to the surface formates/carbonates, these species do reach a steady-state coverage.

Comparing the reaction in ID-ref 100 on Ru/zeolite and Ru/Al_2O_3 catalysts (Figure 31 a and b)), no major differences are observed in the type of adsorbed surface species. The situation is different, however, when comparing the temporal evolution and peak intensities of the adsorbed CO. Here the intensity of the CO_{ad} species is much lower on the Ru/zeolite compared to the Ru/Al_2O_3 catalyst, and furthermore the intensities are much lower than those observed previously (section 3.2.3) at higher CO partial pressure. This will be discussed in more detail below.

Reaction in SR-ref 100 (100 ppm CO) and in CO_2-ref: Similar DRIFTS measurements were performed in these CO_2 containing atmospheres (see Table 1) to identify the influence of CO_2 on the CO_{ad} formation, which has been shown to be an intermediate in the CO_2 methanation (see section 3.3). The general characteristics of the resulting spectra (Figure 31 c and d and Figure 32 a and b) are rather similar to those obtained in ID-ref 100 (Figure 31 a and b). The addition of CO_2 results further in an increase of the formate and carbonate related signals and in overtone vibration in the OH region. Most obvious are differences in the CO_{ad} band intensities in the different atmospheres and in their temporal evolution. Therefore, the band intensities of linearly adsorbed CO_{ad} species on Ru, are plotted for different reaction atmospheres in Figure 33 a (Ru/zeolite catalyst) and Figure 33 b (Ru/Al_2O_3 catalyst), respectively, as a function of the time on stream.

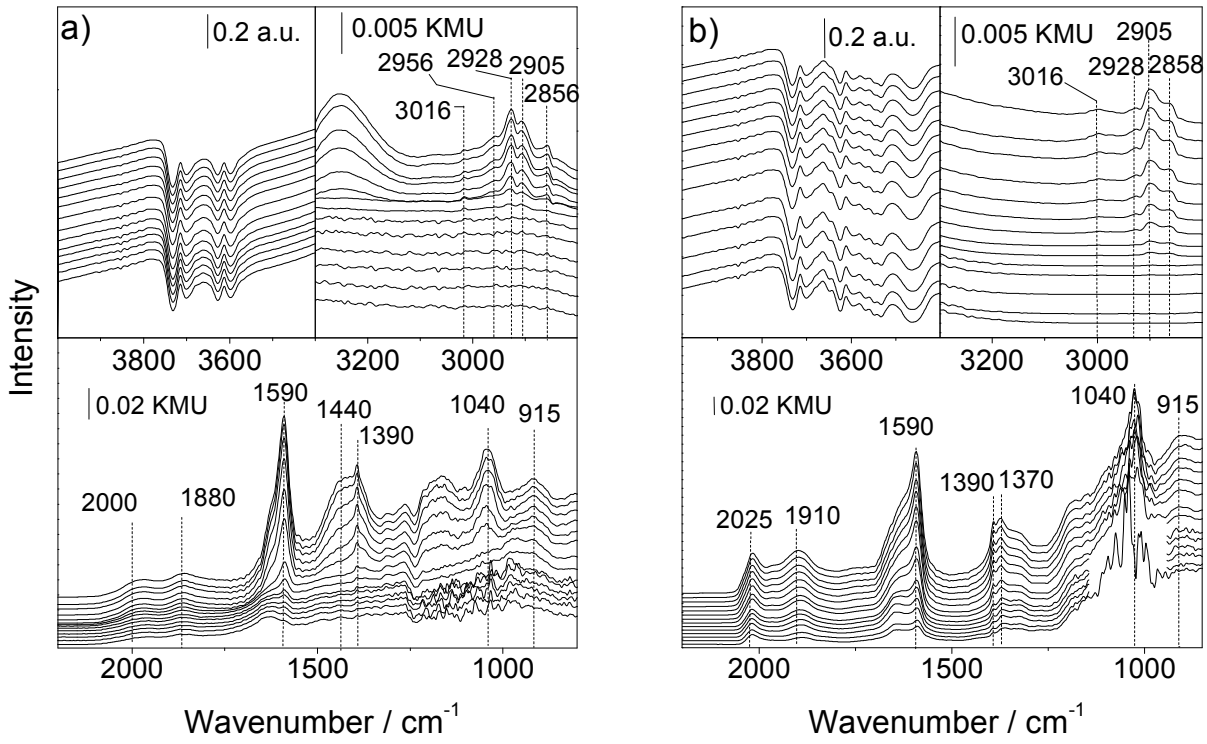

Figure 32: Sequences of DRIFT spectra recorded during 1000 min methanation reaction at 190°C over the Ru/zeolite (a) and the Ru/Al_2O_3 (b) catalysts in CO_2-ref (see Table 1 for abbreviations). The spectra were recorded after 1, 2, 3, 5, 7, 15, 35, 105, 195, 345, 495, 645, 795, 945 min reaction time (from bottom to top), upper left panel: O-H band region, upper right panel: C-H region, bottom panel: CO and OCO band region.

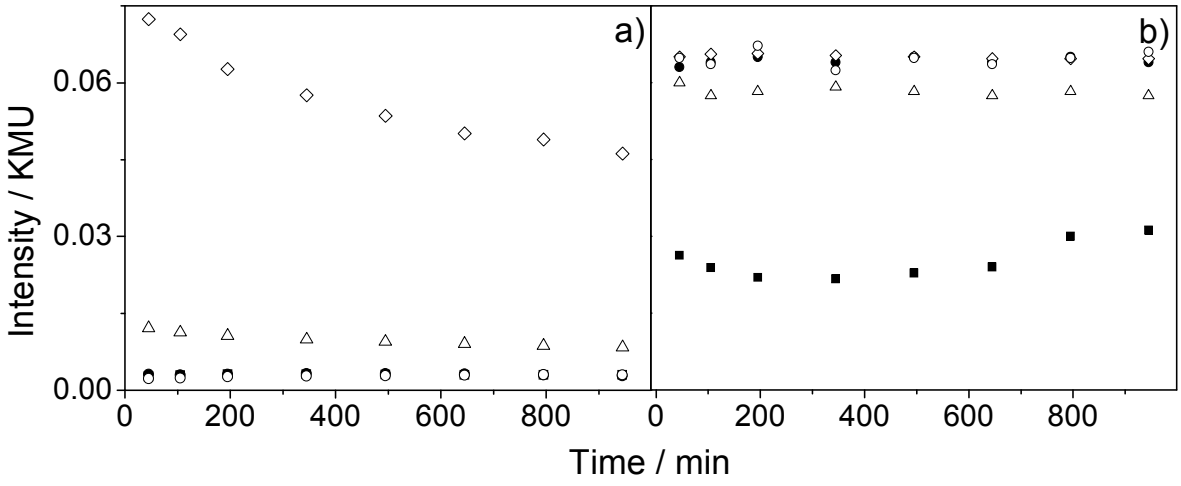

Figure 33: Time evolution of the CO_{ad} band intensities (peak heights) obtained during reaction on the Ru/zeolite (a) and the Ru/Al_2O_3 (b) catalysts in different reaction atmospheres: ■: ID-ref 100; △: ID-ref 1000; ●: SR-ref 100; ◇: SR-ref 6000 ; ○: CO_2-ref (see Table 1 for abbreviations).

On the Ru/Al_2O_3 catalyst, the characteristic findings and differences between the various reaction atmospheres are:

(I) In all cases, the final CO_{ad} band intensities are reached rather quickly, within the first 100 min, except for reaction in ID-ref 100 (100 ppm CO), where the intensity increases slowly after 500 min and reaches steady-state conditions after 1000 min.

(II) The CO_{ad} band intensity is significantly higher (~2.2 fold) in SR-ref 100 than in ID-ref 100, pointing to additional CO_{ad} formation from CO_2 adsorption in the former case. The higher CO_{ad} coverage shifts the peaks of the respective signals to 2025 and 1910 cm^{-1} (ID-ref 100: 2010 and 1860 cm^{-1}).

(III) On the other hand, there is little difference between the CO_{ad} band intensities in SR-ref 100 and that obtained in SR-ref 6000 on the same catalyst. Hence, in semi-realistic reformate, the CO_{ad} coverage does not depend on the CO concentration in the range covered in the present study; CO_2 decomposition to CO_{ad} leads to a surface coverage close to saturation.

(IV) Correspondingly, in (CO-free) CO_2 reformate (CO_2-ref), the CO_{ad} signal intensity reaches a similar value as in semi-realistic reaction atmosphere (100 ppm or 6000 ppm CO).

(V) In ID-ref 1000, the CO_{ad} coverage is significantly higher (about double) than in ID-ref 100, but does not yet reach saturation. The CO_{ad} band intensity is ~90% of the CO_{ad} signal intensity obtained in semi-realistic reaction atmosphere (100 ppm or 6000 ppm CO).

On the Ru/zeolite catalyst, the situation is distinctly different. Here the main results are:

(I) In reaction atmospheres with low CO contents (ID-ref 100, SR-ref 100, and CO_2-ref (CO-free)), the final intensities are reached quickly, within the first 100 min. For higher CO contents (ID-ref 1000 and SR-ref 6000), the CO_{ad} intensity passes through an initial maximum and then decays with time (23% for ID-ref 1000, 20% for SR-ref 6000 over the full time on stream).

(II) The final CO_{ad} band intensities are significantly lower in reaction atmospheres with a low CO content than SR-ref 6000. Both in SR-ref 100 and in ID-ref 100, the CO_{ad} band intensity is only ~6% of that obtained in SR-ref 6000. Hence, in this case, the presence of a large CO_2 excess does not increase the low steady-state CO_{ad} coverage.

(III) Correspondingly, the CO_{ad} coverage and band intensity obtained in (CO-free) CO_2-ref are also low and similar to those obtained in ID-ref 100 and SR-ref 100 on the same catalyst.

(IV) Even at 1000 ppm CO concentration, the CO coverage is far from saturation. The CO_{ad} band intensity obtained in ID-ref 1000 reaches $^1/_6$ of the value of the CO_{ad} band intensity obtained in SR-ref 6000, where the latter is again assumed to reflect CO_{ad} saturation.

The most important observations are that i) the presence of CO_2 in the reformate gases (CO_2-ref, SR-ref 100) increases the CO_{ad} band intensity and hence the CO_{ad} coverage significantly on the Ru/Al_2O_3 catalyst compared to the ID-ref 100 (see Figure 33 b), while on the Ru/zeolite catalyst the presence of CO_2 has essentially no effect on the CO_{ad} coverage, and that ii) in reaction atmospheres with low CO content (ID-ref 100) the CO_{ad} coverage is much lower on the Ru/zeolite catalyst than on the Ru/Al_2O_3 catalyst.

Considering that on the Ru/Al_2O_3 catalyst the CO_{ad} level in SR-ref 100 is about equally high as in SR-ref 6000, which in turn is likely to represent the CO_{ad} saturation coverage, the first point implies that on this catalyst CO_2 decomposition is facile on sites which are active also for CO adsorption. In SR-ref 100, the two pathways for CO_{ad} formation, CO adsorption and CO_2 decomposition, are sufficiently fast to reach the CO_{ad} coverage close to saturation under present reaction conditions (190°C reaction temperature). Facile decomposition of CO_2 to CO_{ad} on this catalyst is supported by the fact that also in (CO-free) CO_2-ref a CO_{ad} value close to saturation coverage is reached. In contrast, on the Ru/zeolite catalyst, the CO_{ad} band intensities in SR-ref 100 and in (CO-free) CO_2-ref are essentially identical to that obtained in ID-ref 100. Hence, on this catalyst CO_2 decomposition to CO_{ad} occurs only at very low rates even at very low CO partial pressures, in CO-free CO_2-ref and in SR-ref 100. This indicates that on the very small Ru NPs in this catalyst the CO_{ad} formation from CO_2 is inherently slow and not just hindered by a blocking CO adlayer. A more detailed discussion will be given in the next section.

3.4.2 Kinetic measurements

Figure 34 illustrates the temporal evolution of the Ru mass normalized activities and of the selectivities for CO methanation obtained over the two catalysts at 190°C in semi-realistic reaction atmospheres with different CO concentrations. The activities are based on the CO consumption, the selectivity for CO methanation is calculated from the ratio between CO consumption and CH_4 formation. Table 5 summarizes the reaction rates and the selectivities of both catalysts under these reaction conditions. In all cases, the Ru/zeolite catalyst is significantly more active, by factors between 6 and 20, than the Ru/Al_2O_3 catalyst, and a CO selectivity of 100% is maintained (all methane formed results from CO methanation), while for the Ru/Al_2O_3 catalyst the selectivity depends on the composition of the reaction gas.

Catalyst	Ru/zeolite		Ru/Al_2O_3	
Reaction gas	Activity$\times 10^{-6}$/ $mol \cdot s^{-1} \cdot g_{Ru}^{-1}$	Selectivity / %	Activity$\times 10^{-6}$/ $mol \cdot s^{-1} \cdot g_{Ru}^{-1}$	Selectivity / %
Low-CO semi-realistic reformate (100 ppm CO)-SR-ref 100	78	100	10	42
Semi-realistic reformate (1000 ppm CO)-SR-ref 1000	91	100	22,5	86
Semi-realistic reformate (3000 ppm CO)-SR-ref 3000	78	100	9,2	100
Semi-realistic reformate (6000 ppm CO)-SR-ref 6000	67/62	100	3,9	100

Table 5: Ru mass normalized activities for CH_4 formation (maximum/steady-state activity if applicable) and selectivities for CO methanation in the selective CO methanation reaction over the two Ru catalysts at 190°C.

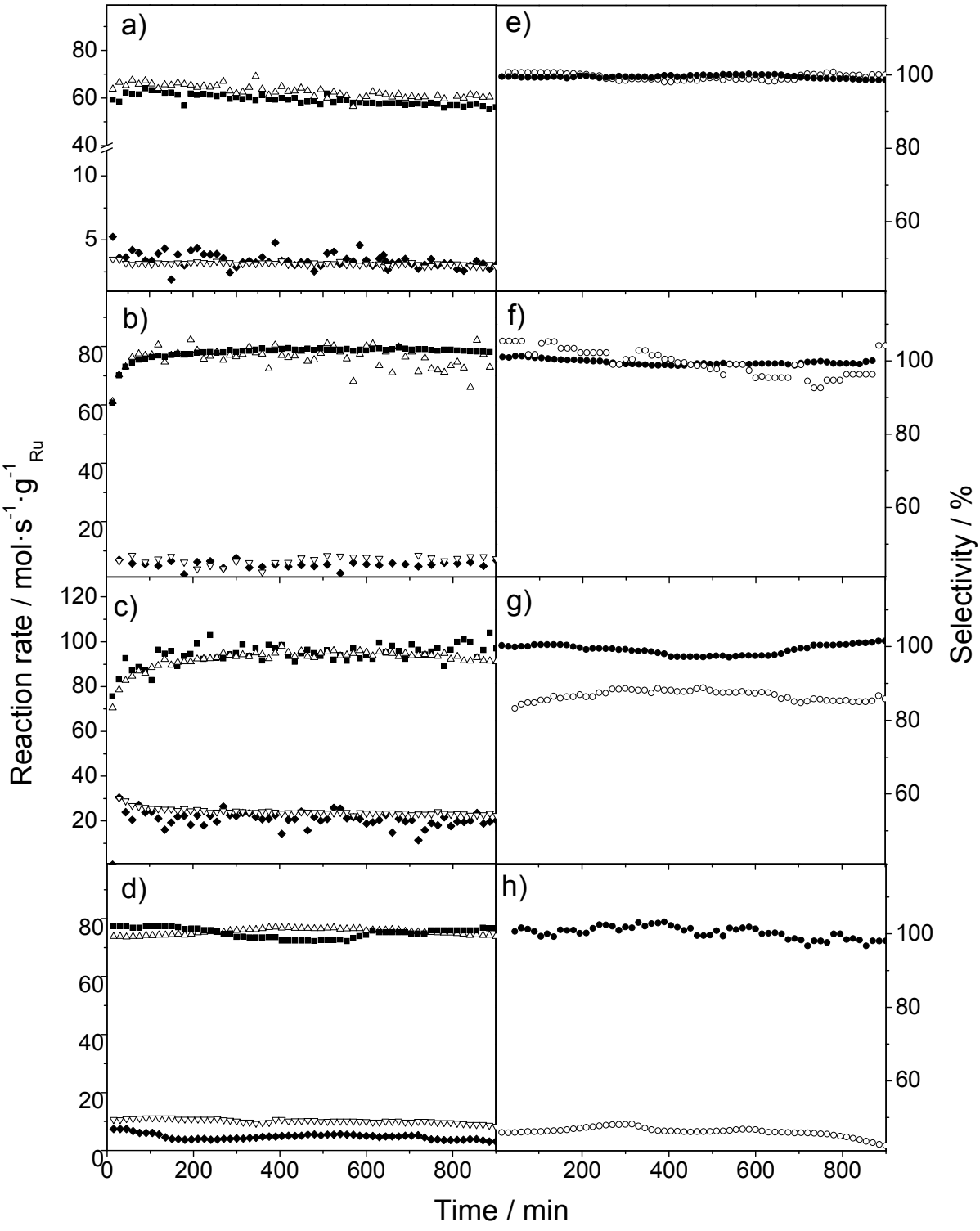

Figure 34: Reaction rates (left panels) and selectivities (right panels) obtained for reaction over the Ru/zeolite and the Ru/Al_2O_3 catalysts, both diluted with SiO_2 to achieve differential conditions, in different semi-realistic reaction atmospheres (x % CO, 2.8 % N_2, 15.5 % CO_2, rest H_2). CO reaction rate: (■) Ru/zeolite, (◆) Ru/Al_2O_3; CH_4 formation rate: (△) Ru/zeolite, (▽) Ru/Al_2O_3; selectivity: (●) Ru/zeolite , (○) Ru/Al_2O_3; (a), (e): x = 6000 ppm, (b), (f): x = 3000 ppm, (c),(g): x = 1000 ppm, (d), (h): x = 100 ppm.

Comparing the reaction rates and selectivity of the two catalysts at 'normal' reaction conditions, i.e., in SR-ref 6000 at 190°C, the catalysts exhibit initial reaction rates of 63×10^{-6} mol·s^{-1}·g_{Ru}^{-1} (Ru/zeolite) and 3.4×10^{-6} mol·s^{-1}·g_{Ru}^{-1} (Ru/Al_2O_3). The Ru/zeolite catalyst shows a slight initial activation for about 50 min (maximum rate 67×10^{-6} mol·s^{-1}·g_{Ru}^{-1}), followed by a slow decay by ~8% of its highest rate over the remaining time on stream, reaching steady-state conditions at a rate of 65×10^{-6} mol·s^{-1}·g^{-1}_{Ru} and a selectivity of 100%. In contrast, on the Ru/Al_2O_3 catalyst, the reaction is essentially stable over the entire time on stream of 1000 min, with a reaction rate of $3.9\cdot10^{-6}$ mol·s^{-1}·g^{-1}_{Ru} and a selectivity of 100%. These results agree very well with previous findings (sections 3.2.1 and 3.2.2).

Using a lower CO concentration of 3000 ppm (ID-ref 3000), while leaving the other components constant, the initial activation of the Ru/zeolite catalyst is more pronounced; starting from an initial rate of 60×10^{-6} mol·s^{-1}·g^{-1}_{Ru}, it reaches a maximum rate of 78×10^{-6} mol·s^{-1}·g^{-1}_{Ru} after ~50 min. Interestingly, the activity does not decrease subsequently as described in the measurement above. The absence of an apparent deactivation is explained by counteracting contributions from catalyst activation and deactivation. (Note that the steady-state CO_{ad} coverage decreases with time in both SR-ref 6000 and in ID-ref 1000.) The higher activity under these conditions, as compared to reaction in SR-ref 6000, is attributed to a lower CO_{ad} coverage, which leaves more sites for H_2 adsorption. Assuming a Langmuir-Hinshelwood reaction mechanism, this should increase the activity. For the Ru/Al_2O_3 catalyst, qualitatively similar, but even more pronounced trends in the activity (increasing rate with lower CO content) are observed, pointing to a similar reaction mechanism. The present results and conclusions agree very well with the negative reaction order measured for CO under comparable reaction conditions on both catalysts (Ru/Al_2O_3: α_{CO} = -0.5, Ru/zeolite: α_{CO} = -0.7 (section 3.2.2)). Only for the lowest CO concentration (100 ppm CO), the activity decreases again on both catalysts. At this point (at ~1000 ppm), the reaction has apparently changed from H_{ad} limited to CO_{ad} limited, which now results in an opposite effect upon further lowering of the CO partial pressure.

The selectivity of the Ru/zeolite catalyst remains constant at 100%, independent of the CO concentration in the reformate. On the Ru/Al_2O_3 catalyst, it is around 100% at the higher CO concentrations (3000 ppm, 6000 ppm CO), but decreases to 85% for reaction with 1000 ppm CO in the reformate and even to only 42% for reaction in low-

CO semi-realistic reformate (SR-ref 100). Hence, the difference in selectivities observed in integral measurements on the two catalyst, with complete removal of CO at negligible CO_2 conversion on the Ru/zeolite catalyst compared to only partial CO removal (remaining CO content 3000 ppm CO) at the onset of CO_2 conversion or sizable CO_2 conversion (selectivity 48%) at complete CO removal on the Ru/Al_2O_3 catalyst (see section 3.2.1), is reflected also by the different reaction characteristics under differential reaction conditions at low CO contents.

The significantly higher activity of the Ru/zeolite catalyst compared to the Ru/Al_2O_3 catalyst in SR-ref 6000 was already discussed above. Differences in the morphology and chemical properties of the support such as pore structure, support acidity (metal support effects) and BET surface area were held responsible for the significantly higher activity of the Ru/zeolite catalyst. These effects are likely to be active also at lower CO contents. Obviously, these explanations are rather qualitative, a more quantitative molecular scale explanation, which would be desirable, is still missing.

The selectivity for CO methanation in the selective methanation reaction is commonly attributed to a blocking of the active catalyst surface by CO_{ad}, due to the higher adsorption energy of CO compared to CO_2 [49;50]. The authors claimed that CO_2 methanation sets in only if there is not sufficient CO in the gas phase to block all active surface sites CO adsorption. In that case, the adsorption of CO_2 and its subsequent dissociation and methanation would become active. In a more detailed picture, one has to consider that complete blocking of the surface by CO_{ad} would not only inhibit dissociative CO_2 adsorption, but also H_2 adsorption, which is pre-requisite for the methanation of CO. Hence, under reaction conditions, the surface can not be fully blocked by CO_{ad}, but must leave open sites for dissociative H_2 adsorption. In that picture, the inhibition of dissociative CO_2 adsorption and hence the selectivity for CO methanation results from the higher adsorption energy of hydrogen (dissociative adsorption) compared to CO_2 (molecular adsorption) and the much higher barrier for $CO_{2,ad}$ dissociation [37] than for dissociative H_2 adsorption. (On most surfaces, the latter barrier is negligible [158].) In that case, adsorption of CO_2 or H_2 on empty surface sites will be determined by the respective partial pressures, but the lifetime on the surface will be much shorter for $CO_{2,ad}$ than for H_{ad}. As long as the CO_2 steady-state coverage is sufficiently low, dissociation of $CO_{2,ad}$ (and the subsequent methanation of the resulting CO_{ad}) will effectively be inhibited, while dissociative adsorption of H_2 to H_{ad} and its subsequent reaction with CO_{ad} will already be active.

This reaction scheme agrees fully with the findings for the Ru/Al_2O_3 catalyst, where CO_2 methanation sets in as soon as the steady-state CO_{ad} coverage (from CO adsorption) decreases below a critical value. At that point, CO_2 dissociation and subsequent methanation set in, and the selectivity decreases. Most clearly, this is demonstrated by methanation of (CO-free) CO_2-ref, which results in a rapid build-up of a CO adlayer, close to or at CO_{ad} saturation under present reaction conditions. But also in SR-ref 100 or SR-ref 1000, the critical CO_{ad} coverage is not reached any more, and CO_2 methanation is observed. Hence, on these Ru NPs, CO_2 dissociation on the adsorbate free Ru NPs is facile.

The situation is very different for the Ru/zeolite catalyst. On this catalyst, the selectivity for CO_{ad} methanation remains high, at essentially 100%, even at very low CO concentrations and at very low CO_{ad} coverages under steady-state conditions (6% of the saturation CO_{ad} band intensity in SR-ref 100). This indicates already that surface blocking can not be the main reason for the high selectivity. Together with the observation of a very low activity for CO_2 dissociation in (CO-free) CO_2-ref (see section 3.1), this provides clear proof that on this catalyst the high selectivity for CO methanation does not originate from blocking of surface sites by adsorbed CO, but rather from an inherent, low activity of this catalyst for dissociative adsorption of CO_2. This conclusion is supported also by the much lower steady-state CO_{ad} coverage at 100 ppm CO content on the Ru/zeolite catalyst, with ~6% of the saturation CO_{ad} band intensity compared to ~45% on the Ru/Al_2O_3 catalyst (ID-ref 100), which points to a distinct decrease of the CO adsorption energy and hence to a weakening of the CO_{ad}-substrate bond on the very small Ru NPs compared to the larger Ru NPs on the Ru/Al_2O_3 catalyst. According to the Brønstedt-Evans-Polanyi (BEP) relation [159;160], a CO_{ad}-substrate bond weakening corresponds to an increase of the barrier for CO_2 dissociation to CO_{ad} on the very small Ru NPs, which in turn must result from distinct differences in the electronic structures of the differently sized Ru NPs on the two catalysts. Using the d-band model introduced by Hammer and Nørskov [161;162], this corresponds to a down-shift of the center of the d-band when going from the 3 nm Ru NPs to the very small Ru NPs in the Ru/zeolite catalyst. Additional effects on the intrinsic activity of the small Ru NPs for CO_2 methanation may be imposed by interaction between the Ru NPs and the zeolite support, which in turn would lead to electronic (and geometric) modifications of the Ru NPs [56].

3.4.3 Conclusions

The influence of the CO partial pressure on the reaction behavior and in particular on the selectivity of a 2.2 wt.% Ru/zeolite and a 5 wt.% Ru/Al_2O_3 catalyst in the selective methanation of CO in CO_2 containing reformate gases was investigated by a combination of kinetic measurements and *in situ* DRIFTS measurements, where the latter focused on the correlation between the build-up of the adlayer and in particular of the CO_{ad} coverage and its influence on the selectivity in the idealized and semi-realistic reformates with different CO contents. These measurements led to the following results and conclusions:

(I) The Ru/zeolite catalyst shows under all reaction conditions a higher activity (up to a factor of 20), and 100% selectivity for CO methanation, even at 100 ppm CO content, whereas for the Ru/Al_2O_3 catalyst the selectivity decreases to 80% and 45% in reaction gas mixtures containing 1000 ppm and 100 ppm CO.

(II) On both catalysts, the reaction rate increases with decreasing CO content, down to 1000 ppm CO in semi-realistic reformate (negative reaction order for CO), while for reaction gas mixtures containing 100 ppm CO the reaction rate decreases again, reflecting a change from a hydrogen limited to a CO_{ad} limited reaction process in a Langmuir-Hinshelwood reaction mechanism.

(III) The steady-state CO_{ad} coverages obtained in low –CO reaction gases (ID-ref 100 and SR-ref 100) differ significantly for the two catalysts. The very different behavior of the two catalysts points i) to a stronger CO_{ad}-Ru interaction on the Ru/Al_2O_3 catalyst and ii) to a lower barrier for CO_2 dissociation on that catalyst compared to the Ru/zeolite catalyst. This is mainly attributed to electronic effects arising from the much smaller size of the Ru NPs on the latter catalyst, and possibly effects introduced by interactions with the support.

(IV) For reaction on the Ru/Al_2O_3 catalyst, the selectivity decreases for the two lower CO contents, and the same trend is obtained also for the CO_{ad} band intensity. Furthermore, CO_{ad} formation in CO_2-ref is facile, resulting in a high steady state CO_{ad} coverage at or close to saturation under these conditions. This supports a mechanism where CO_2 methanation is not inherently inhibited, but limited by blocking of the active surface sites by CO_{ad}. Hence, existence of a sufficiently

high CO_{ad} coverage is precondition for a high selectivity for CO methanation during reaction in CO_2 containing semi-realistic reformate.

(V) For reaction on the Ru/zeolite catalyst, the main reason for a high selectivity for CO methanation and hence for inhibiting the CO_2 methanation is not a blocking of surface sites by adsorbed CO, but rather the low inherent activity of the small Ru NPs for CO_2 dissociation. Using the Brønstedt-Evans-Polanyi relation, the higher barrier for CO_2 dissociation is related to the weaker adsorption of CO on this catalyst, and both result from a change in electronic properties in the very small Ru NPs compared to the larger Ru NPs in the Ru/Al_2O_3 catalyst, with possibly additional contributions from metal-support interactions.

The difference in physical origin for the selectivity for CO methanation between the two catalysts can perfectly explain the high selectivity of the Ru/zeolite in practical applications, with negligible CO_2 methanation down to complete removal of CO (<10 ppm), while for the Ru/Al_2O_3 catalyst, CO_2 methanation will start to contribute as soon as the CO partial pressure and hence the CO_{ad} coverage will drop below a critical value, i.e., in the final part of the reactor. In that case, complete removal of CO will not be possible without contributions from CO_2 methanation.

3.5 Influence of the catalyst loading on the activity and the CO selectivity of supported Ru catalysts in the selective methanation of CO in CO_2 containing feed gases

The previous section dealt with the question of the underlying reasons for the high CO selectivity in case of the 2.2 wt.% Ru/zeolite catalyst. It was shown, that the very small Ru particle size of the zeolite supported catalyst results in a high selectivity of the CO methanation compared to the larger Ru particle size of the Al_2O_3 supported catalyst. On the latter it was observed, that the CO_2 methanation is not inherently inhibited but limited by blocking of active surface sites by CO_{ad}. When the CO_{ad} coverage decreases under a critical value the CO_2 will be methanated. In contrast, on the Ru/zeolite catalyst the situation is different. Even at very low CO_{ad} coverages CO_2 is not methanated. According to the Brønstedt-Evans-Polanyi relation, a higher barrier for CO_2 dissociation is related to the weaker adsorption of CO_{ad} when going from large to small particles. However, an effect on the selectivity of the CO methanation due to variations in the metal support effects of the differently supported catalysts cannot be excluded. Therefore, results of the investigation of the selective methanation of CO over differently loaded Ru/zeolite catalysts, which comprise different Ru particle sizes on the identical zeolite support, in order to exclude contributions of metal support interactions, are presented in the following sections. The methanation of CO and CO_2 over Ru/zeolite catalysts was investigated in idealized and semi-realistic reformate gases by *in situ* diffuse reflectance infrared Fourier transform spectroscopy (DRIFTS) and kinetic measurements.

The results of the following section were published in Catalysis Today 181 (2012) 40: *S.Eckle, M. Augustin, H. G. Anfang and R. J. Behm. Influence of the catalyst loading on the activity and the CO selectivity of supported Ru catalysts in the selective methanation of CO in CO_2 containing feed gases*

3.5.1 *In situ* DRIFTS measurements

The interaction of the different reaction atmospheres with the differently loaded Ru/zeolite catalysts and the resulting adlayer build-up were characterized by sequences of *in situ* DRIFT spectra, which were recorded over 1000 min on stream. The measurements were performed in different reaction atmospheres, including semi-realistic reformates (SR-ref 6000 and SR-ref 100), idealized reaction atmosphere with low CO content (ID-ref 100) and CO_2 reformate (CO_2-ref). The compositions are given in Table 1.

The characteristic bands arising from the interaction with the respective reaction atmospheres are labeled in the spectra in Figure 35, Figure 36, Figure 37. Since the different characteristic bands and their assignment were discussed in detail in section 3.2.3, the assignment of the different signals will be summarized at this point just shortly. On all four catalysts, the characteristic signals are found in the CO_{ad} region at ~2000 - 2040 cm^{-1} and at 1980 cm^{-1}, depending on the CO content in the gas mixture, which are generally attributed to CO adsorbed in a linear or bridged configuration on the Ru NPs, respectively [31;65;79;132-134;136-138;151]. A signal at 2075 cm^{-1} was assigned previously to CO adsorbed on Ru^{n+} species [65;152]. The exact frequencies vary slightly with reaction conditions.

The OH region exhibits two peaks at 3740 and 3600 cm^{-1}, which we relate to silanol species and isolated structural or adsorbed OH groups on the support [141;142]. In CO_2-containing reformates CO_2-related overtone signals (not marked) appear at 3600, 3640, 3700 and 3740 cm^{-1}, in addition to the OH-related signals in this region.

The CH_x spectral region shows the typical $CH_{x,ad}$ signals at 3016, 2928, and 2860 cm^{-1}, arising from gas phase CH_4, $CH_{3,ad}$, and the symmetric and asymmetric CH_2 vibrations on the respective catalysts [27;65;79]. A shoulder at ~2905 cm^{-1} was assigned to the CH vibration of a surface formate [26;30]. Depending on the catalyst and the reaction conditions, only some of the bands are resolved. At higher conversions, all of these bands are visible.

In the OCO region, bands at 1590, 1440, 1390 and 915 cm^{-1} were assigned to surface formates (1590 and 1390 cm^{-1}), carbonates (1440 cm^{-1}) and CH_2 vibrations (915 cm^{-1}) resulting from chain growth.

3.5.2 SR-ref 6000 reformate

In a first set of experiments, the temporal evolution of the different signals of the respective surface species on the 1.0 wt.%, 2.2 wt.%, 3.6 wt.%, and 5.6 wt.% Ru/zeolite catalysts in SR-ref 6000 ($CO/CO_2/H_2/N_2$) was investigated and characterized by sequences of *in situ* DRIFTS measurements (Figure 35 a - d) over 1000 min. During reaction in SR-ref 6000 (Figure 35 a - d), for all four catalysts characteristic signals in the CO_{ad} region are observed at ~2036 cm^{-1} (linear CO_{ad}) and 1980 cm^{-1} (bridged CO_{ad}) [31;65;79;133;134;136-138;151], and a signal at 2080 cm^{-1}, associated with CO adsorbed on oxidized Ru^{n+} or coadsorbed with O_{ad} on Ru [65;132;152]. After passing through a maximum after about 100 min, a constant level of the adsorbed CO_{ad} surface species is reached after ~500 min on all four catalysts. It should be noted that the CO_{ad} band intensity in SR-ref 6000 represents the maximum CO_{ad} intensity that can be reached on the respective catalysts. This was tested in measurements using reaction gas mixtures with higher CO concentrations, which yielded similar band intensities. Accordingly, the CO_{ad} coverage must be at or close to saturation. The loss of the CO_{ad} signal intensity with time on stream, after having passed through the maximum, is most likely due to agglomeration of Ru NPs or deposition of deactivating carbon on the Ru surface as already discussed in section 3.2.

In the OH region, CO_2-related overtone signals (not marked) appear at 3600, 3640, 3700 and 3740 cm^{-1}, in addition to the OH-related signals in this region, which blur the OH signals.

The CH_x spectral region shows the typical $CH_{x,ad}$ signals at 3016, 2928, and 2860 cm^{-1} [65;79]. On all four catalysts, these species (except CH_4) start to grow in after about 15 min on stream and reach a steady-state situation after 1000 minutes. For the CH_4 signal, steady-state is reached much faster, after about 10 min. A shoulder at ~2905 cm^{-1}, observed all on four catalysts, indicates the presence of C-H vibrations of surface formate species [26;30].

In the OCO region, bands at 1590, 1440 and 1390 cm^{-1}, related to surface formates (1590 and 1390 cm^{-1}) and carbonates (1440 cm^{-1}) [26], appear after about 100 min on stream on the four Ru/zeolite catalyst [30;136]. These bands grow steadily in intensity and do not saturate over 1000 min.

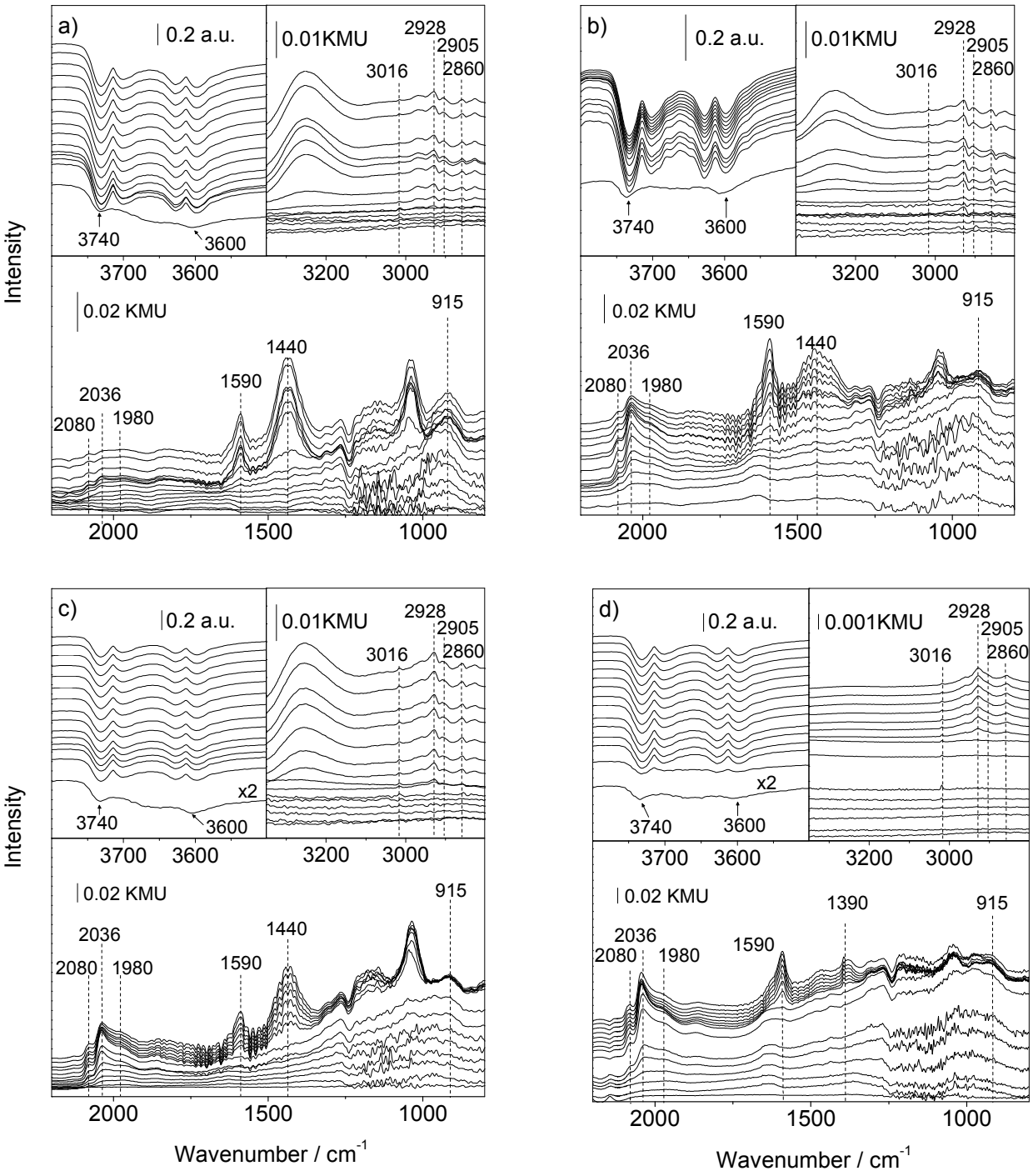

Figure 35: Sequences of DRIFT spectra recorded during 1000 min methanation reaction at 190°C in SR-ref 6000 reformate (a) 1.0 wt.% Ru/zeolite, (b) 2.2 wt.% Ru/zeolite, (c) 3.6 wt.% Ru/zeolite and (d) 5.6 wt.% Ru/zeolite; from bottom to top: 0, 2, 3, 5, 7, 15, 45, 105, 195, 345, 495, 645, 795, 915 min.

The steady-state intensities of the CO_{ad} signal at ~2036 cm^{-1} after 1000 min of the CO_{ad} surface species are given in Table 6.

The steady-state CO_{ad} band intensity (Figure 35 a - d) increases with the amount of active metal deposited on/in the zeolite support, by factors of 2.7, 3.9 and ~5.6 (see Table 6), respectively, with increasing Ru loading. This is significantly more than the increase in Ru surface area, 1.45, 2.04, and 2.81 (calculated from the average Ru particle size) in the same order.

Catalyst	Relative CO_{ad} saturation intensity	Ru surface area* / 10^{19}	ID-ref 100 / %	SR-ref 100 / %	CO_2-ref/ / %	SR-ref 6000 / %
1 wt.% Ru/zeolite	1	0.53	-	-	-	100
2.2 wt.% Ru/zeolite	2.7	0.77	6	6	6	100
3.6 wt.% Ru/zeolite	3.9	1.08	9	10	10	100
5.6 wt.% Ru/zeolite	5.6	1.49	10	12	12	100

Table 6: CO_{ad} band intensity under steady-state conditions during CO methanation on the different catalysts in different reformates. CO_{ad} saturation intensity obtained in SR-ref 6000 relative to that of the 1 wt.% catalyst (2nd column), CO_{ad} intensity relative to saturation on the respective catalyst in semi-realistic reformate (SR-ref 6000) (subsequent columns, data for 2.2 wt.% catalyst from section 3.4).

Quantitative conclusions are hard to draw, however, because of the complex correlation between DRIFTS intensity (in KM units) and total amount of adsorbate molecules for the different catalysts, even if the support is identical. Since the CO_{ad} band intensity was shown earlier to correlate with the methanation activity (see section 3.2.3), the increase in CO_{ad} band intensities can be compared with that in catalytic activity (section 3.5.3). Here it is most appropriate to compare with Ru surface area normalized rates, which are linearly correlated with the turnover frequencies. The latter increase by a factor of 4.4 for going from the 1 wt.% to the 5.6 wt.% Ru/zeolite catalyst.

3.5.3 Reformate gases with low CO concentrations

In order to gain more information on the activity of the catalysts for CO_2 methanation, measurements in three reaction mixtures with low CO contents were conducted, ID-ref 100 (Figure 36 a, b), SR-ref 100 (c, d) and CO_2-ref (CO-free) (Figure 37 a, b), on the 3.6 wt.% (Figure 36 a, c; Figure 37 a) and the 5.6 wt.% (Figure 36 a, d; Figure

37 b) Ru/zeolite catalyst. Similar measurements on the 2.2 wt.% Ru/zeolite catalyst were already reported earlier in this thesis, and the data will be used for comparison. For the 1 wt.% loaded catalyst, a similar adsorption and reaction behavior as for the 2.2 wt.% catalyst is expected.

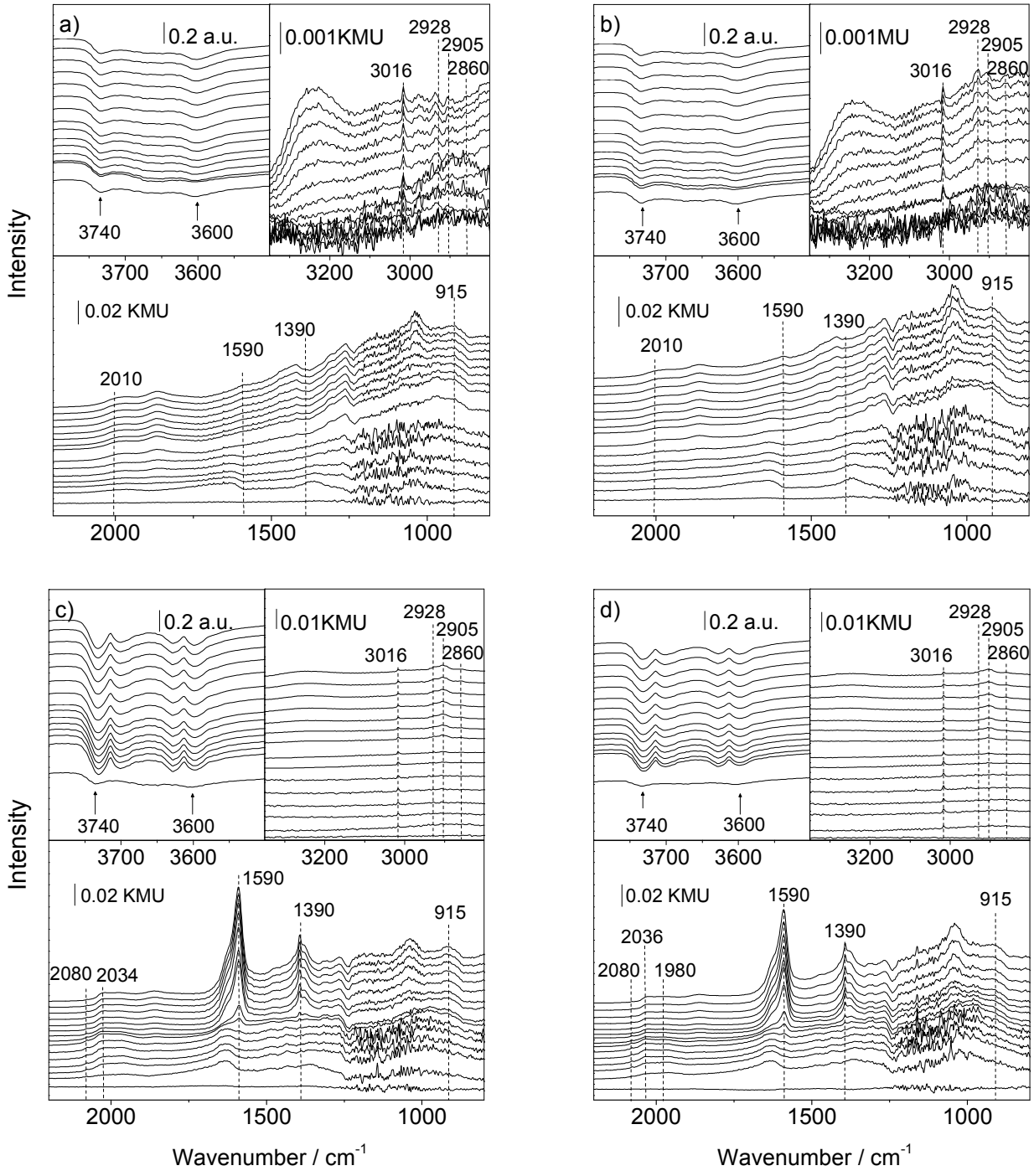

Figure 36: Sequences of DRIFT spectra recorded during 1000 min methanation reaction at 190°C over the Ru/zeolite catalysts; left panels: 3.6 wt.% Ru/zeolite, right panels: 5.6 wt.% Ru/zeolite in ID-ref 100 reformate (a), (b), and SR-ref 100 (c), (d); from bottom to top: 0, 2, 3, 5, 7, 15, 45, 105, 195, 345, 495, 645, 795, 915 min.

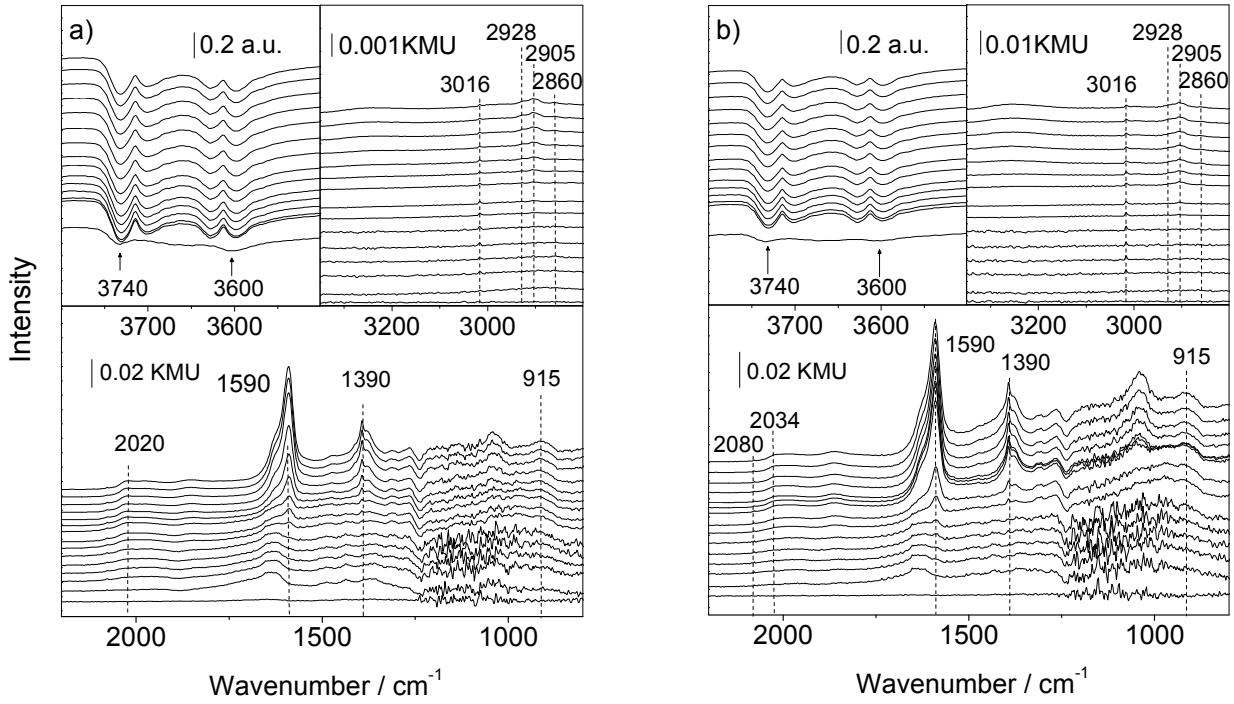

Figure 37: Sequences of DRIFT spectra recorded during 1000 min methanation reaction at 190°C over the Ru/zeolite catalysts; (a) 3.6 wt.% Ru/zeolite catalyst, (b) 5.6 wt.% Ru/zeolite catalyst in CO_2-ref reformate; from bottom to top: 0, 2, 3, 5, 7, 15, 45, 105, 195, 345, 495, 645, 795, 915 min.

The spectra obtained in these atmospheres (SR-ref 100, ID-ref 100 or CO_2-ref) do not differ significantly from the spectra discussed above in their general appearance. They differ, however, in the band intensities, especially of the $CH_{x\ ad}$ and the CO_{ad} related signals, and their temporal evolution. Therefore, the band intensities of the linearly adsorbed CO_{ad} species on Ru obtained in the different reaction atmospheres are plotted vs. time in Figure 38 a, b and c for the 2.2 wt.%, the 3.6 wt.% and the 5.6 wt.% Ru/zeolite catalyst, respectively. The 2.2 wt.% Ru/zeolite catalyst was investigated earlier, the CO_{ad} intensities in Figure 38 a are taken from section 3.4. If, as proposed in section 3.3 and by several research groups [71;73], the methanation of CO_2 proceeds via CO_{ad} as reaction intermediate, the CO_{ad} band intensity can be taken as a measure of the CO_2 methanation activity in CO-free CO_2-ref, while in CO containing reformates the situation is more complex and both CO_2 decomposition and CO adsorption as well as the processes for CO_{ad} removal, CO_{ad} desorption and CO_{ad} methanation, contribute to the steady-state CO_{ad} coverage and band intensity. Therefore the CO_{ad} band intensities in the different reformates have to be compared, ID-ref 100, SR-ref 100, SR-ref 6000 and CO_2-ref, in order to gain more quantitative information about the physical origin of the CO selectivity. The same procedure was

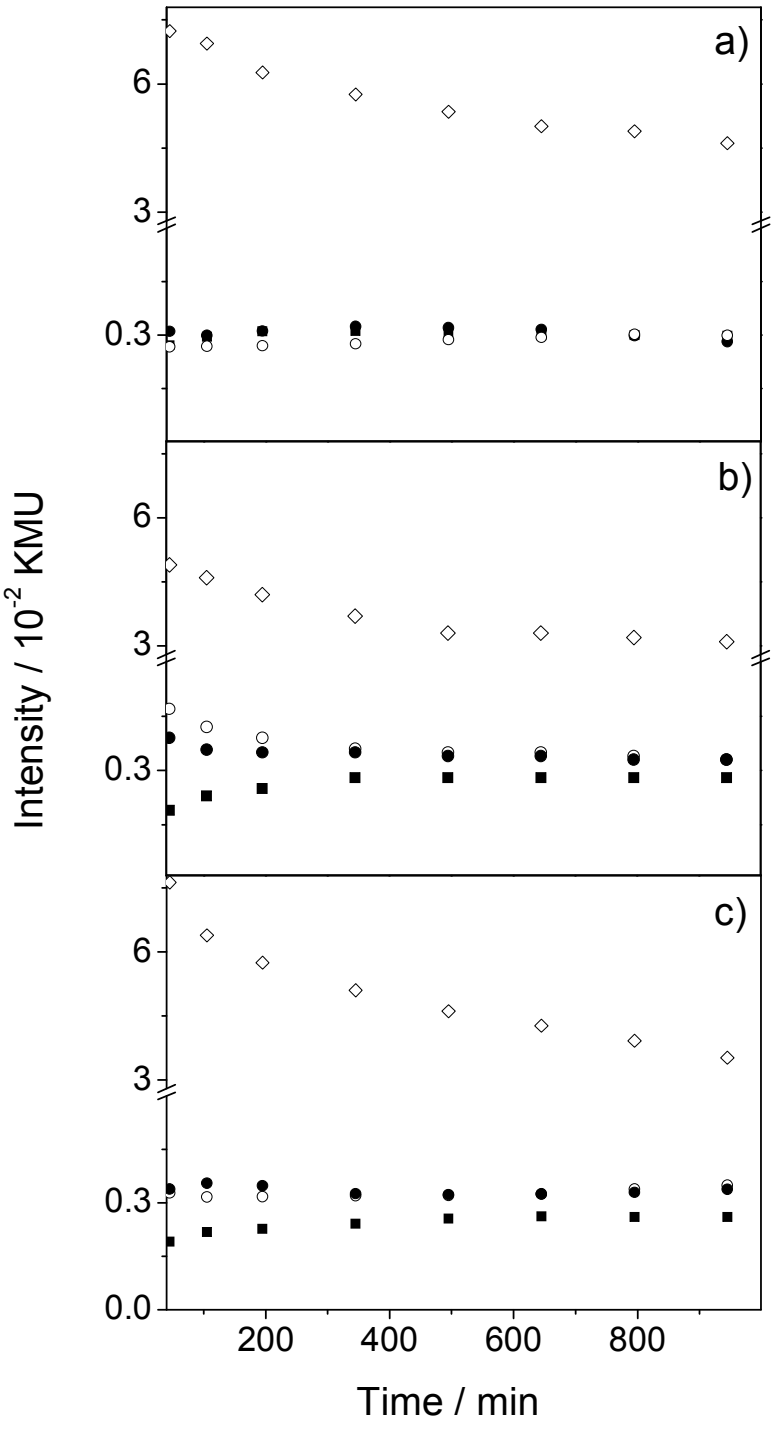

Figure 38: Time evolution of the CO_{ad} band intensities (peak heights) obtained during reaction of the Ru/zeolite catalysts in different reaction atmospheres; (◊) SR-ref 6000, (○) SR-ref 100, (●) CO_2-ref, (■) ID-ref 100. (a) 2.2 wt.% Ru/zeolite catalyst, (b) 3.6 wt.% Ru/zeolite catalyst, (c): 5.6 wt.% Ru/zeolite catalyst.

applied for the 5.0 wt.% Ru/Al_2O_3 and the 2.2 wt.% Ru/zeolite catalyst (see section 3.4), where the differences in the CO_{ad} band intensity obtained in the different reaction gas compositions (CO_2-ref, ID-ref 100 and SR-ref 100) and their correlation with the selectivity for CO methanation in the different semi-realistic reformates indeed allowed

us to draw conclusions on the origin of the selectivity for CO methanation on these catalysts. A similar approach will be used in this section. It should be noted that a similar quantitative evaluation of the evolution of the $CH_{x,ad}$ related band intensities is not possible as these signals at ~2928 cm^{-1} may be due to different surface species, CH_2 groups of carbon chains and $CH_{2,ad}$ as active intermediate for methanation.

The most important observations on the three catalysts are:

(I) In reaction atmospheres with low CO contents (ID-ref 100, SR-ref 100 and CO_2-ref (CO free); Figure 36 a, b, c, d, Figure 37 a and b), the final intensities of the CO_{ad} related signals are reached quickly within the first 100 minutes, as compared to ~800 min of the respective signals in reaction atmospheres with higher CO content (SR-ref 6000) (Figure 38 a, b, c).

(II) The final intensities of the CO_{ad} related bands are significantly lower in atmospheres, with low CO contents, regardless of the presence of CO_2, and in CO_2-ref than in SR-ref 6000 for all catalysts. For the 2.2/3.6/5.6 wt.% Ru/zeolite catalysts, the final CO_{ad} band intensity in ID-ref 100 is only ~6/~9/~10% of that in SR-ref 6000, where the latter corresponds to saturation of the CO_{ad} band intensity. Hence, under these conditions, the Ru NPs are largely free of a reaction inhibiting CO adlayer and *per se* available for CO_2 methanation.

(III) The effect of CO_2 in the gas-phase in low-CO (SR-ref 100) (Figure 36 a and b) or CO-free (CO_2-ref) (Figure 37 b and c; Figure 38 b and c) reformate depends sensitively on the catalyst loading. On the higher loaded 3.6 wt.% and 5.6 wt.% catalysts, the CO_{ad} band intensities in SR-ref 100 and CO_2-ref (CO-free) are ~10 and ~12% of the signal intensity in SR-ref 6000. The presence of CO_2 results in a clear increase in the CO_{ad} band intensity (relative to the intensity in a comparable CO_2-free atmosphere, ID-ref 100), indicating that the rate for CO_2 decomposition to CO_{ad} is of comparable order of magnitude as the rates for CO adsorption (from 100 ppm CO) and CO_{ad} desorption plus methanation, respectively, under present reaction conditions. Accordingly, exposure to CO_2-ref results in a CO_{ad} band intensity which is comparable to that obtained in SR-ref 100.

On the 2.2 wt.% Ru/zeolite catalyst, the situation is distinctly different (Figure 38 a). Addition of CO_2, by going from ID-ref 100 to SR-ref 100 reaction gas, does not increase the CO_{ad} signal intensity significantly. This implies that decomposition of CO_2 to CO_{ad} is slow compared to the rates for CO adsorption

and CO_{ad} removal, by desorption plus CO_{ad} methanation, in SR-ref 100. Correspondingly, the CO_{ad} signal intensity resulting from exposure to CO_2-ref is much lower (~6%) than on the higher loaded Ru/zeolite catalysts and comparable to the that obtained from direct adsorption of CO in 100 ppm CO containing atmosphere (exposure to ID-ref 100), which is also lower than on the higher loaded catalysts.

The above findings directly demonstrate that on the 2.2 wt.% Ru/zeolite catalyst CO_2 decomposition to CO_{ad} on the largely adsorbate-free Ru NPs is significantly slower than on the higher loaded catalysts with their larger Ru NPs, supporting the claim of an inherently slower CO_2 methanation rate on the former catalysts. Since these catalysts differ only in the Ru loading and in the Ru particle size, but not in the nature of the support, the differences in the CO_2 adsorption and CO formation behavior must be due to Ru particle size effects. This will be discussed in more detail in section 3.5.4, after presentation of the catalytic activities.

3.5.4 Kinetic measurements

Figure 39 illustrates the temporal evolution of the Ru mass normalized reaction rates of the 4 different Ru/zeolite catalysts in semi-realistic reformate ($CO/CO_2/H_2$) over 500 min. For all four catalysts, the reaction rate increases initially for about 100 min and stay constant afterwards. Table 7 summarizes the resulting final reaction rates. The results of the 2.2 wt.% catalyst closely resemble the data shown in previous sections [116]. All catalysts show 100% CO selectivity under the present reaction conditions, which is mainly attributed to the fact that in the presence of 6000 ppm CO the surface of the Ru NPs is covered by a reaction inhibiting CO adlayer (the CO_{ad} band intensity is saturated under these conditions on all four catalysts), the high selectivity for CO methanation under these conditions is predominantly attributed to a surface blocking effect, which prevents the decomposition of CO_2 to CO_{ad} and its further reaction to CH_4. The higher CO methanation activity of all Ru/zeolite catalysts compared to the Ru/Al_2O_3 catalyst discussed earlier is attributed to strong metal support-interactions on the Ru/zeolite catalyst (see also below) [79;163]. Pronounced support effects on the CO methanation activity of Ru catalysts with comparable Ru particle sizes had been reported earlier [26;40]. Obviously, the Ru mass normalized reaction rate increases with increasing Ru content. A 5.6 fold increase of the Ru content (1 wt.% to 5.6 wt.% Ru) results in a 2.2 fold increase of the Ru mass normalized rate, and similar effects are observed also for the other two catalysts with intermediate loadings (see Table 7). This effect becomes even more pronounced when accounting for the lower fraction of surface atoms (dispersion) on the larger Ru NPs by using turnover frequencies, which are also listed in Table 4. (The TOFs are calculated assuming hemispherical Ru NPs of the mean particle size for the respective catalysts.) The TOF-based inherent activity of the Ru NPs increases by more than a factor of 4.4 from the 1 wt.% to the 5.6 wt.% Ru/zeolite catalyst. These trends in the CO methanation activity are also evident for reaction in low-CO reformate (SR-ref 100, see below and Figure 40), where the mass based activity / TOF based activity increases by factors of ~1.84 and 2.14, respectively, when going from the 2.2 to the 5.6 wt.% catalyst (see Table 7). Hence, the intrinsic activity of the Ru/zeolite catalysts for CO methanation increased significantly when higher catalyst loadings are used.

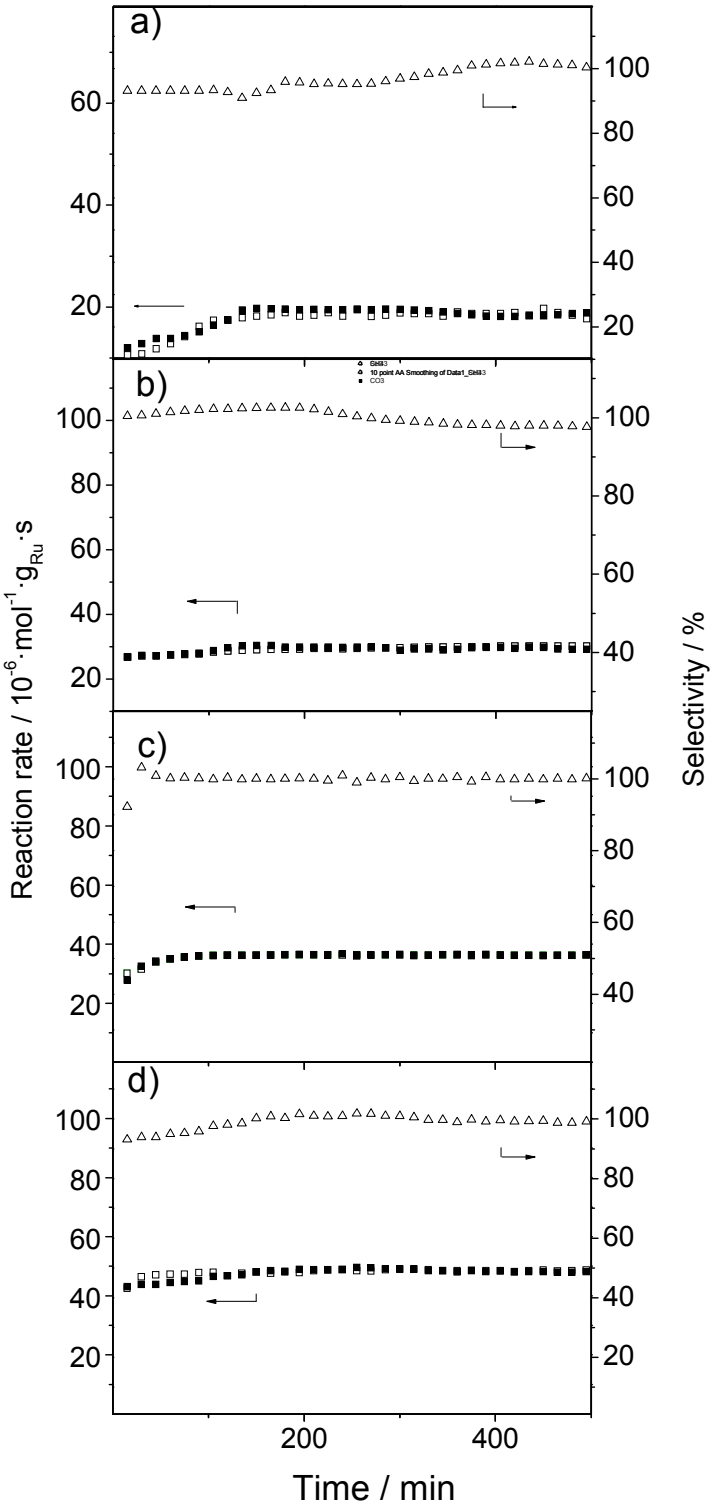

Figure 39: Reaction rates and selectivities obtained for reaction over (a) the 3.6 and (b) the 5.6 wt.% Ru/zeolite catalyst (diluted with SiO_2) under differential reaction conditions in SR-ref 6000. (■): CO reaction rate, (□): CH_4 formation rate, (Δ): selectivity.

Catalyst	Reaction rate / 10^{-6}·mol^{1}·g_{Ru}^{-1} s^{-1}	Loading / / wt.% Ru	Relative reaction rate	Turnover frequency /10^{-3}·s^{-1}	Relative TOFs	Selectivity %
1 wt.% Ru/zeolite	20 / -	1 / -	1	2.5*	1 / -	100 / -
2.2 wt.% Ru/zeolite	30 / 48	2.2	1.5 / 1	3.7 / 6.1	1.5 / 1	100 / 100
3.6 wt.% Ru/zeolite	36 / 50	3.6	1.8 / 1.04	8.0 / 11.2	3.2 / 1.84	100 / 90
5.6 wt.% Ru/zeolite	44 / 52	5.6	2.2 / 1.1	11.1 / 13.1	4.4 / 2.14	100 / 80

* The Ru particle size was assumed to be 0.9 nm, identical to the 2.2 wt.% catalyst

Table 7: Activity (Ru mass normalized final rates) for CO methanation of the different catalysts in semi-realistic reformate (SR-ref 6000) and in low-CO semi-realistic reformate (SR-ref 100) (all columns: SR-ref 6000 / SR-ref 100).

Since there is no change in the nature of the support, which can be unambiguously associated with a particle size effect, leading to a higher activity of the larger Ru particles on the higher Ru loaded catalysts. This even overcompensates the loss of active Ru surface, as evident from the increase in Ru mass normalized reaction rates. In a microscopic picture, this trend can be understood by the increasing adsorption energy and metal-CO interaction of the CO_{ad} when going from smaller to larger particles, which leads to weakening of the C-O bond due to increasing population of the antibonding 2π* orbital [37]. The increase in CO_{ad} adsorption energy is evident from the much lower intensity of the CO_{ad} band and CO_{ad} coverage under steady-state conditions in ID-ref 100 on the 2.2 wt.% catalysts (6% of I_{max}) as compared to the higher loading catalysts (3.6 and 5.6 wt.%: 9% and 10%, respectively, of I_{max}).

A similar trend of the particle size dependent CO methanation activity was reported in early studies by King [127], Kellner et al. [44] and Che and Bennett [45] for reaction on differently loaded Ru/Al_2O_3 catalyst (1-11 wt.% Ru) under Fischer-Tropsch reaction conditions ($CO:H_2$ = 1:2). The dispersion of the Ru NPs was determined by H_2 chemisorption, yielding values between 30 and 90%. Hence, the Ru NPs on these catalysts are clearly smaller than those on the Ru/Al_2O_3 catalyst investigated previously (5 wt.% Ru, dispersion 15% from H_2 chemisorption). Especially at very high dispersions (> 80%) the turnover frequencies were found to decrease dramatically. The above authors explained this by a structural effect, assuming that the methanation of CO requires crystallite faces whose amount increases with increasing

particle size. For comparison, van Hardeveld and Hartog calculated that the fraction of terrace surface atoms (relative to all surface atoms) increases by a factor of 2 when increasing the particle size from 1.0 to 2.0 nm [164]. Comparable particle size effects were reported also for Ru catalysts on different supports in the ammonia synthesis [165], which these authors attributed to a higher number of B_5 adsorption sites on (110) facets on larger Ru NPs than on smaller ones. The support was proposed to play an important role by stabilizing certain Ru particle shapes. Similar effects would be reasonable also for the present systems, for zeolite and Al_2O_3 supported Ru catalysts in the selective CO methanation reaction.

More recent studies investigated the influence of the dispersion on the CO methanation reaction under conditions relevant for feed gas purification [40;41;51]. Although the mechanistic understanding is hampered by the fact that these studies were either performed under integral reaction conditions [40], or the CO_2 and CO methanation were investigated separately at different temperatures under differential reaction conditions [41], the results of these studies agree well with the findings of the early studies [44;45;127] and of the present work in the sense that they also observed an increasing activity with increasing particle size and higher Ru loading.

In the context of the present work, particle size effects on the selectivity are even more interesting than size related variations in the CO methanation activity. Above (section 3.4), it was demonstrated that the 2.2 wt.% Ru/zeolite catalyst exhibits a high CO methanation selectivity even at 100 ppm CO concentration in the presence of 15.5% CO_2, whereas the selectivity of a 5 wt.% Ru/Al_2O_3 catalyst (~2.3 nm Ru particle size) was rather low under similar reaction conditions (see above). It was proposed that the small Ru particles of the Ru/zeolite catalyst are responsible for the high selectivity. In order to test such kind of particle size effects without interference with possible variations in the metal-support interactions, CO methanation experiments in low-CO semi-realistic reformate (SR-ref 100, 0.01% CO, 15.5% CO_2, rest H_2) were performed on the 3.6 wt.% and on the 5.6 wt.% Ru/zeolite catalysts with their larger Ru particle sizes, similar to the previous measurement on the 2.2 wt.% Ru/zeolite catalyst (see section 3.4). Figure 40 a, b and c depict the CO methanation and the CH_4 production rate on the 2.2 wt.%, the 3.6 wt.% and the 5.6 wt.% Ru/zeolite catalysts, whereas Figure 40 d, e and d show the selectivity for CO methanation. The 3.6 wt.% catalyst exhibits a CO methanation rate of 50×10^{-6}mol·g$^{-1}_{Ru}$·s^{-1} and a CO

methanation selectivity of 90%, whereas for the 5.6 wt.% catalyst the corresponding values are 52×10^{-6} mol·g$^{-1}_{Ru}$·s^{-1} and 80%. For the 2.2 wt.% catalyst, values of 48×10^{-6} mol·g$^{-1}_{Ru}$·s^{-1} and 100% were determined (see above). The higher reaction rates compared to reaction in the SR-ref 6000 reformate (0.6% CO) are due to the lower CO concentrations (0.01%), reflecting the negative CO reaction order reported in section 3.2.2.

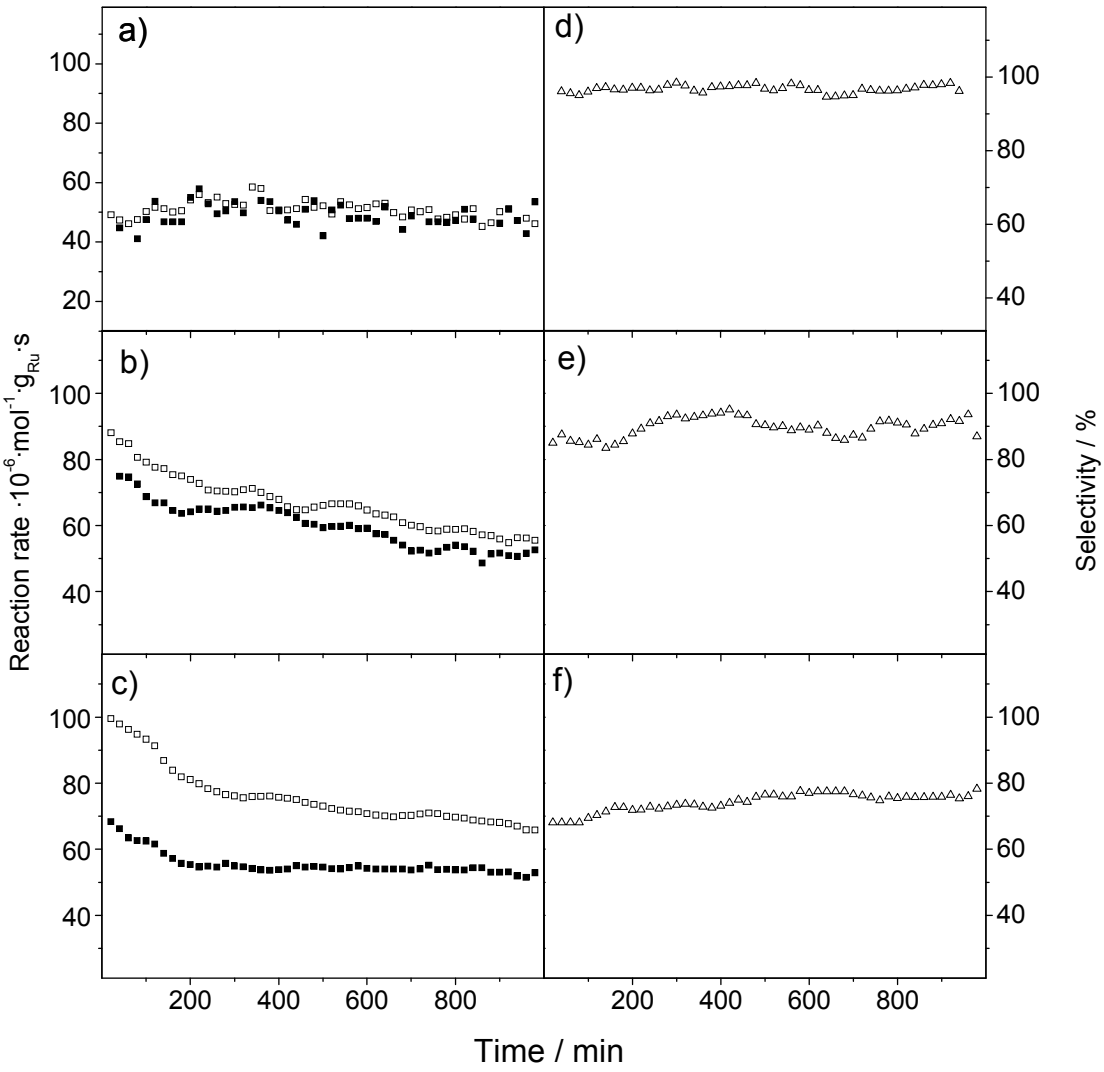

Figure 40: Reaction rates (left panels) and selectivities (right panels) obtained for reaction over the 2.2 (a), (d), 3.6 (b), (e), and 5.6 wt.% (c), (f) Ru/zeolite catalysts (diluted with SiO_2) under differential reaction conditions in SR-ref 100. (■) CO reaction rate, (□) CH_4 formation rate, (Δ) selectivity.

The observed decay in selectivity with increasing Ru particle size agrees well with the trends in the CO_{ad} signal intensities in the DRIFTS measurements, where the difference between reaction in ID-ref 100 and SR-ref 100 increases from essentially zero (2.2 wt.%) via 1% of the saturation intensity (3.6 wt.%) to 2% of the saturation

intensity (5.6 wt.%) (note that the error margins are below 1%), and where the CO_{ad} intensity in CO_2-ref increases from 6% to 12% of the saturation intensity in the same order (Table 6). These trends fully agree also with the previous proposal for the physical origin of the selectivity for CO methanation on Ru/zeolite catalyst (see section 3.4). The very small particles dominant on the lower loaded Ru/zeolite catalysts (1 wt.% and 2.2 wt.%) are little active for CO formation from reversibly adsorbing CO_2, as indicated by the lower CO_{ad} band intensity observed in CO-free CO_2-reformate as compared to the higher loading Ru/zeolite catalysts. (For the 1 wt.% catalyst similar or lower particle sizes are assumed compared to the 2.2 wt.% catalyst based on the adsorption / reaction characteristics.) This is attributed to a higher barrier for CO_2 dissociation, which, according to the Brønstedt-Evans-Polanyi relation [159;160], agrees perfectly with the weaker CO adsorption, derived from the decreasing CO_{ad} band intensity on these catalysts. Hence, on the catalysts, the high selectivity for CO methanation even at low CO concentrations is driven by an inherently low activity for CO_2 methanation, due to a higher barrier for CO formation from reversibly adsorbed CO_2. Of course, at higher CO concentrations site blocking by a closed CO adlayer comes as an additional effect.

For the higher loading Ru/zeolite catalysts it was assumed that their larger mean Ru particle sizes (3.6 wt.%: 1.6 nm, 5.6 wt.%: 1.9 nm) results from a coexistence of larger Ru NPs outside the zeolite particles and very small Ru NPs (0.-8-0.9 nm diameter) inside the pores, as present on the low loading catalysts. On the larger Ru NPs, the selectivity is proposed to be controlled by a site blocking mechanism, where the active Ru surface is essentially covered by strongly adsorbed CO_{ad}, preventing the dissociative adsorption of CO_2, which corresponds to the previous ideas for the origin of the selectivity in the selective CO methanation over Ru catalysts [49;50]. As the CO concentration and hence the CO_{ad} coverage decreases, CO_2 can adsorb on the resulting empty sites and dissociate to CO_{ad}, which acts as intermediate for the CO_2 methanation [71;73]. Therefore, the selectivity for CO methanation decreases with decreasing CO concentration in the feed gas. The very small Ru NPs (in the zeolite pores), which are most likely present also on these catalysts, behave similarly as on the low loading Ru/zeolite catalysts, with an inherently lower activity for CO_2 dissociation to CO_{ad}. On a microscopic scale, this trend towards a higher inherent activity for larger Ru particles can again be explained by in terms of the Brønstedt-

Evans-Polanyi relation, similar to the correlation between CO methanation rate and CO_{ad} adsorption energy, where larger Ru particles result in a higher CO methanation rate and a higher CO adsorption energy. A similar correlation is likely also between CO_{ad} stabilization and CO_2 decomposition, where stabilisation of CO_{ad} (increasing particle size) should be correlated with an increase in CO_2 decomposition (stabilization of the final state and of the transition state), in agreement with experimental findings.

Based on the above trends, the variation in the selectivity for CO methanation on the different Ru/zeolite catalysts is dominated and can be rationalized consistently by particle size effects. This may be different when changing the nature of the support. It was demonstrated above that particle size effects are not sufficient to rationalize the different activities of the Ru/zeolite catalysts and a Ru/Al_2O_3 catalyst with larger Ru NPs (~2.3 nm). Also, for the 5.6 wt.% Ru/zeolite catalysts, whose mean particle sizes is not so different from that of the Ru/Al_2O_3 catalyst, the Ru mass based activity differs by more than one order of magnitude from that of the latter one. (Extrapolating from lower loaded Ru/zeolite catalysts with smaller Ru NPs this difference should even increase when going to hypothetical Ru/zeolite catalysts with even larger Ru NPs (~2.3 nm).) Similar discrepancies are also observed for the inherent activity for CO_2 methanation, which controls the selectivity at low CO concentrations. In section 3.4.1 it was reported, that exposure of the Ru/Al_2O_3 catalyst to CO_2-ref under identical reaction conditions results in a similar CO_{ad} band intensity as obtained in SR-ref 6000, which in turn corresponds to the maximum intensity achieved on this catalyst (CO_{ad} saturation). In contrast, on the 5.6 wt.% Ru/zeolite catalyst, this value was only 12% of the saturation intensity. Hence, on the Ru/Al_2O_3 catalyst with its larger Ru NPs (~2.3 nm particle size), CO_2 decomposition is relatively fast compared to the combined rates of CO_{ad} desorption and CO_{ad} methanation on that catalyst. On the other hand, it has to be considered that on the Ru/Al_2O_3 catalyst also the methanation of the resulting CO_{ad} was much slower, by at least one order of magnitude, than on the 5.6 wt.% Ru/zeolite catalyst (see above and section 3.4), which leads to a higher CO_{ad} steady–state coverage on Ru/Al_2O_3 in CO_2–ref than on the 5.6 wt.% Ru/zeolite catalyst for a similar CO_2 decomposition rate. Hence, metal–support interactions affect also the CO_2 methanation reaction and hence the selectivity, either indirectly via

the build–up of a reaction inhibiting CO adlayer, via the competition between CO_{ad} formation from CO_2 and CO_{ad} removal, or directly.

Finally, a brief comment on the implications of these findings for technical application will be given, i.e., for CO removal from CO–contaminated feed gases for low–temperature polymer electrolyte fuel cells (PEFCs). Obviously, both processes for removal of small amounts of CO (<1%), the preferential oxidation of CO (PROX) and the selective methanation of CO (SelMeth) are facing limitations in the down–stream part of the reactor with its low residual CO concentrations, if the selectivity is only due to reaction inhibiting CO adlayer on the active particles. This leads to considerable H_2 consumption due to H_2 oxidation (PROX reaction) or due to CO_2 methanation (SelMeth reaction). The much simpler technical realization of the SelMeth reaction as compared to a PROX reactor makes this pathway attractive from a technical point of view. Therefore, catalysts with an inherently low activity for H_2 oxidation (PROX reaction) or, as in the present case, for CO_2 methanation (SelMeth reaction) are ideal candidates for complete CO removal from these fuels, and fundamental for the realization of the SelMeth process.

For reaction in the regime of very low CO contents, at the end of the catalyst bed in technical applications, only inherently low activities for CO_2 decomposition will maintain the high selectivities of ~100%, which can be obtained via the site blocking mechanism at higher CO concentrations in the reformate gas mixture. This is crucial for the implementation of the selective methanation as a technically simple and therefore attractive technology for fine purification of H_2-rich feed gases for low-temperature PEFCs, which were prepared by steam reforming of fossil fuels and therefore contain large amounts of CO_2 in addition to CO impurities.

3.5.5 Conclusion

The effect of Ru loading and of the Ru particle size on the reaction behavior of differently loaded Ru/zeolite catalysts in the selective methanation of CO in CO_2-rich reformate gases was systematically investigated, employing *in situ* DRIFTS and kinetic measurements in reformate gases with different CO contents. Combining the structural information (particle sizes) from XAS measurements, the time-resolved information on the build–up of the adlayer and in particular of the CO_{ad} coverage on the different catalysts and in different reaction atmospheres from DRIFTS measurements, and the trends in reactivities and selectivities for CO methanation

obtained from the kinetic measurements, led to the following conclusions on the reaction behavior of these Ru/zeolite catalysts:

(I) The activity of the Ru/zeolite catalysts for CO methanation (both TOF–based activity and Ru mass normalized rates) increases with increasing Ru particle size. Since variations in the metal–support interactions can be excluded, the changes in reactivity purely reflect a particle size effect. In addition, the rates are significantly higher, by at least a one order of magnitude, than for a Ru/Al_2O_3 catalyst under identical reaction conditions and extrapolated to similar particle sizes. This difference must be solely due to a variation in the metal–support interaction.

(II) The adsorption energy of CO_{ad} increases with increasing Ru particle size, as evident from the increasing relative CO_{ad} band intensity and hence increasing CO_{ad} coverage in low–CO idealized reformate under identical adsorption/reaction conditions. In reformate gas with higher CO concentrations, the CO_{ad} band intensity reaches its saturation level, independent of catalyst loading / Ru NP size.

(III) In the absence of CO, the dissociation rate for CO_2 increases with increasing Ru particle size, as indicated by the increasing CO_{ad} band intensity. This leads to an increasing inherent activity for CO_2 methanation with increasing Ru particle size. In good agreement with the increasing activity for CO_2 decomposition, its contribution to the CO_{ad} band intensity in low–CO reformate with Ru loading / NP size, as evident from comparison with the band intensity in the same atmosphere, but without CO_2.

(IV) In low–CO reformate, the CO selectivity decreases with increasing Ru NP size, from 100% for the 2.2 wt.% catalyst to 80% for the 5.6 wt.% Ru/zeolite catalyst. In contrast, in reformate gas with higher CO concentration, the CO selectivity is constant at 100%, independent of catalyst loading / Ru NP size.

(V) The high selectivity for CO methanation of the Ru/zeolite catalysts and its particle size dependence are explained by a combination of two effects: i) a site blocking mechanism, where a reaction inhibiting, strongly bound CO adlayer blocks the decomposition of CO_2 to CO_{ad} and its further methanation, as it was proposed for Ru catalysts earlier, and ii) a decreasing inherent activity for CO_2 dissociation to CO_{ad} with decreasing Ru particle size. The former results in a high selectivity at higher CO concentrations, independent of the Ru particle size, while the latter is responsible for the very high selectivities obtained even at very low CO concentrations, despite the presence of vast amounts of CO_2. The pronounced decrease in activity for CO_2 dis-

sociation for very small Ru particles is explained in terms of the Brønstedt-Evans-Polanyi relation, with the barrier for CO_2 dissociation increasing with a decrease of the CO_{ad} adsorption energy at decreasing Ru particle size.

(VI) In addition to particle size effects, also metal–support interactions play a role and affect the selectivity for CO methanation of the Ru/zeolite catalysts, as evident from the much higher selectivity of the highest loading Ru/zeolite compared to the Ru/Al_2O_3 catalyst with similar particle sizes in low–CO reformate. Metal support interactions may affect the selectivity either directly, via the activity for CO_2 decomposition, or indirectly, by modifying the ratio between CO_{ad} formation and CO_{ad} removal (desorption plus methanation), which changes the steady–state coverage of the reaction inhibiting CO adlayer.

4 Summary

In the present PhD thesis I described the investigations of the mechanism of the selective CO methanation in the presence of CO_2 in H_2-rich feed gases over various supported Ru catalysts and presented their results. During this thesis I introduced the *in situ* X-ray Absorption Spectroscopy as characterization method for very small Ru nanoparticles on zeolite supported catalysts and constructed an *in situ* XAS reaction cell and a portable gas mixing unit, in order to perform *in situ* experiments at a synchrotron. These measurements revealed changes in the average coordination numbers of the Ru nanoparticles and its oxidation state. The results of the *in situ* XAS measurements gave access to the mean particle size of the different Ru/zeolite catalysts. This in consequence allowed me to compare the intrinsic activity and to draw conclusions on the driving force behind the differences in CO selectivity for the particular catalysts, a 1.0 wt.% 2.2 wt.%, 3.6 wt.% and 5.6 wt.% Ru/zeolite and 5 wt.% Ru/Al_2O_3 catalyst.

The obtained results during this work can be summarized as follows:

(I) The catalysts feature different Ru nanoparticle sizes which were derived from *in situ* EXAFS measurements for the 2.2, 3.6 and 5.6 wt.% Ru/zeolite (d= 0.9, 1.6 and 1.9 nm) catalyst and from TEM as well as *in situ* EXAFS experiments for the Ru/Al_2O_3 (2.3 nm) catalyst. Standard characterization techniques such as TEM, XRD did not lead to realistic Ru particle sizes for the Ru/zeolite catalyst, due to the decomposition of the zeolite support under the focused electron beam during TEM measurements and the parallel existence of large and very small nanoparticles in case of XRD experiments. The similar particle size derived by *in situ* EXAFS and TEM for the Ru/Al_2O_3 catalyst underlined the correctness of evaluation. The Ru nanoparticles of the Ru/zeolite catalyst are expected to be located inside the pores mostly, as indicated by the small Ru particle size. For the 2.2 wt.% Ru/zeolite catalyst, the mean particle sizes almost correspond to the pore size of the zeolite support. In addition, a much smaller XPS intensity on this catalyst compared to the Ru/Al_2O_3 catalyst provided additional evidence of the existence of the small Ru nanoparticles. The increasing average particle size with higher metal loading on the Ru/zeolite catalyst was explained by the existence of a larger amount of bigger Ru particles on the outer surface.

(II) All catalysts are active for the methanation of CO. The CO_2 methanation activity in contrast was dependent on the catalyst and on the Ru particle size. Integral measurements showed a higher CO methanation activity and selectivity of the 2.2 wt.% Ru/zeolite catalyst compared to the 5.0 wt.% Ru Al_2O_3 catalyst. The experiments revealed that the Ru/zeolite catalyst exhibits 100% conversion at a 20°C lower temperature (190°C) than the Ru/Al_2O_3 catalyst (210°C). The major difference of the two catalysts lies in the methanation of CO_2, where the 2.2 wt.% Ru/zeolite catalyst exhibits a selectivity of 100% for CO under semi-realistic conditions ($H_2/CO/CO_2$) at this temperature. CO_2 only is converted at much higher temperatures, where 50% CO_2 conversion are reached at 330°C and full conversion is achieved at 410°C. Even if no CO is present (H_2/CO_2) the conversion of CO_2 reaches 50% and full conversion at the same temperatures. On the other hand, the Ru/Al_2O_3 catalyst shows full CO_2 conversion at 230 °C, even in the presence of CO ($H_2/CO/CO_2$). The catalyst readily converts CO_2 in CO free reformates (H_2/CO_2) exhibiting full conversion at the same temperature as under CO methanation conditions (210°C), pointing to unselective active sites, which readily methanate CO and CO_2 even at low temperatures. On the latter catalyst the selectivity is driven by the much higher adsorption enthalpy of CO compared to CO_2. As long as the partial pressure of CO is sufficiently high, CO_2 will not be methanated.

(III) The reaction rates of both catalysts are in a range between 3.1 and 4.4 or 31.8 and 63.9x10^{-6} mol·g^{-1}_{Ru}·s^{-1} for the 5.0 wt.% Ru/Al_2O_3 and the 2.2 wt.% Ru/zeolite catalyst, respectively, depending on the reformate gases. Addition of CH_4 and CO_2 did not significantly affect the reaction rate on both catalysts. In contrast, the addition of 5 % H_2O to the gas mixture resulted in a twofold lower activity for the Ru/zeolite catalyst, which also corresponds to a 50% lower linearly adsorbed CO_{ad} signal intensity on metallic Ru during the *in situ* DRIFTS experiments. Obviously, water prevents adsorption of CO on Ru on this catalyst and also blocks active sites for the reaction intermediate. The activation energy of the selective methanation was in the range between 90 and 110 kJ·mol^{-1} for both, the Ru/zeolite and the Ru/Al_2O_3 catalyst. The reaction order of CO was measured to be -0.7 and -0.5 for the Ru/zeolite and the Ru/Al_2O_3 catalyst, respectively. The reaction order of H_2 was found to be 1.0 on the Ru/Al_2O_3 catalyst compared to 2.7 on the Ru/zeolite catalyst as determined in my diploma thesis. This distinctly higher value on the latter catalyst was proposed as one reason for the higher CO methanation activity of the Ru/zeolite catalyst compared to

that of the Ru/Al_2O_3 catalyst. Transient experiments carried out by *in situ* DRIFTS and mass spectroscopic measurements, where CO was replaced by N_2 after 1000 min of reaction, revealed that the observed $CH_{x,ad}$ species cannot play a dominant role in the reaction pathway, since their off reaction, followed by the *in situ* DRIFTS measurements, does not match with the depletion of CH_4 measured by the mass spectrometer. It was shown that possibly only a small fraction of reactive CH_x takes part in the reaction whose bands are obscured by large signals of produced side products.

(IV) The molecular mechanism of the CO methanation and the CO_2 methanation was investigated by SSITKA (Steady State Isotope Transient Kinetic Analysis) experiments, where after reaching a dynamic equilibrium (1000 min) one educt (^{12}CO or $^{12}CO_2$) was replaced by its isotopomer (^{13}CO or $^{13}CO_2$). It was shown, that on the Ru/Al_2O_3 a 'formyl' species (CHO_{ad}) is likely to act as a reaction intermediate of the CO methanation, since the off reaction of this surface species, determined in the *in situ* DRIFTS experiments, revealed a similar reaction rate as observed in the kinetic measurements. The same mechanism is tentatively assigned to occur on the Ru/zeolite, although such a formyl species was not yet detected. This is explained by the much higher activity (20 fold) for the reaction and possibly also for the off reaction, where the surface concentration of such a species is likely to be below the detection limit. For the CO_2 methanation it was shown by similar experiments on both catalysts that CO_2 adsorbs and dissociates directly to CO_{ad} under the present reaction conditions. A participation of formates can be excluded. The produced CO_{ad} reacts further to CH_4.

The combination of the above mentioned results proposes CO_{ad} adsorbed on metallic Ru as active species which reacts to CH_4 via HCO_{ad}, which is also adsorbed on the Ru nanoparticles. Moreover I showed, that the Ru/zeolite catalyst, comprising very small Ru particles, exhibits a higher reaction rate compared to the Ru/Al_2O_3 catalyst. This is currently explained by metal support effects, and by the high reaction order for hydrogen. In addition the Ru/zeolite catalyst showed in integral measurements a very high selectivity for CO methanation, which is also explained by the very small Ru particles (see below). The observed high selectivity for CO methanation may also be an explanation for the fact, that the Reverse Water Gas Shift reaction did not occur on the Ru/zeolite catalyst under the conditions applied during this work.

(V) By combination of kinetic and *in situ* IR (DRIFTS) results it was possible to demonstrate that the particle size influences the CO selectivity of the CO methanation reaction. On the Ru/Al_2O_3 catalyst, which features larger particles (~ 2.3 nm), derived by *in situ* EXAFS and TEM measurements, the CO selectivity is solely controlled by a surface blocking mechanism. As long as sufficient gas phase CO is present to form a monolayer of CO_{ad} (saturation coverage) on the active sites, CO_2 will not be dissociated. Once the monolayer of adsorbed CO_{ad} cannot be maintained, as the gas phase CO concentration decreases below a critical value, free active sites will adsorb and dissociate CO_2 to CO_{ad}. In consequence, the CO selectivity decreases to about 45% in very low CO partial pressures in the presence of CO_2 (100 ppm CO). These selectivity values correlated with the CO_{ad} band intensities measured in different reformates. The situation is very different for the 2.2 wt.% Ru/zeolite catalyst, which features very small Ru nanoparticles (d= 0.9 nm), as derived by *in situ* EXAFS measurements. Here, CO_2 is not adsorbed and dissociated even if the reformate contains only 100 ppm CO besides CO_2. Kinetic experiments revealed a 100% CO selectivity under all investigated reaction conditions. *In situ* DRIFTS showed that even in a CO free reformate the CO_{ad} signal intensity reaches only 6% of the possible CO_{ad} saturation band intensity (on the Ru/Al_2O_3 catalyst saturation coverage was reached). This points to an inherently low CO_2 methanation activity, which was attributed to a very low activity of the very small Ru NPs for the dissociation of CO_2. This different behaviour of the two catalysts was explained by the Brønstedt-Evans-Polanyi (BEP) relation, according to which CO_{ad} is adsorbed weaker on smaller nanoparticles than on larger nanoparticles. This in turn raises the dissociation barrier for CO_2, since the intermediate (CO_{ad}) is less stable on smaller nanoparticles.

(VI) In order to confirm the CO selectivity model presented above, similar experiments were carried out on differently loaded (3.6 and 5.6 wt.%) Ru/zeolite catalysts. These experiments enabled the identification of the particle size as driving force for the CO selectivity apart from possible support effects. The higher loaded catalysts featured larger average particle sizes (d= 1.6 and 1.9 nm), where the particle size of the catalyst with the highest loading was comparable to that of the standard Ru/Al_2O_3 catalyst. The rate of CO_2 methanation and in consequence its dissociation increased with larger particles, when the CO concentration was low. The selectivity derived from the results of the kinetic measurements, correlates well again with the CO_{ad} band intensity of the Ru/zeolite catalysts under different gas atmospheres. In

addition, the increase in particles size correlated with an increase of the reaction rate (Ru mass normalized). This was explained by the existence of a larger number of active Ru sites (e.g. B5 sites) on larger nanoparticles, as it is often proposed in the present Literature.

Finally, the importance of the present results for practical applications is presented. Using the 5.0 wt.% Ru/Al_2O_3 and the 3.6 or 5.6 wt.% Ru/zeolite catalysts with Ru nanoparticles larger than 1 nm, CO_2 methanation will start to contribute as soon as the CO partial pressure and hence the CO_{ad} coverage will drop below a critical value, i.e., in the final part of the methanation reactor. In that case, complete removal of CO will not be possible without contributions from CO_2 methanation, and this was indeed observed experimentally. The higher loaded Ru/zeolite catalysts showed in fact a higher methanation reaction rate, however, on the cost of the CO selectivity. For the 2.2 wt.% Ru/zeolite catalyst, in contrast, CO_2 methanation is essentially inhibited even at very low CO_{ad} coverages, due to the inherent low activity of this catalyst, and most likely of the very small Ru NPs for dissociative adsorption of CO_2 and the subsequent methanation of the resulting CO_{ad}. Hence, the mechanistic origin of the selectivity for CO methanation is distinctly different from that on the Ru/Al_2O_3 catalyst. This allows highly selective CO removal even at very low CO contents in the reformate, and hence complete removal of CO (> 10 ppm) from CO containing feed gases for fuel cells without measurable CO_2 methanation, as long as the reaction temperature is kept below the onset of significant CO_2 dissociation. Based on the inherently low activity for CO_2 methanation, the Ru/zeolite catalyst is predicted to perform also very well under dynamic reaction conditions, where the variation in CO_{ad} coverage would otherwise lead to substantial CO_2 methanation.

As a final point, the results showed that the Ru particle size is the key to control the CO methanation selectivity. It is therefore essential to maintain a small Ru particle size in order to preserve a high CO selectivity during reaction. This can be achieved by using a zeolite support where the Ru nanoparticles are mostly located inside the pores, which slows down their agglomeration and in turn the CO_2 methanation, resulting in a high efficiency of the process. This concept is the precondition for PEM fuel cells, since they require stable H_2 purification catalysts, to prevail against standard technologies.

5 References

1 W. Lubitz and W. Tumas, Chem. Rev., 107 (2007) 3900-3903.

2 K. Kochloefl, in G.Ertl, H.Knözinger, and J.Weitkamp (Eds.), Handbook of Heterogeneous Catalysis, Vol. 2, Wiley-VCH, Weinheim, 1997.

3 S. Kawatsu, J. Power Sources, 71 (1998) 150-155.

4 D. L. Trimm and Z. I. Önsan, Catal. Rev., 43 (2001) 31-84.

5 J. R. Rostrup-Nielsen and K. Aasberg-Petersen, in W.Vielstich, H.A.Gasteiger, and A.Lamm (Eds.), Fuel Cell technology and applications, Vol. 3, Wiley, Chichester, 2003, Ch. 14.

6 J. Sehested, S. Dahl, J. Jacobsen, and J. R. Rostrup-Nielsen, J. Phys. Chem. B, 109 (2005) 2432-2438.

7 R. M. Navarro, M. A. Pena, and J. L. G. Fierro, Chem. Rev., 107 (2007) 3952-3991.

8 D. R. Palo, R. A. Dagle, and J. D. Holladay, Chem. Rev., 107 (2007) 3992-4021.

9 O. Deutschmann and L. D. Schmidt. Two dimensional modeling of partial oxidation of methane on rhodium in a short contact time reactor. Twenty-Seventh Symposium (International) on Combustion/The Combustion Institute. 2283-2291. 1998

10 S. Gottesfeld and T. A. Zawodzinski, in R.C.Alkire, H.Gerischer, D.M.Kolb, and C.W.Tobias (Eds.), Advances in Electrochemical Science and Engineering, Vol. 5, Wiley-VCH, Weinheim, 1997.

11 W. Vielstich, in A.J.Bard, M.Stratmann, and E.J.Calvo (Eds.), Encyclopedia of Electrochemistry - Interfacial Kinetics and Mass Transport, Vol. 2, VCH, Weinheim, 2003.

12 J. R. Ladebeck and J. P. Wagner, in W.Vielstich, A.Lamm, and H.A.Gasteiger (Eds.), Handbook of Fuel Cells - Fundamentals Technology and Applications, Vol. 3, Wiley, Chichester, 2003, Ch. 16.

13 L. Shore and R. Farrauto, in W.Vielstich, H.A.Gasteiger, and A.Lamm (Eds.), Fuel Cell technology and applications, Vol. 3, Wiley, Chichester, 2003, Ch. 18.

14 S. Sircar and T. C. Golden, Separation Science and Technology, 35 (2000) 667-687.

15 E. Riedel, Anorganische Chemie, Walter de Gruyter, Berlin, 1994.

16 E. D. Park, D. Lee, and H. C. Lee, Catal. Today, 139 (2009) 280-290.

17 M. Echigo and T. Tabata, J. Chem. Eng. Japan, 37 (2004) 75-81.

18 J. R. Rostrup-Nielsen, K. Pedersen, and J. Sehested, Appl. Catal. A, 330 (2007) 134-138.

19 H. Pichler, in W.G.Frankenburg (Ed.), Adv. Catal., Academic Press, 1952.

20 V. Ponec, Catalysis Reviews, 18 (1978) 151-171.

21 G. Henrici-Olivé and S. Olivé, Angew. Chem. Int. Ed. Engl., 15 (1976) 136-141.

22 G. A. Mills and F. W. Steffgen, Catal. Rev. Sci. Eng., 8 (1974) 159-210.

23 S. S. Ranghava and R. C. E. H. Amirali, I&EC Process Design and Development, (1969) 482-486.

24 M. A. Vannice, J. Catal., 37 (1975) 449-461.

25 M. Boudart and M. A. McDonald, J. Phys. Chem., 88 (1984) 2185-2195.

26 R. A. Dalla Betta and M. Shelef, J. Catal., 48 (1977) 111-119.

27 J. G. Ekerdt and A. T. Bell, J. Catal., 58 (1979) 170-187.

28 H. Yamasaki, K. Yoshihiro, Y. Kobori, S. Naito, T. Ohnishi, and K. Tamaru, J. Chem. Soc. Faraday Trans. I, 77 (1980) 2913-2925.

29 R. D. Kelley and D. W. Goodman, in D.A.King and D.P.Woodruff (Eds.), Fundamental Studies of Heterogeneous Catalysis, Vol. 4, Elsevier Scientific Publishing, Amsterdam, 1982, Ch. 10.

30 N. M. Gupta, V. S. Kamble, V. B. Kartha, R. M. Iyer, K. R. Thampi, and M. Gratzel, J. Catal., 146 (1994) 173-184.

31 N. M. Gupta, V. P. Londhe, and V. S. Kamble, J. Catal., 169 (1997) 423-437.

32 N. M. Gupta and A. K. Tripathi, Bull. Catal. Soc. India, (2003) 213-219.

33 L. Caldwell. Selectivity in Fischer-Tropsch Synthesis. 660 5 2, 1-4. 1-6-1980. South Africa, Council for Scientific and Industrial Research.

34 C. H. Bartholomew, Catal. Lett., 7 (1990) 303-316.

35 M. P. Andersson, T. Bligaard, A. Kustov, K. E. Larsen, J. Greeley, T. Johannessen, C. H. Christensen, and J. K. N°rskov, J. Catal., 239 (2006) 501-506.

36 M. P. Andersson, F. Abild-Pedersen, I. N. Remediakis, T. Bligaard, G. Jones, J. Engbæk, O. Lytken, S. Horch, J. H. Nielsen, J. Sehested, J. R. Rostrup-Nielsen, J. K. Nørskov, and I. Chorkendorff, J. Catal., 255 (2008) 6-19.

37 O. R. Inderwildi, S. J. Jenkins, and D. A. King, J. Phys. Chem. C, 112 (2008) 1305-1307.

38 T. Bligaard, J. K. Nørskov, S. Dahl, J. Matthiesen, C. H. Christensen, and J. Sehested, J. Catal., 224 (2004) 206-217.

39 J. Zhang, M. B. Vukmirovic, K. Sasaki, U. N. Anand, M. Mavrikakis, and R. Adzic, J. Am. Chem. Soc., 127 (2005) 12480-12481.

40 A. R. Dagle, Y. Wang, G.-G. Xia, J. J. Strohm, J. Holladay, and D. R. Palo, Appl. Catal. A, 326 (2007) 213-218.

41 Z. Kowalczyk, K. Stolecki, W. Rarog - Pilecka, E. Miskiewicz, E. Wiczkowska, and Z. Karpinski, Appl. Catal. A, 342 (2008) 35-39.

42 P. Panagiotopoulou, D. I. Kondarides, and X. E. Verykios, Appl. Catal. A, 344 (2008) 45-54.

43 D. L. King and J. B. Peri, J. Catal., 79 (1979) 164-175.

44 C. S. Kellner and A. T. Bell, J. Catal., 75 (1982) 251-261.

45 M. Che and C. O. Bennet, Adv. Catal., 36 (1989) 55-172.

46 K. Asakura and Y. Iwasara, J. Chem. Soc. Faraday Trans. I, 86 (1990) 2657-2662.

47 C. Galletti, S. Specchia, G. Saracco, and V. Specchia, Chem. Engin. Sci., 65 (2010) 590-596.

48 C. Galletti, S. Specchia, and V. Specchia, Chemical Engineering Journal, 167 (2011) 616-621.

49 T. Inui, M. Funabiki, and Y. Takegami, Ind. Eng. Chem. Prod. Res. Dev., 19 (1980) 385-388.

50 M. B. I. Choudhury, S. Ahmed, and M. A. Shalabi, Appl. Catal. A, 314 (2006) 47-53.

51 P. Panagiotopoulou, D. I. Kondarides, and X. E. Verykios, Appl. Catal. B, 88 (2009) 470-478.

52 K. Urasaki, K. i. Endo, T. Takahiro, R. Kikuchi, T. Kojima, and S. Satokawa, Top. Catal., 53 (2010) 707-711.

53 V. Jimonez, P. Sanchez, P. Panagiotopoulou, J. L. Valverde, and A. Romero, Appl. Catal. A, 390 (2010) 35-44.

54 P. Djinovic, C. Galletti, S. Specchia, and V. Specchia, Catal. Today, 164 (2011) 282-287.

55 P. Panagiotopoulou and D. I. Kondarides, J. Catal., 225 (2004) 327-336.

56 M. Krämer, M. Duisberg, K. Stöwe, and WF. Maier, J. Catal., 251 (2007) 410-422.

57 M. Krämer, K. Stöwe, M. Duisberg, F. Müller, M. Reiser, S. Sticher, and WF. Maier, Appl. Catal. A, 369 (2009) 42-52.

58 D. J. Elliott and J. H. Lunsford, J. Catal., 57 (1979) 11-26.

59 A. Rehmat and S. S. Randhava, Ind. Eng. Chem. Prod. Res. Dev., 9 (1970) 512-515.

60 O. Görke, P. Pfeifer, and K. Schubert, Catal. Today, 110 (2005) 132-139.

61 V. P. Londhe, V. S. Kamble, and N. M. Gupta, J. Mol. Catal. A, 121 (1997) 33-44.

62 D. Li, N. Ichikuni, S. Shimazu, and T. Uematsu, Appl. Catal. A, 180 (1999) 227-235.

63 M. P. Andersson, T. Bligaard, A. Kustov, K. E. Larsen, J. Greeley, T. Johannessen, C. H. Christensen, and J. K. Nørskov, J. Catal., 239 (2006) 501-506.

64 O. Inderwildi and P. Jenkins, Chem. Soc. Rev., 37 (2008) 2274-2309.

65 M. W. McQuire and C. H. Rochester, J. Catal., 141 (1993) 355-367.

66 H. H. Nijs and P. A. Jacobs, J. Catal., 66 (1980) 401-411.

67 D. W. Goodman, R. D. Kelley, T. E. Madey, and J. T. Yates, J. Catal., 63 (1980) 226-234.

68 H. P. Bonzel and H. J. Krebs, Surf. Sci., 91 (1980) 499-513.

69 A. T. Bell, Cat. Rev. Sci. Eng., 23 (1981) 203-232.

70 R. D. Kelley and D. W. Goodman, Surf. Sci., 123 (1982) L743-L749.

71 I. A. Fisher and A. T. Bell, J. Catal., 162 (1996) 54-65.

72 O. Inderwildi, Jenkins.J.S., and D. King, Angew. Chem. Int. Ed., 47 (2008) 5253-5255.

73 M. R. Prairie, A. Renken, J. G. Highfield, K. R. Thampi, and M. Grätzel, J. Catal., 129 (1991) 130-144.

74 L. F. Liotta, G. A. Martin, and G. Deganello, J. Catal., 164 (1996) 322-333.

75 Y. Traa and Weitkamp J., Chem. Eng. Technol., 21 (1999) 291-293.

76 K. Yaccato, R. Carhart, A. Hagemeyer, A. Lesik, P. Strasser, A. F. Volpe jr., H. Turner, H. Weinberg, R. K. Graselli, and C. Brooks, Appl. Catal. A, 296 (2005) 30-48.

77 J.-N. Park and E. W. McFarland, J. Catal., 266 (2009) 92-97.

78 H. Y. Kim, H. M. Lee, and J.-N. Park, J. Phys. Chem., 114 (2010) 7128-7131.

79 S. Scirè, C. Crisafulli, R. Maggiore, S. Minico, and S. Galvagno, Catal. Lett., 51 (1998) 41-45.

80 R. Burch, Phys. Chem. Chem. Phys., 8 (2006) 5483-5500.

81 O. Levenspiel, Chemical Reaction Engineering, Wiley & Sons, New York, 1972.

82 M. J. Kahlich. Untersuchungen zur selektiven CO-Oxidation an geträgerten Edelmetallkatalysatoren in einem Gasphasenreaktorsystem mit on-line Analytik (1996) Universität Ulm.

83 M. J. Kahlich. CO-Feinreinigung H_2-reicher Reformergase durch selektive Oxidation an geträgerten Edelmetallkatalysatoren: Kinetische Untersuchungen und Reaktoredesign-Berechnungen(2000) Universität. Ulm.

84 M. M. Schubert. In-situ DRIFTS (diffuse reflectance infrared Fourier transform spectroscopy) Messungen zur Charakterisierung der selektiven CO- Oxidation in H_2-reichem Gas (2000) University of Ulm.

85 S. Hackenberg. Untersuchungen zum Einfluß von Kalium und Cadmium auf die Formierung und katalytische Aktivität SiO2 geträgerter Palladiumkatalysatoren bei der Totaloxidation von Ethylen (2002) Universität Ulm.

86 R. Leppelt. Untersuchungen zur Wasser-Gas-Shift-Reaktion bei tiefen Temperaturen an geträgerten Goldkatalysatoren (2002) Universität Ulm.

87 Z. Liu, L. M. Gan, L. Hong, W. Chen, and J. Y. Lee, J. Power Sources, 139 (2005) 73-78.

88 Handbook of Heterogeneous Catalysis, VCH-Wiley, Weinheim, 1997.

89 J. W. Niemantsverdriet, Spectroscopy in Catalysis - An Introduction -, VCH, Weinheim, 1993.

90 S. V. Thomas and V. I. Birss, J. Electrochem. Soc., 144 (1997) 1353-1362.

91 D. Briggs and M. P. Seah, Practical Surface Analysis - Auger and X-Ray Photoelectron Spectroscopy, 2nd ed., John Wiley & Sons, Chichester, 1990.

92 G. A. Somorjai, Introduction to Surface Science and Catalysis, John Wiley and Sons, New York, 1994.

93 J. F. Moulder, W. F. Stickle, P. E. Sobol, and K. D. Bomben, Handbook of X-ray Photoelectron Spectroscopy, Perkin Elmer Corp., Eden Prairie/USA, 1992.

94 J. C. Fuggle, T. E. Madey, M. Steinkilberg, and D. Menzel, Surf. Sci., 52 (1975) 521-541.

95 R. Nyholm and N. Martensson, J. Phys. C. Solid State Phys., 13 (1980) L279-L284.

96 R. A. Dalla Betta, J. Phys. Chem., 79 (1975) 2519-2525.

97 G. Bergeret and P. Gallezot, in G.Ertl, H.Knözinger, and J.Weitkamp (Eds.), Handbook of Heterogeneous Catalysis, Vol. 2, Wiley-VCH, Weinheim, 1997.

98 R. A. D. Betta, J. Catal., 34 (1974) 57-60.

99 T. Armaroli, T. Bécu, and S. Gautier, Oil&Gas Science and Technology, 59 (2004) 215-237.

100 P. Kubelka and F. Munk, Z. Tech. Phys., 11 (1931) 593-601.

101 J. Sirita, S. Phanichphant, and F. C. Meunier, Anal. Chem., 79 (2007) 3912-3918.

102 I. M. Hamadeh and P. R. Griffiths, Appl. Spectrosc., 41 (1987) 682-688.

103 M. Vaarkamp and D. C. Koningsberger, in G.Ertl, E.Knözinger, and Weitkamp J. (Eds.), Handbook of Heterogeneous Catalysis, Vol. 2, Wiley - VCH, Weinheim, 1997, Ch. 3.1.3.2.

104 K. Wille, Physik der Teilchenbeschleuniger und Synchrotronstrahlungsquellen, Teubner Studienbücher, Stuttgart, 1996, Ch. 2.2.

105 Graph. www.psi.ch (2011)

106 J. A. van Bokhoven, T. Ressler, F. M. F. De Groot, and G. Knop-Gericke, in B.M.Weckhuysen (Ed.), In-situ Spectroscopy of Catalysts, American Scientific Publishers, 2004, Ch. 26.

107 K. Getty, M. U. Delgado-Jaime, and P. Kennepohl, Inorg. Chim. Acta, 361 (2008) 1059-1065.

108 D. C. Koningsberger, B. L. Mojet, G. E. van Dorssen, and D. E. Ramaker, Top. Catal., 10 (2000) 143-155.

109 J. J. Rehr and R. C. Albers, Rev. Mod. Phys., 72 (2000) 621-654.

110 A. L. Ankudinov, B. Ravel, J. J. Rehr, and S. D. Conradson, Phys. Rev. B, 58 (1998) 7565-7576.

111 E. Bus, J. T. Miller, A. J. Kropf, R. Prins, and J. A. van Bokhoven, Phys. Chem. Chem. Phys., 8 (2006) 3248-3258.

112 V. Kröger, T.Kanerva, U. Lassi, K. Rahkamaa-Tolonen, T. Lepistö, and R. L. Keiski, Top. Catal., 42 – 43 (2007) 433-436.

113 O. Korkuna, R. Leboda, J. Skubiszewska-Zie,ba, T. Vrublevs'ka, V. M. Gun'ko, and J. Ryczkowski, Micropor. Mesopor. Mater., 87 (2006) 243-254.

114 H. T. Wang, Y. W. Chen, and J. G. Goodwin, Zeolites, 4 (1984) 56-60.

115 T. J. McCarthy, C. M. P. Marques, H. Trevino, and W. M. H. Sachtler, Catal. Lett., 43 (1997) 11-18.

116 S. Eckle, H.-G. Anfang, and R. J. Behm, Appl. Catal. A, 391 (2011) 325-333.

117 A. M. Karim, V. Prasad, G. Mpourmpakis, W. W. Lonergan, A. I. Frenkel, J. G. Chen, and D. G. Vlachos, J. Am. Chem. Soc., 191 (2009) 12230-12239.

118 S. Eckle. Untersuchungen zu Kinetik und Mechanismus der Selektiven Methanisierung von CO auf geträgerten Ru Katalysatoren. (2008) Universität Ulm

119 I.-G. Bajusz and J. G. Goodwin Jr., J. Catal., 169 (1997) 157-165.

120 Y. Men, G. Kolb, R. Zapf, V. Hessel, and H. Löwe, Catal. Today, 125 (2007) 81-87.

121 S. Fujita and T. Notbutsune, Chem. Engin. J., 68 (1997) 63-68.

122 V. P. Londhe and N. M. Gupta, J. Catal., 169 (1997) 415-422.

123 S. Takenaka, T. Shimizu, and K. Otsuka, Int. J. Hydrogen Energy, 29 (2004) 1065-1073.

124 Z. Z. Lin, T. Okuhara, M. Misono, K. Tohji, and Y. Udagawa, J. Chem. Soc. Chem. Commun., (1986) 1673-1675.

125 T. Iwasita-Vielstich, in H.Gerischer and C.W.Tobias (Eds.), Advances in Electrochemical Science and Engineering, VCH Verlagsgesellschaft, Weinheim, 1990.

126 R. L. Gorring and A. J. de Rosset, J. Catal., 3 (1964) 341-352.

127 D. L. King, J. Catal., 51 (1978) 386-397.

128 R. A. Dalla Betta, A. G. Piken, and M. Shelef, J. Catal., 35 (1974) 54-60.

129 H. Knözinger, Y. Zhao, B. Tesche, R. Barth, R. Epstein, B. C. Gates, and J. P. Scott, Faraday Discuss., 72 (1981) 53-74.

130 J. Zhang, M. Li, Z. Feng, J. Chen, and C. Li, J. Phys. Chem. B, 110 (2006) 927-935.

131 E. Guglielminotti, A. Zecchina, A. Bossi, and M. Camia, J. Catal., 74 (1982) 240-251.

132 R. D. Gonzalez and M. F. Brown, J. Phys. Chem., 80 (1976) 1731.

133 A. A. Davydov and A. T. Bell, J. Catal., 49 (1977) 332-344.

134 F. Solymosi and J. Raskó, J. Catal., 15 (1989) 107-119.

135 G. H. Yokomizo, C. Louis, and A. T. Bell, J. Catal., 120 (198) 1-14.

136 E. Guglielminotti and G. C. Bond, J. Chem. Soc. Faraday Trans. I, 86 (1990) 979-987.

137 N. M. Gupta, V. S. Kamble, R. M. Iyer, T. Ravindranathan, and M. Grätzel, J. Catal., 137 (1992) 473-486.

138 S. ZH. Todorova and G. B. Kadinov, Res. Chem. Intermed., 28 (2002) 291-301.

139 H. Pfnür, D. Menzel, F. M. Hoffmann, A. Ortega, and A. M. Bradshaw, Surf. Sci., 93 (1980) 431-452.

140 J. Assmann, E. Loffler, A. Birkner, and M. Muhler, Catal. Today, 85 (2003) 235-249.

141 H. Knözinger and P. Ratnasamy, Catal. Rev., 17 (1978) 31-70.

142 S. T. Yong, K. Hidajat, and S. Kawi, J. Power Sources, 131 (2004) 91-95.

143 C. S. Kellner and A. T. Bell, J. Catal., 71 (1981) 296.

144 F. Solymosi, A. Erdöhelyi, and M. Kocsis, J. Catal., 65 (1980) 428-436.

145 V. Sanchez-Escribando, M. A. Larrubia Vargas, E. Finocchio, and G. Busca, Appl. Catal. A, (2007) 68-74.

146 T. Yamada and K.-I. Tanaka, J. Am. Chem. Soc., 113 (1991) 1173-1176.

147 C. K. Rofer-DePoorter, Chem. Rev., 81 (1981) 447-474.

148 M. Marwood, R. Doepper, and A. Renken, Appl. Catal. A, 151 (1997) 223-246.

149 R. Leppelt, B. Schumacher, V. Plzak, M. Kinne, and R. J. Behm, J. Catal., 244 (2006) 137-152.

150 A. S. Wexler, Spectrochim. Acta, 21 (1965) 1725-1742.

151 K. Yokota, M. Fukui, and T. Tanaka, Appl. Surf. Sci., 121/122 (1997) 273-277.

152 F. Solymosi, A. Erdöhelyi, and T. Bansagi, J. Catal., 68 (1981) 371-382.

153 W. J. Mitchell, Y. Wang, J. Xie, and W. H. Weinberg, J. Am. Chem. Soc., 115 (1993) 4381-4382.

154 M. Wu, D. W. Goodman, and G. W. Zajac, Catal. Lett., 24 (1994) 23-30.

155 C. G. Visconti, L. Lietti, E. Tronconi, P. Forzatti, R. Zennaro, and E. Finocchio, Appl. Catal. A, 355 (2009) 61-68.

156 N. M. Gupta, V. S. Kamble, R. M. Iyer, K. Ravindranathan Thampi, and M. Grätzel, Catal. Lett., 21 (1993) 245-255.

157 C. Schild, A. Wokaun, and A. Baiker, Journal of Molecular Catalysis, 69 (1991) 347-357.

158 K. Christmann, Progr. Surf. Sci., 48 (1995) 15-26.

159 N. Bronstedt, Chem. Rev., 5 (1928) 231-338.

160 M. G. Evans and N. P. Polanyi, Trans. Faraday Soc., 34 (1938) 11-29.

161 B. Hammer and J. K. Nørskov, Surf. Sci., 343 (1995) 211-220.

162 B. Hammer and J. K. Nørskov, Adv. Catal., 45 (2000) 71-129.

163 R. J. Davis, J. Catal., 216 (2003) 396-405.

164 R. van Hardeveld and F. Hartog, Surf. Sci., 15 (1969) 189-230.

165 C. J. H. Jacobsen, S. Dahl, P. L. Hansen, E. Törnqvist, L. Jensen, H. Topsøe, D. V. Prip, P. B. Møenshaug, and I. Chorkendorff, J. Mol. Catal. A, 163 (2000) 19-26.

6 Appendix

Table 8: Catalyst dilution and gas feed composition applied during kinetic experiments

Catalyst	Reformate	dilution
2.2 wt.% Ru/zeolite	0.6 % CO, 2.8 % N_2, balance H_2	1:10
2.2 wt.% Ru/zeolite	0.6 % CO, 4.5 % CH_4 2.8 % N_2, balance H_2	1:10
2.2 wt.% Ru/zeolite	0.6 % CO, 15.5 % CO_2 2.8 % N_2, balance N_2	1:10
2.2 wt.% Ru/zeolite	0.6 % CO, 5 % H_2O 2.8 % N_2, balance H_2	1:10
2.2 wt.% Ru/zeolite	0.3 % CO, 15.5 % CO_2 2.8 % N_2, balance H_2	1:80
2.2 wt.% Ru/zeolite	0.1 % CO, 15.5 % CO_2 2.8 % N_2, balance H_2	1:200
2.2 wt.% Ru/zeolite	100 ppm CO, 2.8 % N_2, balance H_2	1:400
3.6 wt.% Ru/zeolite	0.6 % CO, 5 % H_2O 2.8 % N_2, balance H_2	1:30
3.6 wt.% Ru/zeolite	100 ppm CO, 2.8 % N_2, balance H_2	1:30
5.6 wt.% Ru/zeolite	0.6 % CO, 5 % H_2O 2.8 % N_2, balance H_2	1:600
5.6 wt.% Ru/zeolite	100 ppm CO, 2.8 % N_2, balance H_2	1:60
5.0 wt.% Ru/Al_2O_3	0.6 % CO, 2.8 % N_2, balance H_2	1:3
5.0 wt.% Ru/Al_2O_3	0.6 % CO, 4.5 % CH_4 2.8 % N_2, balance H_2	1:3
5.0 wt.% Ru/Al_2O_3	0.6 % CO, 15.5 % CO_2 2.8 % N_2, balance N_2	1:3

5.0 wt.% Ru/Al_2O_3	0.6 % CO, 5 % H_2O 2.8 % N_2, balance H_2	1:3
5.0 wt.% Ru/Al_2O_3	0.3 % CO, 15.5 % CO_2 2.8 % N_2, balance H_2	1:36
5.0 wt.% Ru/Al_2O_3	0.1 % CO, 15.5 % CO_2 2.8 % N_2, balance H_2	1:100
5.0 wt.% Ru/Al_2O_3	100 ppm CO, 2.8 % N_2, balance H_2	1:180

Table 9: Mass flow controllers used during the different experiments

Mass Flow Controller	Model	Flow·ml^{-1}	Gas
DRIFTS			
1	Hastings Model 202	0-50 N_2	CO_2; N_2
2	Hastings Model 202	0-20 N_2	10% O_2/N_2; CH_4
3	Hastings Model 202	0-100 H_2	H_2; N_2
4	Hastings Model 202	0-20 N_2	2% CO/H_2; CO; N_2
Kinetic experiments			
1	Hastings Model 202	0-10 (100) CO	2% CO/H_2; CO; N_2
2	Hastings Model 202	0-100 N_2	H_2; N_2
3	Hastings Model 202	0-20 N_2	10% O_2/N_2; N_2; CH_4
4	Hastings Model 202	0-100 N_2	CO_2; N_2
XAS experiments			
1	Bronkhorst F-201CV	0-100 H_2	H_2, N_2
2	Bronkhorst F-201CV	0-100 H_2	H_2, N_2
3	Bronkhorst F-201CV	0-50 N_2	N_2, CO
4	Bronkhorst F-201CV	0-20 CO	CO, CO_2
5	Bronkhorst F-201CV	0-20 CO_2	CO_2. H_2
6	Bronkhorst F-201CV	0-20 O_2	CO, CO_2

Table 10: Reaction rates of the CO methanation reaction on different supported Ru catalysts and the respective reaction conditions (TOFs in this work are based on the active surface area determined by H_2 adsorption experiments).

Catalyst	Temperature	Reaction gas mixture	Rate /10^{-6} mol·s^{-1}·g$^{-1}_{cat}$	Rate /10^{-6} mol·s^{-1}·g$^{-1}_{Ru}$	TOF / 10^{-3}. s^{-1}	Reference
4.5 wt% Ru/Al_2O_3	302°C	CO : H_2 (1:4)	0.16	3.56	-	[61]
0.5 wt.% Ru/Al_2O_3	250°C	1 % CO, 50 % H_2, balance He	0.536	107.2	15	[42]
0.5 wt.% Ru/Al_2O_3	250°C	1 % CO, 15 % CO_2, 50 % H_2, balance He	0.373	74.6	11	[42]
0.5 wt.% Ru/Al_2O_3	250°C	1 % CO, 15 % CO_2, 30 % H_2O, 50 % H_2, balance He	0.306	61.2	20	[42]
15 wt.% Ru/Al_2O_3	220°C	0.4 % CO, balance H_2	24.2	161	20	[41]
5 wt.% Ru/Al_2O_3	190°C	0.6 % CO, 2.8 % N_2, balance H_2	0.15±0.027	3.4±0.3	1.1	This work
5 wt.% Ru/Al_2O_3	190°C	0.6 % CO, 15.5 % CO_2, 2.8 % N_2, 5 % H_2O balance H_2	0.19±0.025	3.8±0.5	1.2	This work
5 wt.% Ru/Al_2O_3	190°C	0.6 % CO, 15.5 % CO_2, 2.8 % N_2, balance H_2	0.16±0.023	3.1±0.4	1.0	This work
5 wt.% Ru/Al_2O_3	190°C	0.6 % CO, 4.5 % CH_4, 2.8 % N_2, 5 % H_2O balance H_2	0.22±0.024	4.4±0.4	1.4	This work
3 wt.% Ru/SiO_2	240°C	72 % H_2, 3.6 % CO, balance He,	1.4	46.0	13	[119]
5 wt.% Ru/SiO_2	200°C	1 % CO, 90 % H_2	0.095	1.94	-	[121]
2.2 wt.% Ru/zeolite	190°C	0.6 % CO, 2.8 % N_2, balance H_2	1.40±0.035	63.9±1.5	7.9	This work
2.2 wt.% Ru/zeolite	190°C	0.6 % CO, 15.5 % CO_2, 2.8 % N_2, 5 % H_2O, balance H_2	0.7±0.13	31.8±4.7	3.9	This work
2.2 wt.% Ru/zeolite	190°C	0.6 % CO, 15.5 % CO_2, 2.8 % N_2, balance H_2	1.33±0.2	60.3±4.7	7.4	This work
2.2 wt.% Ru/zeolite	190°C	0.6 % CO, 4.5 % CH_4, 2.8 % N_2, balance H_2	1.42±0.19	64.5±8.3	8.0	This work

Table 11: Apparent activation energy of the CO methanation reaction on different supported Ru catalysts

Catalyst	Reaction gas mixture	Activation energy / kJ·mol^{-1}	Temperature / °C	Reference
5 wt.% Ru/SiO_2	CO : H_2 (1:20)	100	190 - 275	[27]
1.5 % Ru/Al_2O_3	CO/H_2 (562 kPa:187 kPa)	100	190 - 330	[128]
Ru/Al_2O_3	CO/H_2 (300kPa:700 kPa)	138	134 - 217	[129]
5 wt.% Ru/Al_2O_3	CO/H_2 (1 kPa:900 kPa) + 10% H_2O	126	175 - 300	[130]
0.5 wt.% Ru/Al_2O_3	CO/H_2 (0.3 % : 99.7 %)	156	150 - 275	[23]
0.5 wt.% Ru/Al_2O_3	1 % CO, 50 % H_2, balance He	121	200 - 300	[42]
0.5 wt.% Ru/Al_2O_3	1 % CO, 15 % CO_2, 50 % H_2, balance He	77	200 – 300	[42]
0.5 wt.% Ru/Al_2O_3	1 % CO, 15 % CO_2, 30 % H_2O, 50 % H_2, balance He	73	200 - 300	[42]
5 wt.% Ru/Al_2O_3	0.6 % CO; 2.8 % N_2, balance H_2	111±10	165 - 190	This work
5 wt.% Ru/Al_2O_3	0.6 % CO; 2.8 % N_2, 15.5 % CO_2, balance H_2	92±9	165 - 190	This work
5 wt.% Ru/Al_2O_3	0.6 % CO, 2.8 % N_2, 15.5 % CO_2, 5 % H_2O, balance H_2	106±11	165 - 190	This work
2.2 wt.% Ru/zeolite	0.6 % CO; 2.8 % N_2, balance H_2	90±11	165 - 190	This work
2.2 wt.% Ru/zeolite	0.6 % CO; 2.8 % N_2, 15.5 % CO_2, balance H_2	80±11	165 - 190	This work
2.2 wt.% Ru/zeolite	0.6 % CO, 2.8 % N_2, 15.5 % CO_2, 5 % H_2O, balance H_2	83±8	165 - 190	This work

2.2 wt.% Ru/zeolite and 5 wt% Ru/Al_2O_3 catalyst before reaction

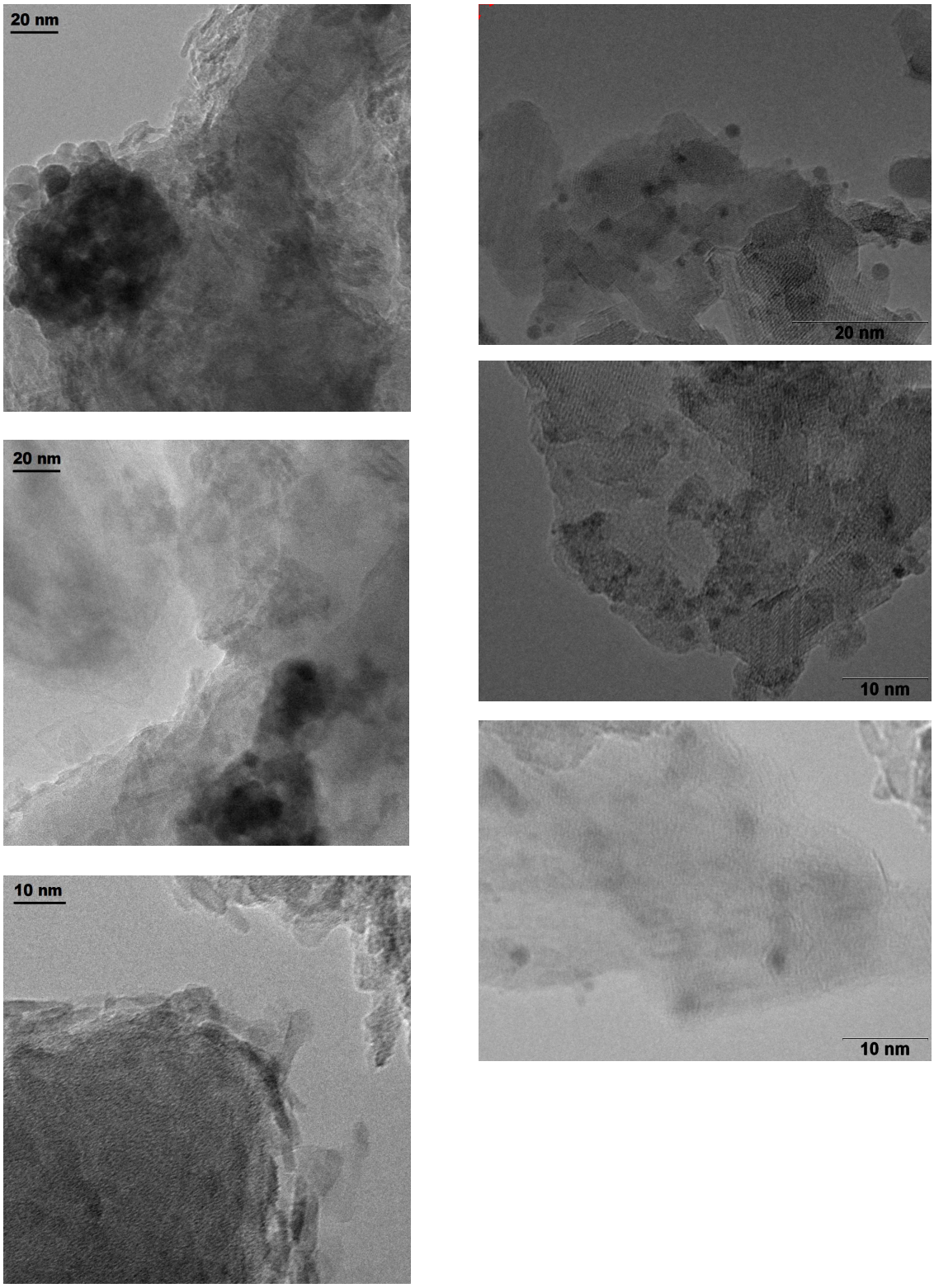

Figure 41: TEM pictures of the Ru/zeolite catalyst and the Ru/Al_2O_3 catalyst before reaction

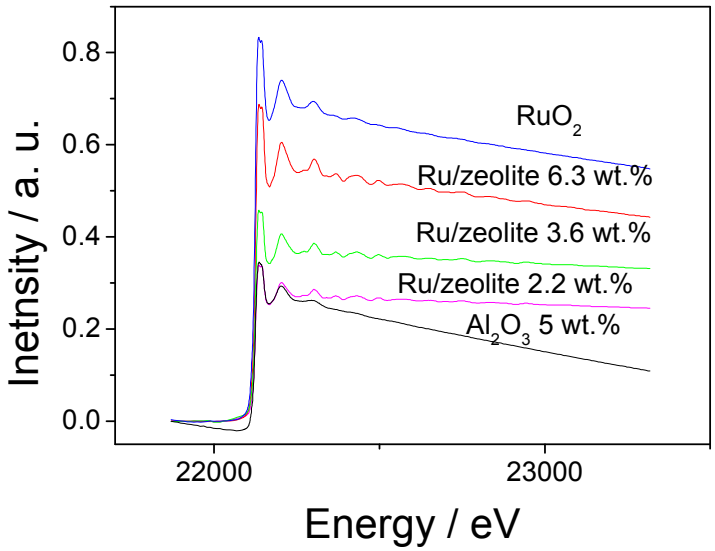

Figure 42: XANES spectra of the RuO_2 reference and differently loaded catalysts prior to reaction.

6.1 German Summary

In der vorliegenden Arbeit habe ich Ergebnisse zum Mechanismus der selektiven Methanisierung von CO über geträgerte Ru Katalysatoren aus kinetischen, *in situ* IR spektroskopischen und *in situ* XAS Messungen beschrieben. Während dieser Dissertation konnte ich die Röntgen Absorptionspektroskopie als Charakterisierungsmethode einführen und im Zuge dessen, zur Durchführung von XAS Messungen, als Teil dieser Arbeit eine Messzelle mit portabler Gasmischeinheit konstruiert. Die am Synchrotron durchgeführten XAS Messungen zeigten dabei Änderungen der mittleren Koordinationszahl und des Oxidationszustandes von Ru. Diese Ergebnisse ermöglichten die Bestimmung und die Beobachtung der Änderung der mittleren Ru Partikelgröße während der Reaktion und dadurch deren Korrelation zur Aktivität und CO Selektivität. Während dieser Arbeit wurden folgende Ergebnisse erhalten:

(I) Die Katalysatoren wiesen unterschiedliche mittlere Ru Nanopartikelgrößen auf, welche im Falle der 2.2, 3.6 und 5.6 Gew.% Ru/Zeolith Katalysatoren (d= 0.9, 1.6 und 1.9 nm) durch *in situ* EXAFS Messungen und im Falle des 5.0 Gew.% Ru/Al_2O_3 Katalysators (d= 2.3 nm) durch TEM und *in situ* EXAFS Messungen erhalten wurden. Standard Charakterisierungsmethoden wie TEM oder XRD führten bei den Ru/Zeolith Katalysatoren zu unrealistischen Ru Partikelgrößen, da sich der Träger unter dem fokusierten Elektronenstrahl zersetzte und dadurch eine Auswertung der Partikelgrößen unmöglich wurde, bzw. die Koexistenz sehr großer Nanopartikel das Signal der kleinen im XRD überlagerte. Da jedoch die Partikelgrößen des Ru/Al_2O_3 Katalysators aus den TEM Messungen mit denen aus den EXAFS Messungen übereinstimmten, konnte davon ausgegangen werden, dass Auswertung der Partikelgrößen aus den EXAFS Messungen korrekt erfolgt ist. Die Ru Nanopartikel werden für die Ru/Zeolith Katalysatoren in den Poren vermutet, da die mittlere Ru Partikelgröße des 2.2 Gew.% Ru/Zeolith Katalysators ungefähr mit der Porengröße des Trägers übereinstimmte. Weiterhin wies der Katalysator eine viel geringere XPS Intensität im Vergleich zu dem Ru/Al_2O_3, Katalysator auf, was als zusätzlicher Hinweis für die Einlagerung der Ru Partikel in die Poren des Zeolithen gewertet werden kann. Die zunehmende Größe der Ru Nanopartikel auf den Zeolith Katalysatoren mit höherer Beladung wurde einer zunehmenden Anzahl von größeren Ru Partikeln auf der äußeren Oberfläche des Zeolithen zugeschrieben.

(II) Sowohl der Ru/Al_2O_3, als auch der Ru/Zeolith Katalysator sind für die selektive CO Methanisierung aktiv. Die Aktivität der CO_2 Methanisierung hängt sowohl vom Katalysator als auch von der Ru Partikelgröße ab. Integrale Messungen zeigten für den 2.2 Gew.% Ru/Zeolith Katalysator eine um 20°C niedrigere Reaktionstemperatur (190°C) für den Vollumsatz von CO im Vergleich zu dem 5 Gew.% Ru/Al_2O_3 Katalysator, welcher Vollumsatz erst bei 210°C aufwies. Zusätzlich war der Ru/Zeolith Katalysator bei dieser Temperatur auch in semirealistischen Reformaten ($H_2/CO/CO_2$) 100% CO selektiv. CO_2 wurde hier nur bei sehr viel höheren Temperaturen zu einem merklichen Anteil umgesetzt, wobei 50% CO_2 Umsatz bei 330°C und Vollumsatz erst bei 410°C beobachtet wurde, sogar dann, wenn kein CO in der Gasphase vorhanden war (CO_2/H_2). Der Ru/Al_2O_3 Katalysator zeigte Vollumsatz von CO_2 in semirealistischen Reformaten ($H_2/CO/CO_2$) schon bei 230°C. Zusätzlich wies dieser Katalysator für die CO_2 Methanisierung in CO freien Gasgemischen (CO_2/H_2) das gleiche charakteristische Temperaturprofil auf, wie es bei der CO Methanisierung beobachtet wurde, was auf unselektive aktive Zentren hindeutet, die sowohl CO als auch CO_2 mit nahezu gleicher Aktivität methanisieren. Dies wurde durch einen Blockade Mechanismus von adsorbierten CO_{ad} auf den aktiven Plätzen erklärt. Solange genügend CO_{ad} auf der Oberfläche vorhanden ist (1 Monolage), wird CO_2 nicht dissoziiert. Fällt diese Bedeckung unter einen kritischen Wert, so werden die freien Adsorptionsplätze von CO_{ad} aus CO_2 aufgefüllt.

(III) Die Reaktionsraten beider Katalysatoren liegen je nach Reaktionsreformat zwischen 3.1 und 4.4×10^{-6} $mol \cdot g^{-1} \cdot s^{-1}$ (Ru/Al_2O_3) bzw. 31.8 und 63.9×10^{-6} $mol \cdot g^{-1} \cdot s^{-1}$ (2.2 Gew.% Ru/Zeolith). Die Erweiterung des Reformats um CH_4 und CO_2 um damit realistischere Reformate zu simulieren, hatte bei beiden Katalysatoren keinen merklichen Einfluss auf die Reaktionsrate. Lediglich das Hinzufügen von 5 % Wasser zum Reformat führte im Falle des Ru/Zeolith Katalysators zu einer Halbierung der Reaktionsrate. *In situ* DRIFTS Messungen zeigten hier eine 50%ige Intensitätserniedrigung der auf metallischem Ru linear adsorbierten CO_{ad} Spezies. Es wurde vermutet, dass das Zwischenprodukt, welches auf denselben Plätzen wie CO_{ad} adsorbiert, ebenfalls durch Wasser verdrängt wird, und dadurch Einfluss auf die Reaktionsrate nimmt. Die Aktivierungsenergie der selektiven Methanisierung von CO lag für alle untersuchten Reformate bei beiden Katalysatoren zwischen 90 (Ru/Zeolith) und 110 (Ru/Al_2O_3) $kJ \cdot mol^{-1}$. Die Reaktionsordnung bezüglich CO lag bei -0.7 (Ru/Zeolith) und bei -0.5 (Ru/Al_2O_3). Für H_2 wurde auf dem Ru/Al_2O_3 Katalysator

eine Reaktionsordnung 1.0 gemessen, was einen deutlich niedrigeren Wert als die Reaktionsordnung von 2.7 auf dem Ru/Zeolith Katalysator darstellt. Dieser um den Faktor 2.7 höhere Wert wird als einer der Gründe für die hohe Aktivität des Ru/Zeolith Katalysators verantwortlich gemacht. Transiente *in situ* DRIFTS und MS Messungen, bei denen nach Erreichen des dynamischen Gleichgewichts nach 1000 min Reaktion in idealisierter Atmosphäre (H_2/CO), CO durch N_2 ersetzt wurde, zeigten, dass die beobachteten CH_x Spezies keinen dominanten Reaktionspfad darstellen können. Die Abreaktion dieser Spezies verläuft, verglichen mit dem Abklingen des CH_4 Signals im Massenspektrometer, auf einer zu langen Zeitskala. Möglicherweise nimmt nur ein geringer reaktiver Anteil von CH_x Spezies an der Reaktion teil. Deren Signale im IR wurden wahrscheinlich von den weitaus größeren Banden der unreaktiven CH_x Spezies überdeckt.

(IV) Der molekulare Mechanismus der CO und CO_2 Methanisierung wurde mittels SSITKA (Steady State Isotope Transient Kinetic Analysis) Experimenten untersucht, bei denen nach Erreichen des dynamischen Gleichgewichts nach 1000 min Reaktion ein Edukt (^{12}CO oder $^{12}CO_2$) durch sein Isotop (^{13}CO oder $^{13}CO_2$) ersetzt wurde. Auf dem Ru/Al_2O_3 Katalysator konnte so eine ‚Formyl' Spezies (CHO_{ad}) als Zwischenprodukt der CO Methansierung identifiziert werden, da seine Abreaktionsrate der Reaktionsrate aus kinetischen Messungen entsprach. Derselbe Mechanismus wurde für den Ru/Zeolith Katalysator vorgeschlagen, obwohl eine ähnliche Spezies noch nicht nachgewiesen werden konnte, was vermutlich an seiner 20-fach höheren Aktivität lag. Weiterhin konnte für beide Katalysatoren gezeigt werden, dass der Mechanismus der CO_2 Methansierung über CO_{ad} zu CH_4 abläuft. Hierbei wird CO_2 dissoziativ adsorbiert (CO_{ad} und O_{ad}), und nicht über ein Formiat in CO_{ad} umgewandelt.

Die Kombination der bisher gezeigten Ergebnisse, lässt metallisches Ru als aktives Zentrum der selektiven Methanisierung schließen. Auf diesem reagiert adsorbiertes CO_{ad} zu HCO_{ad} und schließlich zu CH_4. Das Zwischenprodukt (HCO_{ad}) scheint ebenfalls auf den Ru Nanopartikeln adsorbiert zu sein. Weiterhin konnte ich zeigen, dass der 2.2 Gew.% Zeolith Katalysator mit den sehr kleinen Ru Nanopartikeln eine höhere Reaktionsrate als der Ru/Al_2O_3 Katalysator aufweist. Dies wird einerseits den möglicherweise vorhandenen Träger-Metall Wechselwirkungen und andererseits der hohen H_2 Reaktionsordnung zugeschrieben. Für die sehr hohe CO Selektivität des Zeolith Katalysators sind ebenfalls die sehr kleinen Ru Nanopartikel verantwortlich

(siehe weiter unten). Dies ist auch eine Erklärung dafür, dass die Wassergas-Shift-Rückreaktion (CO_2 zu CO) nie unter den hier gewählten Bedingungen auf dem Ru/Zeolith Katalysator beobachtet wurde.

(V) Es konnte gezeigt werden, dass die Ru Partikelgröße einen maßgeblichen Einfluß auf die CO Selektivität der selektiven Methanisierung von CO in CO_2 reichen Brenngasen ausübt. Der Ru/Al_2O_3 Katalysator, mit einer mittleren Ru Partikelgröße von 2,3 nm, wies eine deutlich schlechtere CO Selektivität (~45%) bei geringen CO Partialdrücken (100 ppm) in semirealistischen Reformaten auf, als der Ru/Zeolith Katalysator (d= 0.9 nm, 100%) bei identischen Bedingungen. Die Abnahme der CO Selektivität korrelierte mit einer Erniedrigung der CO_{ad} Signalintensität in *in situ* DRIFTS Messungen, welches als Maß für das Zwischenprodukt der CO_2 Methanisierung und damit für die Selektivität genommen werden kann. Im Falle des Ru/Al_2O_3 Katalysators wird der Mechanismus der CO Selektivität über einen Blockademechanismus gesteuert, bei dem CO_2 nicht adsobiert und gespalten wird, solange genügend CO die Oberfläche bedeckt (1 Monolage). Sinkt die CO Bedeckung unter den kritischen Wert einer Monolage, füllt CO aus dissoziertem CO_2 die frei gewordenen aktiven Plätze auf, was einer Erniedrigung der Selektivität gleich kommt. Folgerichtig wurde auch unter CO freien Bedingungen ein Wert nahe der CO_{ad} Sättigungsintensität erreicht, wenn nur CO_2 in der Gasmischung vorhanden war (H_2/CO). Der Ru/Zeolith Katalysator zeigte hierbei eine ganz andere Charakteristik. Hier konnte in *in situ* DRIFTS Messungen unter geringen CO Partialdrücken (100 ppm CO) kein zusätzliches CO_{ad} aus CO_2 beobachtet werden. Sogar in CO freiem Reformat erreichte die CO_{ad} Bande, welche durch dissoziiertes CO_2 entstand, nur 6% der Sättigungsintensität. Dieses Verhalten wurde einer inhärent kleinen CO_2 Methanisierungsaktivität der sehr kleinen Ru Nanopartikel zugeordnet. Das unterschiedliche Verhalten konnte mit Hilfe des Brønstedt-Evans-Polanyi (BEP) Zusammenhangs erklärt werden, demzufolge mit zunehmender Partikelgröße die CO_2 Dissoziationsrate steigt, da dessen Produkt (CO_{ad}) auf großen Partikeln besser stabilisiert ist.

(VI) Um Träger-Metall Wechselwirkungen als Ursache für die unterschiedliche Selektivität der zwei Katalysatoren (5.0 Gew.% Ru/Al_2O_3 und 2.2 Gew.% Ru/Zeolith) auszuschließen, wurden identische Experimente auf unterschiedlich beladenen (3.6 Gew.% und 5.6 Gew.%) aber ansonsten gleichen Ru/Zeolith Katalysatoren durchgeführt. Diese Katalysatoren wiesen im Vergleich zum 2.2 Gew.% Ru/Zeolith

Katalysator (d= 0.9 nm) größere mittlere Ru Partikelgrößen auf (d= 1.6 und 1.9 nm), welche vergleichbar mit der des Ru/Al_2O_3 Katalysators sind. Es konnte gezeigt werden, dass auch auf dem Zeolith geträgerten Katalysatorsystem die CO Selektivität mit zunehmender Ru Partikelgröße abnimmt, was sowohl durch kinetische als auch durch *in situ* DRIFTS Messungen verifiziert wurde. Im Gegensatz dazu nahm die Methanisierungsaktivität (auf g_{Ru} normiert) mit größerer Ru Partikelgröße, sowohl für CO als auch für CO_2 Methanisierung, zu.

Zum Abschluß möchte ich auf die Bedeutung dieser Ergebnisse für die praktische Anwendung dieser Katalysatoren in der Reformatreinigung für PEM Brennstoffzellen eingehen. Werden die 5 Gew.% Ru/Al_2O_3, 3.6 oder 5.6 Gew.% Ru/Zeolith Katalysatoren mit Ru Partikelgrößen größer als 1.5 nm für die selektive Methanisierung verwendet, wird die CO_2 Methanisierung immer dann stattfinden, sobald der CO Partialdruck und daraus folgend die CO_{ad} Bedeckung unter einen kritischen Wert fällt; zum Beispiel am Ende eines Methanisierungsreaktors. In diesem Fall ist die komplette Entfernung von CO ohne einen Beitrag der CO_2 Methanisierung nicht möglich. Die höher beladenen Ru/Zeolith Katalysatoren weisen zwar gegenüber dem 2.2 Gew.% Ru/Zeolith Katalysator höhere Methanisierungsraten auf, was prinzipiell immer wünschenswert ist, jedoch wird dieser Vorteil auf Kosten der CO Methanisierungsselektivität erreicht. Im Gegensatz dazu wird die CO_2 Methanisierung auf dem 2.2Gew.% Ru/Zeolith Katalysator sogar bei sehr kleinen CO Partialdrücken verhindert. Dies wird der inhärent niedrigen CO_2 Dissoziationsaktivität auf den sehr kleinen Ru Nanopartikeln zugeschrieben. Deshalb, ist der Mechanismus welcher der CO Selektivität zugrunde liegt ein anderer als der, welcher auf dem Ru/Al_2O_3 Katalysator abläuft. Dieser erlaubt die hochselektive Entfernung von CO aus H_2 reichen Brenngasen bis hin zu sehr kleinen CO Partialdrücken, und folglich die komplette Entfernung von CO (< 10 ppm), ohne eine merkliche CO_2 Methanisierung, solange die Reaktionstemperatur unterhalb der Temperatur ist, die für eine deutliche CO_2 Dissoziation benötigt wird. Basierend auf der inhärent niedrigen CO_2 Methanisierungsaktivität wird der 2.2 Gew.% Ru/Zeolith Katalysator auch unter dynamischen Bedingungen hervorragend arbeiten, bei welchen ansonsten eine Änderung des CO Partialdruckes zu einer merklichen Methanisierung von CO_2 führen würde. Als letzten Punkt möchte ich darauf eingehen, dass der Schlüssel für eine hohe Selektivität für die CO Methanisierung auf den hier

untersuchten Systemen die Ru Partikelgröße darstellt. Es ist essentiell eine sehr kleine und stabile Partikelgröße zu produzieren, um eine hohe CO Selektivität zu gewährleisten. Dies wurde durch die Verwendung eines Zeolithen als Träger realisiert. Dort befinden sich die Ru Nanopartikel in den Poren, so dass das Sintern zu größeren Agglomeraten verlangsamt wird, was folglich die CO_2 Methanisierung hemmt. Diese Eigenschaft ist die wichtigste Voraussetzung um PEM Brennstoffzellen, welche hochreinen Wasserstoff benötigen, gegenüber bewährten Technologien attraktiver zu machen.

6.1.1 List of publications

Publications in scientific journals

1. S. Eckle, Y. Denkwitz and R.J. Behm, *Activity, selectivity, and adsorbed reaction intermediates/reaction side products in the selective methanation of CO in reformate gases on supported Ru catalysts*, Journal of Catalysis 269 (2010) 255 - 268

2. S. Eckle, H.G. Anfang and R.J. Behm, *What drives the selectivity for CO methanation in the methanation of CO_2-rich reformate gases on supported Ru catalysts*, Applied Catalysis A: General 391 (2011) 325-333

3. S. Eckle, H.G. Anfang and R.J. Behm, *Reaction intermediates and side products in the methanation of CO and CO_2 over supported Ru catalysts in H_2-rich reformate gases*, Journal of Physical Chemistry C 115 (2011) 1361-1367

4. J. Geserick, T. Fröschl, N. Hüsing, G. Kucerova, M. Makosch, T. Diemant, S. Eckle, and R.J. Behm, *Molecular approaches towards mixed metal oxides and their behaviour in mixed oxide support Au catalysts for CO oxidation*, Dalton Transaction 40 (2011) 3269-3286

5. S. Eckle, M. Augustin, H.G. Anfang and R.J. Behm, *Influence of the catalyst loading on the activity and the CO selectivity of supported Ru catalysts in the selective methanation of CO in CO_2 containing feed gases*, Catalysis Today 181 (2012) 40-51

Conference Contributions

1. S. Eckle, A. Karpenko, R. Leppelt and R.J. Behm, *Kinetik und Mechanismus der selektiven Methanisierung von CO über Ru Katalysatoren*, 41. Jahrestreffen Deutscher Katalytiker, Weimar, 2008

2. S. Eckle, M. Wassner, R. Leppelt and R.J. Behm, *Kinetics and Mechanism of the selective methanation of CO on Ru catalysts*, Ulm ElectroChemical Talks, Ulm, 2010

3. S. Eckle, H.G. Anfang and R.J. Behm, *Kinetik und Mechanismus der selektiven Methanisierung von CO über Ru Katalysatoren*, 42. Jahrestreffen Deutscher Katalytiker, Weimar, 2009

4. S. Eckle, H.G. Anfang and R.J. Behm, Aktivität und Selektivität der selektiven Methanisierung von CO über Ru Katalysatoren in Abhängigkeit der Ru Beladung, 43. Jahrestreffen Deutscher Katalytiker, Weimar, 2010

5. S. Eckle, H.G. Anfang, R.J. Behm, *Carriers selective methanation of CO in CO2–rich feed Gases on Supported Ru Catalysts,* 18th World Hydrogen Energy Conference 2010 - WHEC 2010 : Parallel Sessions Book 3: Hydrogen Production Technologies - Part 2 / Detlef Stolten, Thomas Grube (Ed.) Forschungszentrum Jülich GmbH, Zentralbibliothek, Verlag : 2010 ; WHEC, May 16.-21. 2010, Essen ; 271

6. S.Eckle, H.G. Anfang and R.J. Behm, *High selectivity for CO methanation in the methanation of CO_2-rich reformate gases on supported Ru catalysts-Mechanism and physical origin*, Ulm ElectroChemical Talks, Ulm, 2010

7. S. Eckle, H.G. Anfang and R.J. Behm, *Influence of the support on the activity and selectivity of supported Ru catalysts in feed gas processing by selective methanation of CO*, First International Conference on Materials for Energy, Karlsruhe, 2010

8. S. Eckle, H.G. Anfang and R.J. Behm, *Mechanismus der selektiven Methanisierung von CO über Ru Katalysatoren*, 44. Jahrestreffen Deutscher Katalytiker, Weimar, 2011

6.1.2 Curriculum Vitae

The curriculum vitae has been removed for reasons of data protection from the electronic version

7 Acknowledgement

At this point I would like to thank all those who contributed to the success of this thesis.

- I am especially grateful to Prof. R.J. Behm for providing the challenging and interesting topic, the opportunity to work on it in his institute and his ongoing support throughout the years.
- I thank Prof. N. Hüsing for her willingness to review the thesis and for coming from Salzburg to Ulm for my defense.
- I thank Prof. M. Muhler for giving the third expert opinion.
- Georg Anfang I would like to thank for his support concerning the synthesis of the Ru catalysts and the nice discussions throughout the years.
- I thank Daniel Widmann, Dr. Gabriela Kucerova for the great working atmosphere, the nice discussions and the fun during the synchrotron experiments.
- I thank in particular Dr. Gabriela Kucerova for reading the PhD thesis before submission, and Robert Reichert and Christian Gebauer, for helping to find typos.
- Prof. van Bokhoven and Evalyn Alayon (ETH) I would like to thank for introducing me to EXAFS spectroscopy, and their help with its evaluation
- Thomas Häring I would like to thank for the ongoing support when something broke again, his time and advices when setting up the *in situ* XAS cell and for the great times during the synchrotron trips, especially in France, and especially for the discussions in his office.
- Gerd Bräth I would like to thank for his support in all electronic concerns.
- I give thanks to PD Dr. Joachim Bansmann for his helping hand and advices concerning XAS planning and measurements.
- All colleagues of the IOK I would like to thank for the great atmosphere and the good discussions during coffee breaks.

8 Declaration

I hereby certify that this dissertation has been composed by me and is based on my own work, unless stated otherwise. This work has not been submitted for any other degree.

Ulm, 09.02.2012

(Stephan Eckle)